A p p e n d i x D

Supplementary Information for Chapter 5

D.1 General considerations

All manipulations were carried out using standard Schlenk or glovebox techniques under an N_2 atmosphere. Solvents were deoxygenated and dried by thoroughly sparging with N_2, followed by passage through an activated alumina column in a solvent purification system by SG Water, USA LLC. Nonhalogenated solvents were tested with sodium benzophenone ketyl in tetrahydrofuran (THF) to confirm the absence of oxygen and water. Deuterated solvents were purchased from Cambridge Isotope Laboratories, Inc., degassed, and dried over activated 3-Å molecular sieves prior to use.

D.1.1 Materials

HEH_2,[1] $[MoBr_3]$,[2] $[PCPMoCl_3]$,[3] [ColH]OTf,[4] [TBA][$^{15}NO_3$],[4] $^{15\text{-}N}HEH_2$,[4] $^{15\text{-}N}$[ColH]OTf,[4] $^{15\text{-}N}$Col,[5] d_2-HEH_2,[6] d_1-HEH_2 (N-H proton is deuterated),[7] d_3-HEH_2,[8] [ImidH]OTf,[9] were synthesized using literature procedures. d_2-$^{15\text{-}N}HEH_2$ was synthesized as $^{15\text{-}N}HEH_2$ or d_2-HEH_2 but using both [$^{15}NH_4$]Cl and d_2-paraformaldehyde._tolNO_2, ^{Me2N}PhCHO, ^{MeO}PhCHO, [TBA][NO_3], $^{n}PrNO_2$, benzyl acetone, Me_3NO, imidazole, and dimethylterphatalate were purchased from Sigma and used without further purification. Col was purchased from Ambeed and distilled prior to use. ^{15N}Col was also distilled following synthesis. [$^{15}NH_4$]Cl, d_2-paraformaldehyde, D_2O and d_1-EtOD were purchased from Cambridge Isotope Laboratories, Inc.

D.1.2 Spectroscopy

Nuclear Magnetic Resonance spectroscopy: Nuclear Magnetic Resonance (NMR) measurements were recorded with a Varian 400 MHz spectrometer. ^{1}H NMR chemical shifts are reported in ppm relative to tetramethylsilane, using ^{1}H resonances from residual solvent as internal standards.[10]

Ultraviolet-visible spectroscopy: Ultraviolet-visible (UV-vis) absorption spectroscopy measurements were collected with a Cary 50 UV-vis spectrophotometer using a 1 cm path length quartz cuvette. All samples had a solvent background subtraction applied.

Continuous-wave Electron Paramagnetic Resonance spectroscopy: All X-band continuous-wave electron paramagnetic resonance (CW-EPR) spectra were obtained on a

Bruker EMX spectrometer using a quartz liquid nitrogen immersion dewar on samples prepared as frozen THF solutions unless otherwise noted.

Infrared spectroscopy: Solution state infrared (IR) spectra were obtained using a Bruker Alpha Platinum ATR spectrometer with OPUS software in a glovebox under an N_2 atmosphere. All IR data were collected as solution state spectra in a KBr-cell in THF and, unless stated, have had THF background spectra subtracted.

Steady-state Fluorimetry: Steady-state fluorimetry was performed in the Beckman Institute Laser Resource Center (California Institute of Technology). Samples for luminescence measurements were prepared in dry THF and transferred to a 1-cm path length–fused quartz cuvette sealed with a high-vacuum Teflon valve (Kontes). Steady-state emission spectra were collected on the Jobin S4 Yvon Spec Fluorolog-3-11 with a Hamamatsu R928P photomultiplier tube detector with photon counting.

Transient absorbance spectroscopy: Transient Absorption Samples in stirred air-tight cuvettes were excited with 355-nm or 450-nm pulses from a Q-switched Nd:YAG laser (Spectra-Physics Quanta-Ray PRO-Series) or a tunable Nd:YAG-pumped optical parametric oscillator (Opotek Radiant QX8130U), both operating at a 10 Hz repetition rate. Probe light from a current-pulsed (1 ms) 75-W Xe arc lamp was directed with all-reflective optics collinearly with the laser excitation through the cuvette and wavelength selected using a double monochromator (ISA DH10). Wavelength-selected probe light was detected by a photomultiplier tube (PMT, Hamamatsu R955) wired for 5 gain stages. The PMT output was amplified (Femto DHPCA-100), offset in a wideband differential amplifier, and digitized at speeds up to 1 GS/s with a transient digitizer (GageScope). For luminescence decay measurements, the probe light was blocked, and sample fluorescence was detected by the PMT. Data collection was controlled by a PC with software written in LabView (National Instruments). Signals were averaged for several hundred laser shots to optimize signal-to-noise levels.

Time-resolved Fluorescence: Laser excitation was provided by regeneratively amplified (Continuum) pulses from a diode pumped passively mode-locked Nd:YAG laser (Spectra Physics Vanguard 2000). The output from the regenerative amplifier was tripled

(355 nm, ~10 ps) and directed onto the sample held in a stirred 1-cm air-tight fluorescence cuvette. Fluorescence was collected at 90° using reflective optics and focused onto the entrance slit of a 0.275 m spectrograph (Acton SpectraPro 275). A fiber bundle at the spectrograph image plane collected the fluorescence and directed it to the entrance slit of a picosecond streak camera (Hamamatsu C5680). The streak camera was operated in photon counting mode using High-Performance Digital Temporal Analyzer software (Hamamatsu). The instrument time resolution is ~20 ps.

D.2 NH_3 generation experiments

D.2.1 Standard NH_3 Generation Reaction Procedure

In a nitrogen-filled glovebox, the precatalyst ([$MoBr_3$]) (2.3 μmol) is weighed into individual vials. The precatalyst is then transferred quantitatively into a Schlenk tube using THF. The THF is then evaporated to provide a thin film of precatalyst at the bottom of the Schlenk tube. The tube is then charged with a stir bar, and dihydropyridine (124 μmol) is added as solids. The acid and base (124 μmol of each) are dissolved in 1 mL solvent and added to the tube to produce a concentration of precatalyst of 2.3 mM. This tube is sealed, passed out of the box, and transported to a fume hood, where the tube is transferred to a water bath, where it is allowed to stir for 12 hours while irradiated by a Kessil™ as indicated. To ensure reproducibility, all experiments were conducted in 50 mL Schlenk tubes (20 mm OD) using 10 mm egg-shaped stir bars and stirring at ~600 rpm. The water bath was contained in highly reflective dewars. The LED was placed above the bath as close to the stirring reaction without touching the tube or the dewar.

Following completion, the reaction mixtures are cooled to 77 K and allowed to freeze. The reaction vessel is then opened to the atmosphere, and the frozen solution is slowly added to excess of a solution of HCl (3 mL of a 2.0 M solution in Et_2O, 6 mmol) over 1-2 minutes. This solution is allowed to freeze, then the headspace of the tube is evacuated, and the tube is sealed. The tube is then allowed to warm to RT and stirred at RT for at least 10 minutes. Solvent is removed *in vacuo*, and the solids are extracted with 1 M $HCl_{(aq)}$ and filtered to give a total solution volume of 10 mL. A 5 mL aliquot is taken and washed

repeatedly with n-butanol to remove Hantzsch pyridine (HE) and collidinium. After n-butanol washing additional 1 M HCl(aq) is added to give a final total volume of 5 mL. From these 5 mL solutions, a 100 µL aliquot is analyzed for the presence of NH_3 (present as $[NH_4][Cl]$) by the indophenol method. Quantification was performed with UV-vis spectroscopy by analyzing the absorbance at 635 nm.[11]

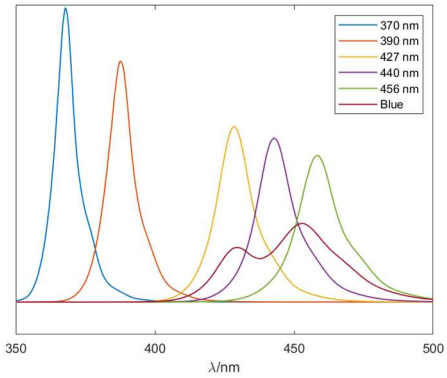

Figure D.1. Lamp relative emission spectra of Kessil™ H160 and H150 lamps used in this study. Emission spectra are measured as photoncount and normalized to wattage. All spectra were measured at multiple intensities to avoid detector saturation.

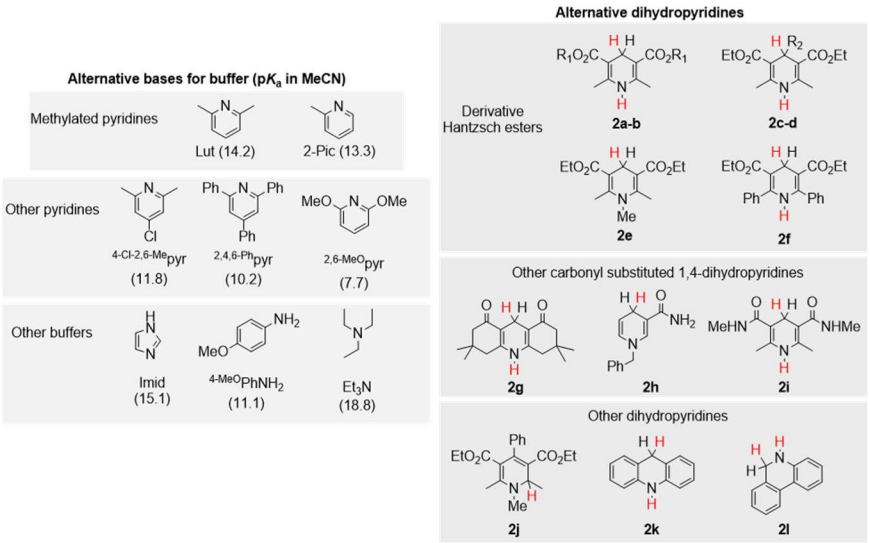

Figure D.2. Structures of buffers and dihydropyridines canvassed for N_2R in Table D.7. Hantzsch ester derivatives are labeled as follows: 2a: R_1 = Me; 2b: R_1 = ^{t}Bu; 2c: R_2 = Ph; 2d: R_2 = $^{4\text{-CN}}$Ph.

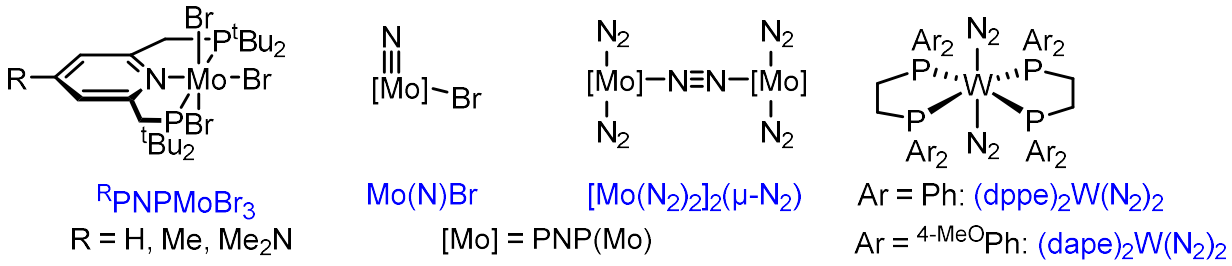

Figure D.3. Additional transition metal catalysts tested for photodriven N_2R.

Table D.1. Catalytic yields for reduction of N_2 to yield NH_3 varying the irradiation wavelength.

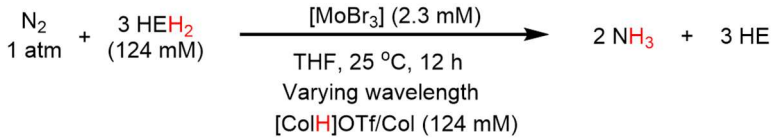

Entry	Lamp	NH_3 (equiv/ Mo)	NH_3 yield/ HEH_2 (%)
1	H150 Blue[a], 34 W	9.5 ± 1	26.5 ± 3
2	H150 Blue, 68 W	13 ± 2	36 ± 5
3	H160 456 nm	<0.1	<0.3
4	H160 440 nm	1.5 ± 0.5	4 ± 1
5	H160 440 nm, 80 W, 24 hrs	4.6 ± 0.2	12.6 ± 0.05
6	H160 427 nm	6.6 ± 0.9	18 ± 2.5
7	H160 427 nm, 80 W	20.4 ± 0.6	57 ± 2
8	H160 427 nm, 80 W, 0.575 mM Mo	28 ± 3	19 ± 2
9	H160 390 nm	15.9 ± 1.4	44 ± 4
10	H160 390 nm, 80 W	17.6 ± 0.4	49 ± 1
11	H160 370 nm	2.7 ± 0.7	7.5 ± 2

[a] Yields taken from ref 4.

Table D.2. Yields for wavelength dependence for organic products (HE and HEH_2) from N_2R.

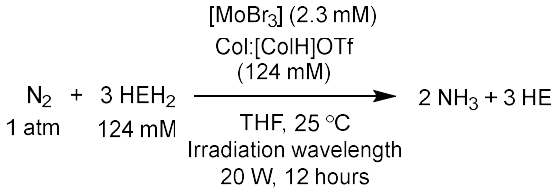

Entry	Lamp	Other Variations	HE yield (%)	HEH_2 yield
1	H160 456 nm		12%	86%
2	H160 440 nm	12 hours, 20 W	69%	19%
3	H160 440 nm	24 hours, 80 W	85%	<1%
4	H150 Blue LED		85%	<1%
5	H160 390 nm		68%	<1%
6	H160 370 nm		59%	<1%
7	H150 Blue LED	Lut-buffer	55%	<1%

Table D.3. Catalytic yields for reduction of N_2 to yield NH_3 varying the irradiation wavelength $PCPMoCl_3$ as precatalyst.

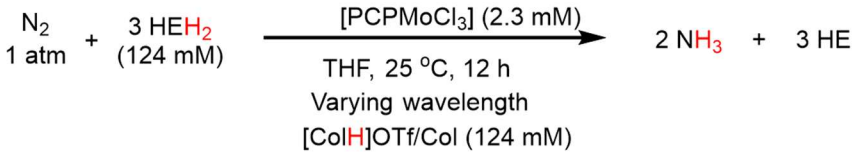

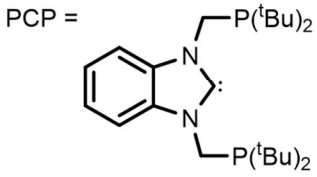

Entry	Lamp	NH_3 (equiv/ Mo)	NH_3 yield/ HEH_2 (%)
1	H160 456 nm	<0.1	<0.3
2	H160 440 nm	1.2	3
3	H160 427 nm	4.3	12

Table D.4. Catalytic yields for reduction of N_2 to yield NH_3 varying the irradiation wavelength in the absence of buffer.

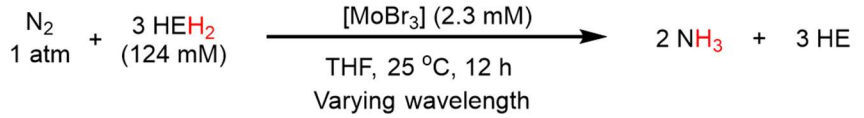

Entry	Lamp	NH_3 (equiv/ Mo)	NH_3 yield/ HEH_2 (%)
1	H150 Blue LED[a]	0.9 ± 0.2	2.6 ± 0.5
2	H160 440 nm,	<0.1	<0.3
3	H160 427 nm	<0.1	<0.3
4	H160 390 nm	0.4 ± 0.3	1.1 ± 0.8
5	H160 370 nm	<0.1	<0.3

[a] Yields taken from ref 4.

Table D.5. Catalytic yields for reduction of N_2 to yield NH_3 varying the buffer loading using either the Blue LED lamps or the H160 390 nm lamp.

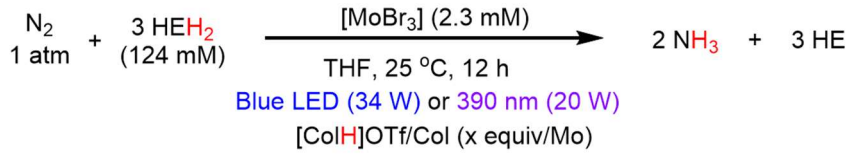

Entry	Lamp and buffer loading	NH_3 (equiv/ Mo)	NH_3 yield/ HEH_2 (%)
1	H160 390 nm, no buffer	0.4 ± 0.3	1.1 ± 0.8
2	H160 390 nm, 5 equiv buffer	6.9 ± 0.3	19 ± 1
3	H160 390 nm, 54 equiv buffer	15.9 ± 1.4	44 ± 4
4	H160 390 nm, 108 equiv buffer	9.2 ± 0.9	26 ± 2.5
5	H160 390 nm, 216 equiv buffer	8.3 ± 0.4	23 ± 1
6	H150 Blue LED, no buffer[a]	0.9 ± 0.2	2.6 ± 0.5
7	H150 Blue LED, 5 equiv buffer[a]	2.9 ± 0.2	8.0 ± 0.6
8	H150 Blue LED, 54 equiv buffer[a]	9.5 ± 1	26.5 ± 3
9	H150 Blue LED, 108 equiv buffer	16 ± 2	44 ± 6
10	H150 Blue LED, 216 equiv buffer[a]	20.3 ± 1.1	56 ± 3

[a] Yields taken from ref 4.

Table D.6. Individual runs for catalytic yields for reduction of N_2 to yield NH_3 when varying the irradiation wavelength (Figure 5.3 and Table D.1).

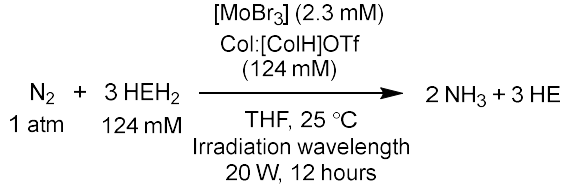

Entry	Lamp	Other Variations	NH_3 (equiv/ Mo)	Yield per HEH_2 (%)
A1	H150 Blue LED	68 W	10.7	30
B1	H150 Blue LED	68 W	13.8	38
C1	H150 Blue LED	68 W	14.9	41
Table D.1, entry 3	**H150 Blue LED**		**13 ± 2**	**36 ± 5**
D1	H160 456 nm		<0.1	<0.3
E1	H160 456 nm		<0.1	<0.3
F1	H160 456 nm		<0.1	<0.3
Table D.1, entry 3	**H160 456 nm**		**<0.1**	**<0.3**
G1	H160 440 nm		2.0	6
H1	H160 440 nm		0.8	2
I1	H160 440 nm		1.8	5
Table D.1, entry 4	**H160 440 nm**		**1.5±0.5**	**4±1**
J1	H160 440 nm	24 hours, 80 W	4.4	**12.2**
K1	H160 440 nm	24 hours, 80 W	**4.9**	**13.6**
Table D.1, entry 5	**H160 440 nm**	**24 hours, 80 W**	**4.6±0.2**	**12.6±0.05**
L1	H160 427 nm		7.5	21
M1	H160 427 nm		5.7	16
Table D.1, entry 6	**H160 427 nm**		**6.6±0.9**	**18±2.5**
N1	H160 427 nm	80 W	20.7	57
O1	H160 427 nm	80 W	18.6	52
P1	H160 427 nm	80 W	21.5	60
Q1	H160 427 nm	80 W	20.6	57
Table D.1, entry 7	**H160 427 nm**	**80 W**	**20.4±0.6**	**57±2**
R1	H160 427 nm	80 W, 0.575 mM Mo	30.8	21.4
S1	H160 427 nm	80 W, 0.575 mM Mo	24.7	17.1
Table D.1, entry 8	**H160 427 nm**	**80 W, 0.575 mM Mo**	**28±3**	**19±2**
T1	390 nm		18.1	50.2
U1	390 nm		15.1	41.9
V1	390 nm		14.2	39.4
W1	390 nm		16.1	44.7
Table D.1, entry 9	**H160 390 nm**		**15.9±1.4**	**44±4**
X1	390 nm	80 W	17.2	47.8
Y1	390 nm	80 W	18.0	50
Table D.1, entry 10	**H160 390 nm**	**80 W**	**17.6±0.4**	**49±1**
Z1	370 nm		3.4	9.4
AA1	370 nm		2.1	5.8
Table D.11, entry 11	**H160 370 nm**		**2.7±0.7**	**7.5±2**

Table D.7. NH_3 yields when varying dihydropyridine and buffer structure. For the benefit of the reader, the discussion is presented in this caption.

In brief, replacing Col-buffer (pK_a 15.0; table D.7, entry 1)[12] with other methylated pyridines showed attenuated efficacy for N_2R; 2,6-dimethylpyridine (Lut, pK_a 14.2; entry 2) buffer yielded 7.1±0.8 and 2-methylpyridine (2-pic, pK_a 13.3; entry 3) yielded 1.7±0.05 equiv NH_3, per Mo. Other buffers, such as more acidic pyridines (entry 4) or structurally distinct alternatives (imidazole, aniline, alkylamine; entry 5) with a similar pK_a to Col, each led to less than 0.4 equiv NH_3 per Mo.

Likewise, canvassing alternative dihydropyridines, we found that HEH_2 was most competent for photodriven N_2R (Table D.7, entries 1 and 6-9). Interestingly, the dihydropyridines we canvassed can be categorized into three groups (Figure D.2, bottom): Hantzsch ester derivates 1,4-dihydropyridines that maintain the ester groups at the 3,5 position and methyl groups at the 2,6 positions (2a-f, entries 6 and 7); 1,4-dihydropyridines with at least one carbonyl group (2g-2i, entry 8); other dihydropyridines (2j-2l, entry 9). Generally, the dihydropyridine that maintains the 3,5-diester functionality produces the most NH_3, suggesting that this motif may be crucial in the parent conditions (HEH_2/Col-buffer).

Varying buffer and dihydropyridine

Entry	Variation from standard conditions	Yield NH_3/Mo
1	None	13 ± 1.7
	Varying buffer (instead of Col-buffer)	
2	Lut as buffer	7.1 ± 0.8
3	2-pic as buffer	1.7 ± 0.1
4	$^{2\text{-MeO}}$pyr, $^{4\text{-Cl-2,6-Me}}$pyr or $^{2,4,6\text{-Ph}}$pyr as buffer	0 − 0.3
5	Imid, $^{4\text{-MeO}}$pyr or Et_3N as buffer	<0.2
	Varying dihydropyridine (instead of HEH_2)	
6	**2a** as dihydropyridine	3.2 ± 0.4
7	**2b-2f** as dihydropyridine	0.4 − 1.9
8	**2g-2i** as dihydropyridine	0.2 − 0.5
9	**2j-k** as dihydropyridine	<0.2

Table D.8. Individual runs for catalytic yields for reduction of N_2 to yield NH_3 when varying the buffer (Table D.7).

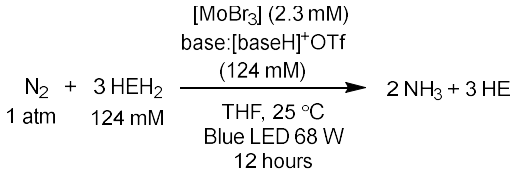

Entry	Base	Notes	NH_3 (equiv/ Mo)	Yield per HEH_2 (%)
A2	Col		10.7	30
B2	Col		13.8	38
C2	Col		14.9	41
Table D.7, entry 1	**Col**		**13 ± 2**	**36 ± 5**
D2	2,6-lutidine		6.4	18
E2	2,6-lutidine		8.0	22
Table D.7, entry 2	**2,6-lutidine**		**7.15±0.8**	**20 ± 2**
F2	2-picoline		1.65	4.6
G2	2-picoline		1.72	4.7
Table D.7, entry 3	**2-picoline**		**1.7±0.05**	**4.7±0.1**
H2	2,6-Me-4-Cl-pyr		0.2	0.6
I2	2,6-Me-4-Cl-pyr		0.4	1.1
Table D.7, entry 4	**2,6-Me-4-Cl-pyr**		**0.3±0.1**	0.8**±0.3**
J2	2,4,6-Ph-pyr		0.1	0.3
K2	2,4,6-Ph-pyr		0.1	0.3
Table D.7, entry 4	**2,4,6-Ph-pyr**		**0.1±0.05**	0.3**±0.15**
L2	2,6-MeO-Pyr		<0.1	<0.3
M2	2,6-MeO-Pyr		<0.1	<0.3
Table D.7, entry 4	**2,6-MeO-Pyr**		**<0.1**	**<0.3**
N2	Et_3N		0.2	0.6
O2	Et_3N		0.1	0.3
Table D.7, entry 4	**Et_3N**		**0.17±0.04**	**0.5±0.11**
P2	Imidazole		<0.1	**<0.3**
Q2	Imidazole		<0.1	**<0.3**
Table D.7, entry 5	**Imidazole**		<0.1	**<0.3**
R2	$^{4\text{-MeO}}PHNH_2$		<0.1	**<0.3**
S2	$^{4\text{-MeO}}PHNH_2$		<0.1	**<0.3**
Table D.7, entry 5	**$^{4\text{-MeO}}PHNH_2$**		<0.1	**<0.3**

Table D.9. Individual runs for catalytic yields for reduction of N_2 to yield NH_3 when varying the dihydropyridine (Table D.7).

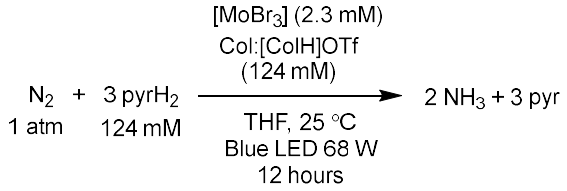

Entry	Dihydropyridine	Notes	NH_3 (equiv/ Mo)	Yield per HEH_2 (%)
A3	HEH_2		10.7	30
B3	HEH_2		13.8	38
C3	HEH_2		14.9	41
Table D.7, entry 1	**HEH_2**		**13 ± 2**	**36 ± 5**
D3	$^{MeO}HEH_2$ (2a)		3.6	10
E3	$^{MeO}HEH_2$ (2a)		2.9	8
Table D.7, entry 6	**$^{MeO}HEH_2$ (2a)**		**3.3 ± 0.4**	**9.0 ± 1.0**
F3	$^{tBuO}HEH_2$ (2b)		0.5	1.4
G3	$^{tBuO}HEH_2$ (2b)		1.1	3.1
Table D.7, entry 7	**$^{tBuO}HEH_2$ (2b)**		**0.7 ± 0.3**	**2±1**
H3	$^{4\text{-}Ph}HEH_2$ (2c)		0.7	1.9
I3	$^{4\text{-}Ph}HEH_2$ (2c)		0.8	2.2
Table D.7, entry 7	**$^{4\text{-}Ph}HEH_2$ (2c)**		**0.75±0.05**	**2.1±0.1**
J3	$^{4\text{-}PhCN}HEH_2$ (2d)		1.85	5.2
K3	$^{4\text{-}PhCN}HEH_2$ (2d)		1.65	4.6
Table D.7, entry 7	**$^{4\text{-}PhCN}HEH_2$ (2d)**		**1.75±0.15**	**4.9±0.4**
L3	$^{N\text{-}Me}HEH_2$ (2e)		1.0	2.8
M3	$^{N\text{-}Me}HEH_2$ (2e)		1.6	4.4
Table D.7, entry 7	**$^{N\text{-}Me}HEH_2$ (2e)**		**1.3 ± 0.3**	**3.6 ± 0.8**
N3	**2f**		2.7	7.5
O3	**2f**		1.1	3
Table D.7, entry 7	**2f**		**1.9±0.8**	**5±2**
P3	**2g**		0.3	0.8
Q3	**2g**		0.3	0.8
R3	**2g**		0.2	0.6
Table D.7, entry 8	**2g**		**0.25±0.04**	0.7**±0.1**

Cont. table D.9				
S3	BNAH (2h)		0.5	1.4
T3	BNAH (2h)		0.3	0.8
U3	BNAH (2h)		0.6	1.7
V3	BNAH (2h)		0.3	0.8
Table D.7, entry 8	**BNAH (2h)**		**0.44±0.13**	**1.2±0.4**
W3	$^{MeNH}HEH_2$ (**2i**)		0.49	1.4
X3	$^{MeNH}HEH_2$ (**2i**)		0.45	1.25

Table D.10. Individual runs for catalytic yields for reduction of N_2 to yield NH_3 when varying the precatalyst.

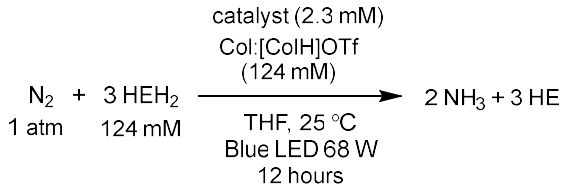

Entry	Catalyst	Notes	NH_3 (equiv/ Mo)	Yield per HEH_2 (%)
A4	[$MoBr_3$]		10.7	30
B4	[$MoBr_3$]		13.8	38
C4	[$MoBr_3$]		14.9	41
	[$MoBr_3$]		**13 ± 2**	**36 ± 5**
D4	[MoNBr]		12.1	34
E4	[MoNBr]		11.4	32
	[MoNBr]		**11.8±0.4**	**33 ± 1**
F4	^{Me}PNPMoBr_3		**7**	19
G4	^{Me}PNPMoBr_3		8.8	24
	^{Me}PNPMoBr_3		**7.9±1.3**	**22 ± 4**
H4	**^{Me2N}PNPMoBr_3**		**6.3**	**17.5**
I4	[$Mo(N_2)_2]_2(\mu\text{-}N_2)$		2.8	7.8
J4	[$Mo(N_2)_2]_2(\mu\text{-}N_2)$		3.2	8.9
	[$Mo(N_2)_2]_2(\mu\text{-}N_2)$		**3.0±0.2**	**8.3±0.6**
K4	$(dape)_2W(N_2)_2$		2.7	7.5
L4	$(dape)_2W(N_2)_2$		1.8	5
	$(dape)_2W(N_2)_2$		**2.25±0.5**	**6.2±1.4**
M4	$(dape)_2W(N_2)_2$	No HEH_2	<0.1	<0.3
N4	$(dape)_2W(N_2)_2$	No HEH_2	<0.1	<0.3
	$(dape)_2W(N_2)_2$	**No HEH_2**	**<0.1**	**<0.3**
O4	$(dppe)_2W(N_2)_2$		0.10	0.3
P4	$(dppe)_2W(N_2)_2$		0.25	0.7
	$(dppe)_2W(N_2)_2$		**0.17±0.07**	**0.5±0.2**

Table D.11. Individual runs for catalytic yields for reduction of N_2 to yield NH_3 when varying the counteranion.

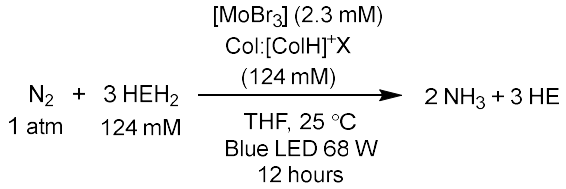

Entry	Counteranion (X)	Notes	NH_3 (equiv/ Mo)	Yield per HEH_2 (%)
A5	$[OTf]^-$		10.7	30
B5	$[OTf]^-$		13.8	38
C5	$[OTf]^-$		14.9	41
	$[OTf]^-$		**13 ± 2**	**36 ± 5**
D5	$[BAr^F{}_4]^-$		5.8	16.1
E5	$[BAr^F{}_4]^-$		4.5	12.5
	$[BAr^F{}_4]^-$		**5.15 ± 0.6**	**14.3±1.7**
F5	$[OTs]^-$		**4.0**	11.1
G5	$[OTs]^-$		2.7	7.5
	$[OTs]^-$		**3.4± 0.6**	**9.4±1.7**
H5	I^-		<0.1	<0.3
I5	I^-		<0.1	<0.3
	I^-		**<0.1**	**<0.3**

D.3. Photoreductions of organic substrates

D.3.1 General procedure

To an oven-dried Schlenk tube HEH_2 (15.6 mg, 62 μmol) and substrate (124 μmol for 1 e^- reduction 62 μmol for 2 e^- reduction, 31 μmol for 4 e^- reduction, 20.6 μmol for 6 e^- reduction and 15.5 μmol for 8 e^- reduction) were added to a Schlenk tube inside the drybox. Dry THF (0.5 mL) with or without 124 mM dissolved buffer was added to the tube, the tube was sealed with a Konte's valve and brought out of the glovebox. The tube was placed in a water bath and irradiated (20 W, H160 427 LED Kessil lamp) for the noted amount of time.

For most substrates, upon completion of the reaction, the solvent was removed *in vacuo*, and a known and weighed amount of 1,3,5-trimethoxybenzene (~3 mg) was added to the tube. Subsequently, the contents of the tube were taken out and analyzed by ^1H NMR, integrating against the TMB standard to calculate the yield of the reaction.

For basic, volatile products (NH_3, propyl amine, trimethylamine), upon completed reaction the tube was frozen to 77 K, and 1 mL NaO^tBu (0.25 M) in MeOH was added via syringe. Upon equilibration, the tube was evacuated, and the contents were vacuum transferred to a receiving flask with 3 mL 2 M HCl in Et_2O. After the transfer, the receiving flask was thawed, and the solvent was removed *in vacuo*. The resulting film was taken up in d_6-DMSO with 10 mM TMB added and analyzed by ^1H NMR to calculate the yield of the reaction.

For some substrates ($tolNO_2$, [TBA][NO_3], and $^{4\text{-Me2N}}PhCHO$), reactivity with additional buffers was analyzed; these results are given in Tables D.12-D.17.

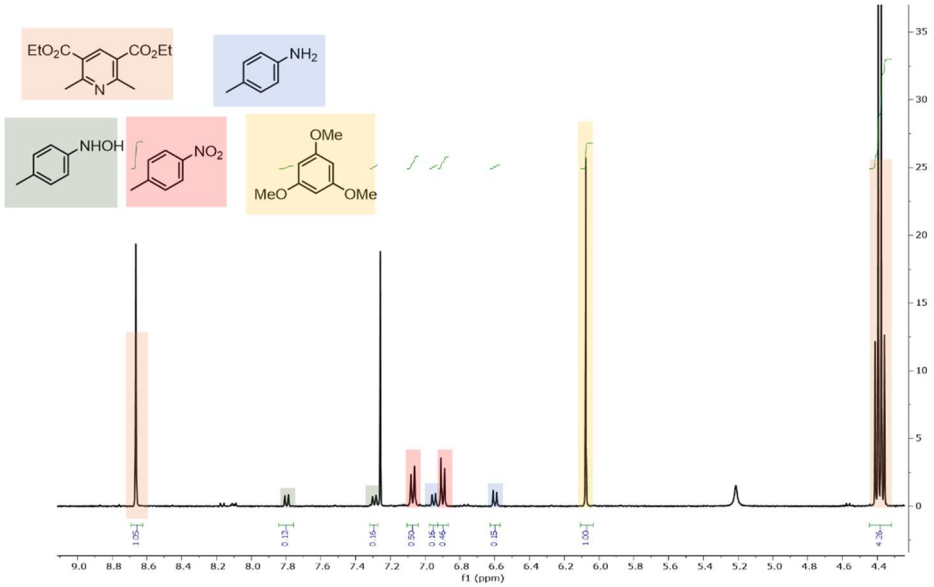

Figure D.4. ^1H NMR ($CDCl_3$ 7.26 ppm) of a typical crude reaction mixture reacting $tolNO_2$ with HEH_2 in the absence of Col-buffer. Identifiable products include: $tolNH_2$ (δ 6.92, d, 2H, J = 8 Hz, δ 6.57, d, 2H, J = 8 Hz, 2H, δ 2.19, s, 3H), tolNHOH (δ 7.07, d, 2H, J = 8 Hz, δ 6.90, d, 2H, J = 8 Hz, 2H, δ 2.28, s, 3H), $tolNO_2$ (starting material) (δ 7.79, d, 2H, J = 8 Hz, δ 7.29, d, 2H, J = 8 Hz, 2H, δ 2.41, s, 3H), along with HE and TMB as indicated.

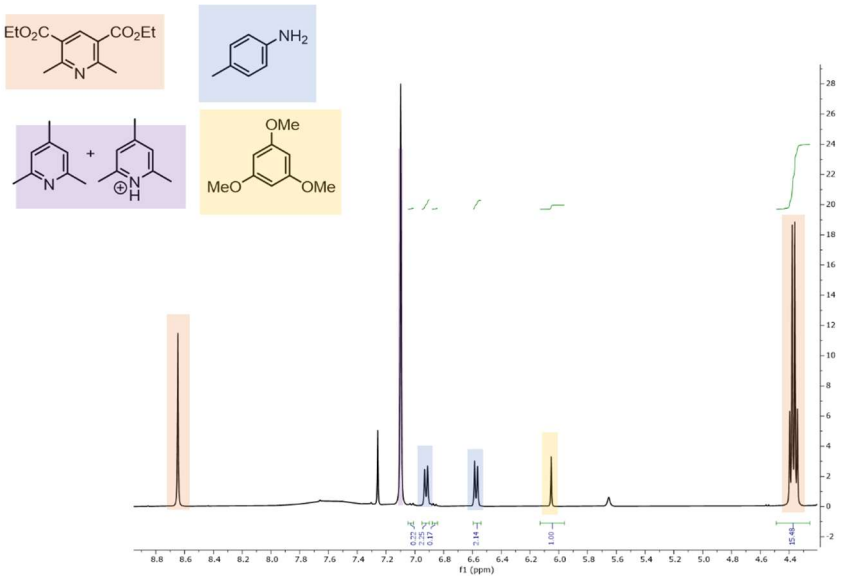

Figure D.5. ^{1}H NMR ($CDCl_3$ 7.26 ppm) of a typical crude reaction mixture reacting $tolNO_2$ with HEH_2 and Col-buffer. Identifiable products include: $tolNH_2$ (δ 6.92, d, 2H, J = 8 Hz, δ 6.57, d, 2H, J = 8 Hz, 2H, δ 2.19, s, 3H), tolNHOH (δ 7.07, d, 2H, J = 8 Hz, δ 6.90, d, 2H, J = 8 Hz, 2H, δ 2.28, s, 3H), $tolNO_2$ (starting material) (δ 7.79, d, 2H, J = 8 Hz, δ 7.29, d, 2H, J = 8 Hz, 2H, δ 2.41, s, 3H), along with HE, Col-buffer and TMB as indicated.

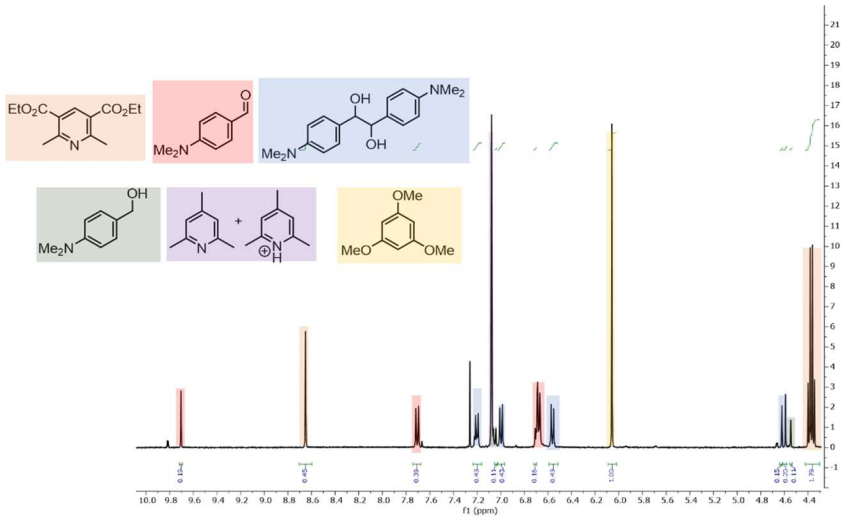

Figure D.6. ^{1}H NMR ($CDCl_3$ 7.26 ppm) of a typical crude reaction mixture reacting ^{4Me2N}PhCHO with HEH_2 and Col-buffer. Identifiable products include: pinacol product *meso* (δ 7.20, d, 4H, J = 8 Hz; δ 6.69 d, 4H, J = 8 Hz; δ 4.63, s, 2H; δ 2.91, s, 12H) and *dl* (δ 7.00, d, 4H, J = 8 Hz; δ 6.57 d, 4H, J = 8 Hz; δ 4.59, s, 2H; δ 2.91, s, 12H), alcohol (δ 7.14, d, 2H, J = 8 Hz; δ 6.69, d, 2H, J = 8 Hz, 2H; δ 4.50, s, 2H; δ 2.28, s, 6H), benzaldehyde (starting material) (δ 9.70, s, 1H; δ 7.71, d, 2H, J = 8 Hz; δ 6.67, d, 2H, J = 8 Hz; 6H, δ 3.10, s, 6H), along with HE, Col-buffer and TMB as indicated.

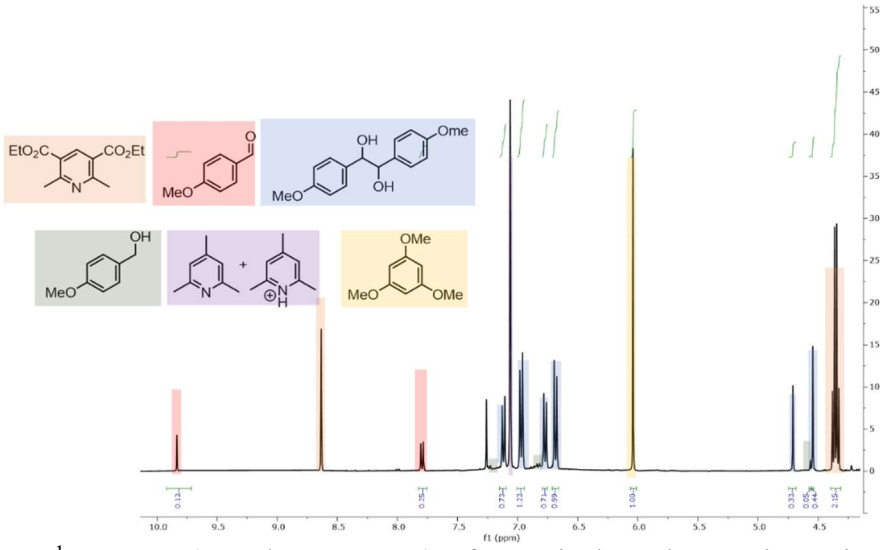

Figure D.7. ^{1}H NMR ($CDCl_3$ 7.26 ppm) of a typical crude reaction mixture reacting ^{4MeO}PhCHO with HEH_2 and Col-buffer. Identifiable products include: pinacol product *meso* (δ 7.12, d, 4H, *J* = 8 Hz; δ 6.77 d, 4H, *J* = 8 Hz; δ 4.74, s, 2H; δ 3.72, s, 6H) and *dl* (δ 6.96, d, 4H, *J* = 8 Hz; δ 6.68 d, 4H, *J* = 8 Hz; δ 4.52, s, 2H; δ 3.72, s, 6H), alcohol (δ 7.23, d, 2H, *J* = 8 Hz; δ 6.82, d, 2H, *J* = 8 Hz, 2H; δ 4.53, s, 2H; δ 3.75, s, 3H), benzaldehyde (starting material) (δ 9.80, s, 1H; δ 7.74, d, 2H, *J* = 8 Hz; δ 6.96, d, 2H, *J* = 8 Hz; 6H, δ 3.86, s, 3H), along with HE, Col-buffer and TMB as indicated.

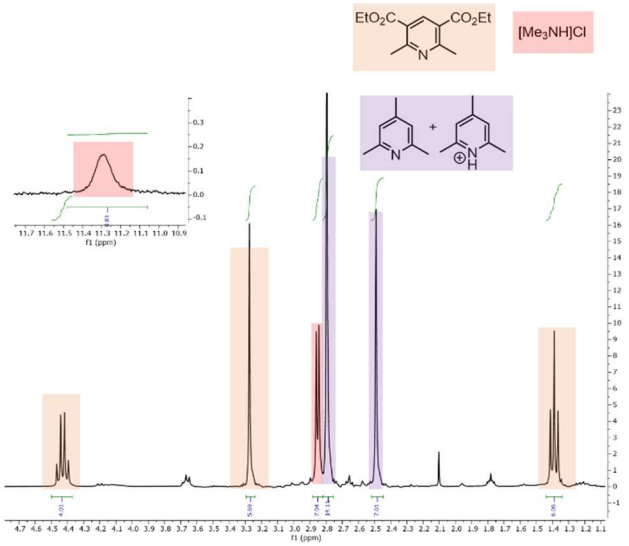

Figure D.8. ^{1}H NMR ($CDCl_3$ 7.26 ppm) of a typical crude reaction mixture reacting Me_3NO with HEH_2 and Col-buffer Typical spectra generated to quantify of products from photoreduction of $tolNO_2$. Identifiable products include: $[Me_3NH]Cl$ (δ 11.28, br, 1H, δ 2.85, d, 9H, *J* = 8 Hz, 2H) along with HE, Col-buffer as indicated.

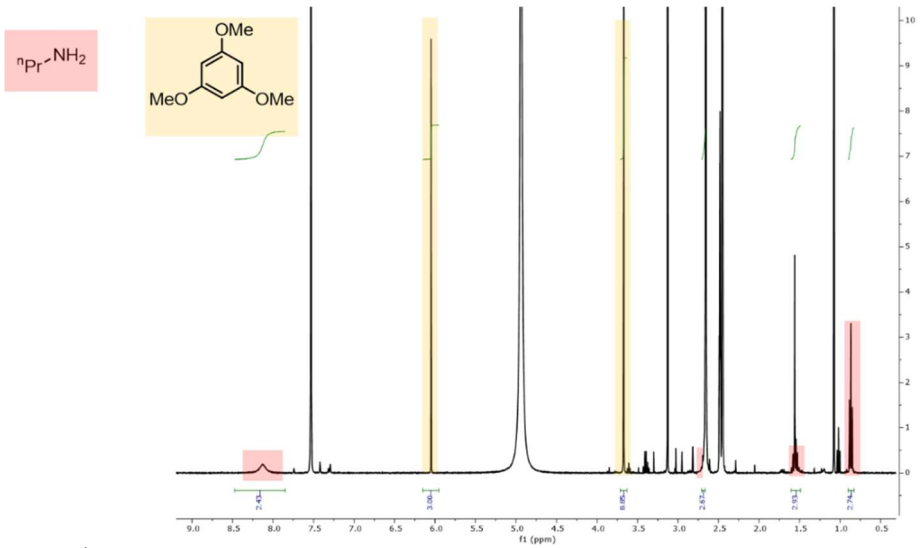

Figure D.9. ^{1}H NMR (DMSO-d_6, 400 MHz) of vac transferred solution following reduction of $^{n}PrNO_2$ by HEH_2 and Col-buffer.

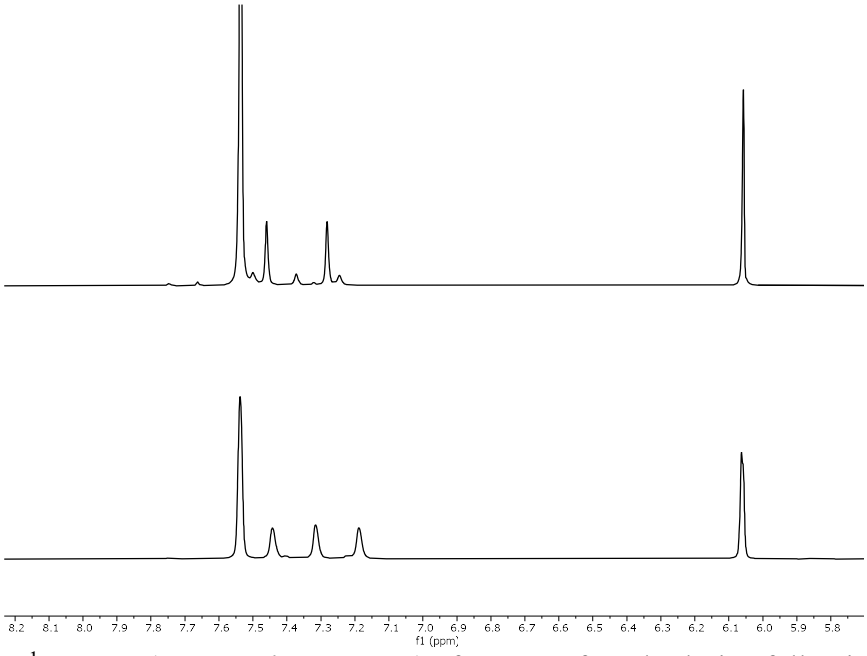

Figure D.10. ^{1}H NMR (DMSO-d_6, 400 MHz) of vac transferred solution following reduction of [TBA][NO_3] by HEH_2 and Col-buffer/ (Top) $^{15}NH_4Cl$ obtained from reaction of natural abundance [TBA]$^{15}NO_3$ with HEH_2 and buffer, under blue light irradiation; (bottom) NH_4Cl obtained from reaction of [TBA]NO_3 with HEH_2 and buffer, under blue light irradiation.

Table D.12. Summary of product yields for $tolNO_2$ reductions.

Entry	Variation from standard conditions	Product yield (% per HEH_2)	
	sub = $tolNO_2$	$tolNHOH$	$tolNH_2$
1	[ColH]OTf/Col buffer	19 ± 14%	77 ± 14%
2	no buffer	31.5 ± 2.5%	13 ± 1%
3	[LutH]OTf/Lut buffer	57±17 %	23±2%
4	[ImidH]OTf/Imid buffer	52 ± 2%	14.9 ± 0.1%
5	Only [ColH]OTf	5%	73%
6	Only Col	56%	22%
7	[$^{2\text{-Me}}$pyrH]OTf/$^{2\text{-Me}}$pyr buffer	40 %	31%
8	[Et_3NH]OTf/Et_3N buffer	11%	26%
9	[$^{4\text{-MeO}}PhNH_3$]OTf/$^{4\text{-MeO}}PhNH_2$ buffer	17%	30%
10	[$^{4\text{-Cl}}$LutH]OTf/$^{4\text{-Cl}}$Lut buffer	50%	0

Table D.13. Yields for individual experiments for $tolNO_2$ reductions.

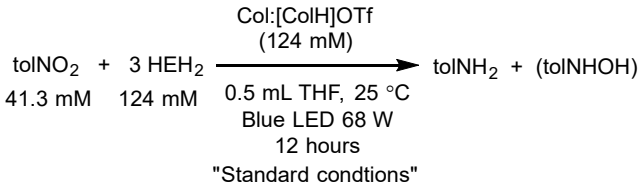

Entry	Variation from standard conditions	Yield $tolNH_2$ (μmol)	Yield $tolNH_2$ per HEH_2 (%)	Yield tolNHOH (μmol)	Yield tolNHOH per HEH_2 (%)	Total yield per HEH_2 (%)
A6	None	19	92	1.5	5	97
B6	None	13	63	7.0	33	96
	None	**16±3**	**77±15**	**4.3±2.7**	**19±14**	**96.5±0.5**
C6	No buffer	2.8	14	9.0	29	43
D6	No buffer	2.4	12	10.6	34	46
	No buffer	**2.6±0.2**	**13±1**	**9.8±0.8**	**31.5±2.5**	**44.5±1.5**
E6	Imid-buffer	3.1	15	15.6	50	65
F6	Imid-buffer	3.0	14.7	16.6	54	69
	Imid-buffer	**3±0.0.05**	**14.8±0.2**	**16.1±0.5**	**52±2**	**67±2**
G6	Lut-buffer	2.1	15	23	74	89
H6	Lut-buffer	5.6	27	12.7	40	67
	Lut-buffer					
I6	Only [ColH]OTf	**15**	**73**	**1.5**	**5**	**78**
J6	Only Col	**4.6**	**22**	**17.2**	**56**	**78**
K6	$^{2\text{-Me}}$pyr-buffer	**6.4**	**31**	**12.5**	**40**	**71**
L6	Et_3N-buffer	**5.4**	**26**	**3.5**	**11**	**37**
M6	$^{4\text{-MeO}}PhNH_2$-buffer	**6.2**	**30**	**5.3**	**17**	**47**
N6	$^{4\text{-Cl-2,6-Me}}$pyr-buffer	**<0.1**	**<0.3**	**15.6**	**50**	**50**

Table D.14. Yields for individual experiments for [TBA][NO_3] reductions.

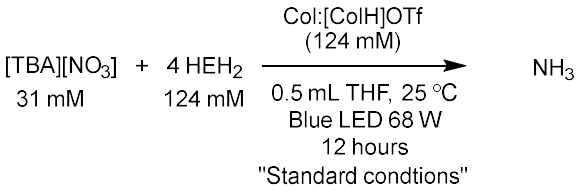

Entry	Variation from standard conditions	Yield NH_3 (μmol)	Yield NH_3 per HEH_2 (%)
A7	None	5.8	37.5
B7	1 mL THF, (unchanged conc)	10.0	32.2
	Col-buffer		**35±3**
C7	No buffer 1 mL THF, (unchanged conc)	0.4	1.4
D7	No buffer 1 mL THF, (unchanged conc)	0.4	1.4
	No buffer		1.4**±0.1**
E7	Imid-buffer	0.11	1.0
F7	Imid-buffer	0.15	1.3
	Imid-buffer		1.2**±0.1**

Table D.15. Yields for individual experiments for 1-nitropropane reductions.

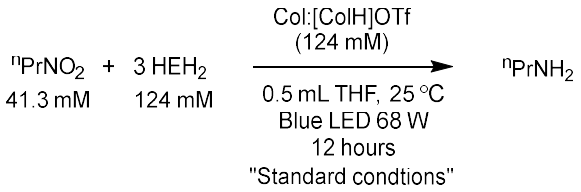

Entry	Variation from standard conditions	Yield $^{n}PrNH_2$ (μmol)	Yield $^{n}PrNH_2$ per HEH_2 (%)
A8	None	5.2	25
B9	None	7.4	36
	Col-buffer	**6.3±1.1**	**30±5**
C9	No buffer	<0.2	<1
D9	No buffer	<0.2	<1
	No buffer	**<0.2**	**<1**

Table D.16. Yields for individual experiments for trimethylamine N-oxide reductions.

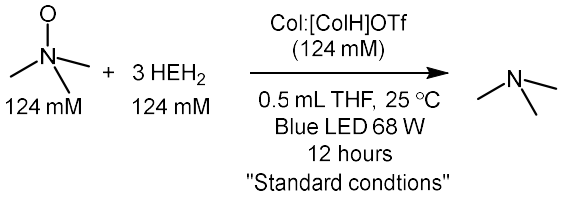

Entry	Variation from standard conditions	Yield Me_3N (μmol)	Yield Me_3N per HEH_2 (%)
A10	None	59.5	96
B10	None	53.2	86
	Col-buffer	**56±3**	**91±5**
C10	No buffer	21.1	34
D10	No buffer	14.2	23
	No buffer	**18±3**	**29±5**

Table D.17. Yields for individual experiments for aldehyde reductions.

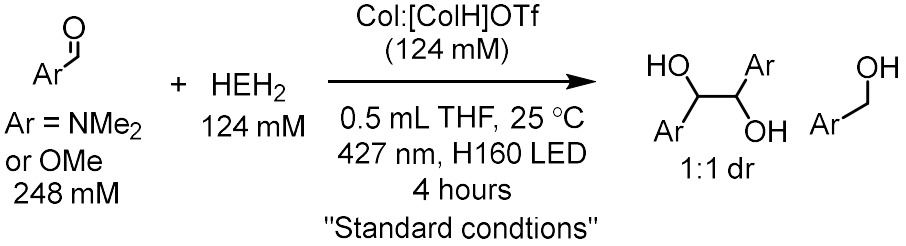

Entry	Variation from standard conditions	Yield pinacol (μmol)	Yield pinacol per HEH_2 (%)	Yield alcohol (μmol)	Yield alcohol per HEH_2 (%)	Total yield per HEH_2 (%)
A11	Ar = NMe_2	31.5	50.8	2.3	3.7	54.7
B11	Ar = NMe_2	30.5	49.2	<1	<2	49.2
C11	Ar = NMe_2	33.5	54.0	<1	<2	54.0
	Ar = NMe_2	**31.8±1.1**	**51.3±1.7**	**<1.5**	**<2.5**	**53±2**
D11	Ar = NMe_2, no buffer	<1.5	<2.5	3.3	5.4	5.4
E11	Ar = NMe_2, no buffer	<1.5	<2.5	3.5	5.6	5.6
	Ar = NMe_2, no buffer	**<1.5**	**<2.5**	**3.4±0.1**	**5.5±0.1**	**5.5±0.1**
F11	Ar = NMe_2, Imid-buffer	**10.6**	**17.1**	**<0.5**	**<1**	**17.1**
G11	Ar = NMe_2, only [ColH]OTf	**11.5**	**18.5**	**11.6**	**18.7**	**37.2**
H11	Ar = NMe_2, only Col	**10**	**16.1**	**<0.5**	**<0.1**	**16.1**
I11	Ar = OMe	54.5	87.9	2.4	3.8	91.7
J11	Ar = OMe	55.3	89.2	1.2	1.9	91.1
		54.9±0.4	**88.6±0.7**	**1.8±0.6**	**2.9±0.9**	**91.4±0.4**
K11	Ar = OMe, No buffer	16.4	26.4	2.4	3.8	30.2
L11	Ar = OMe, No buffer	17.6	28.3	2.2	3.5	31.8
	Ar = OMe, No buffer	**17.0±0.4**	**27.4±0.9**	**2.3±0.1**	**3.6±0.2**	**31.0±0.8**

D.3.2 Light on/off study of tolNO$_2$ reduction

A J. Young-NMR tube was loaded with 124 mM HEH$_2$, 124 mM Col-buffer, and 41.3 mM tolNO$_2$ in 0.7 mL d_8-THF. A spectrum (time =0) was collected, with care being taken to avoid additional irradiation of the NMR tube. Subsequently, the tube was irradiated for 10 minutes, and ^{1}H NMR was collected. The tube was then kept in the dark, and the NMR was recollected. This procedure was continued as indicated in **Figure D.11.**

It was observed that tolNO$_2$ was nearly completely consumed before tolNH$_2$ formation began. Formation of both tolNH$_2$ and tolNHOH was associated with consumption of HEH$_2$. However, upon extended irradiation, tolNHOH does decompose slightly to give more tolNH$_2$, but this is a minor contribution to the total tolNH$_2$ formation.

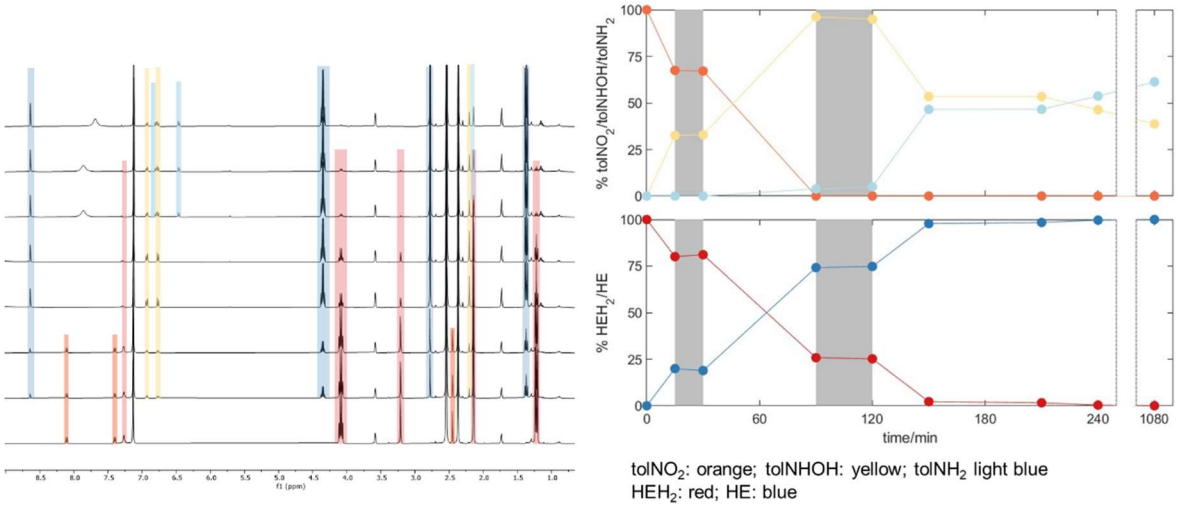

Figure D.11. Light on/off study for tolNO$_2$ reduction. Left panel shows spectra collected from t = 0 (bottom) to 1080 min (top). tolNO$_2$ and HEH$_2$ species are tracked with irradiation off indicated by greyed-out panels in the right panel.

D.3.3 Chemical quantum yield measurements

The organic reaction quantum yield reactions were setup as the uncatalyzed chemical reactions (D.4.1), the H160 427 nm light lamps were used with 10 W irradiation and 15-minute reaction time. The rate (in μmol min^{-1}) was compared to the rate of photon flux measured in this setup.

D.3.3.1 Actinometry measurement

Relative quantum yield was determined through the potassium ferrioxalate chemical actinometry method to determine the light intensity for the setup used for quantum yield experiments (10 W, 427 nm Blue LED). $K_3Fe(C_2O_4)_3$ was prepared and used in solution by making a 10 mM Fe_2SO_4 and 60 mM $K_2C_2O_4$ stock solution in 4% H_2SO_4 (aq). 3 mL of this solution was irradiated at 390 nm for 5 seconds in the same setup as employed for all reactions. Care was taken to minimize light exposure between irradiation cycles.[13]

$$2Fe^{3+} + C_2O_4^{2-} \xrightarrow{h\nu} 2Fe^{2+} + 2CO_2$$

A 0.2% by weight solution of 1,10-phenanthroline in water and a 0.6 M NaOAc buffer in 1% H_2SO_4 (aq) were prepared separately. A 100 µL aliquot of the irradiated solution was placed into a 10 mL volumetric flask along with 200 µL of the phenanthroline solution and 50 µL of buffer, and the solution was diluted with water. The complexation of Fe^{2+} with 1,10-phenanthroline resulted in a bright red solution that had a characteristic absorption at 510 nm. For the control, these steps were repeated with a 100 µL aliquot of non-irradiated solution.

Because complete conversion was not reached after 10 s, but rather sometime between 5 and 60 s, the runs at 10 s were chosen for analysis. These gave an average absorbance of 0.366 ± 0.02 at 510 nm vs. dark.

$$I\ (\text{mol} \cdot \text{min}^{-1}) = \frac{AV_2V_3}{\varepsilon b \phi_\lambda t V_1} \quad (\text{eqn } A5.1)$$

where

A = absorbance at 510 nm

V_2 = volume of actinometer irradiated (0.5 mL)

V_3 = final volume of quantified sample (10 mL)

ε = extinction coefficient of ferrous 1,10-phenanthroline at 510 nm (~1.11×10^4 $M^{-1} \cdot cm^{-1}$)

b = path length of cuvette (1 cm)

ϕ_λ = quantum yield of ferrous production at 427 nm (~1.11)

t = irradiation time (10 s)

V_1 = volume of aliquot of an irradiated sample taken (100 µL).

Giving a light intensity in mol of photons per unit time. Using the gathered absorbance data, a light intensity of $9 \pm 0.5 \times$ µmol · min^{-1} was obtained, and this photon flux was used to calculate all relative quantum yields.

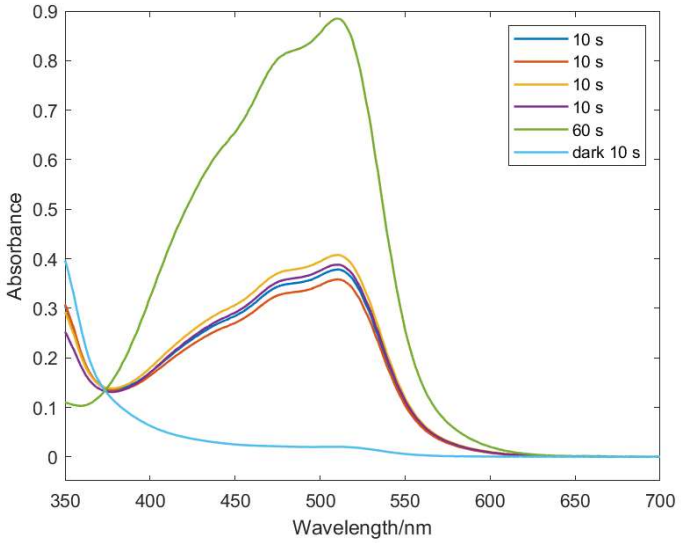

Figure D.12. UV-vis spectra of solutions used for light intensity quantification at different irradiation times.

D.3.2 Individual experiments for chemical quantum yield results

Table D.18. Yields for individual experiments for tolNO$_2$ reductions for quantum yield measurements (Figure 5.8).

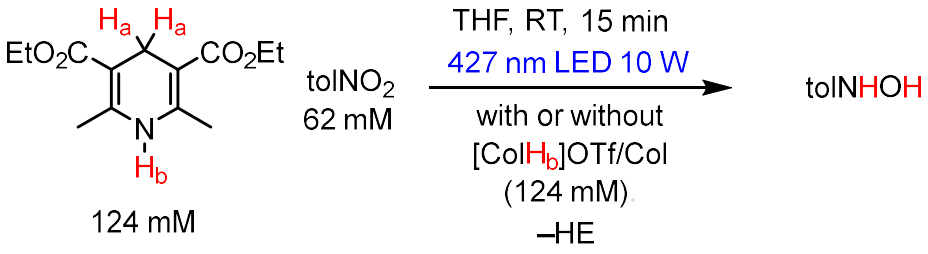

Entry	Variation from standard conditions	Yield tolNHOH (μmol)	Rate (μmol min^{-1})	Quantum yield (x100)	Notes
A12	None	3.5			
B12	None	4.1			
C12	None	3.7			
D12	None	4.0			
	None	**3.8±0.16**	**0.25±0.011**	**0.028±0.0015**	
E12	No buffer	0.6			
F12	No buffer	0.9			
	No buffer	**0.75±0.21**	**0.05±0.014**	**0.006±0.002**	
G12	Only [ColH]OTf	2.9			
H12	Only [ColH]OTf	2.2			
	Only [ColH]OTf	**2.5±0.5**	**0.17±0.03**	**0.019±0.004**	
I12	Only Col	2.25			
J12	Only Col	1.7			
	Only Col	**2.0±0.4**	**0.13±0.03**	**0.015±0.003**	
K12	H_a = D	3.9			
L12	H_a = D	3.8			
M12	H_a = D	3.7			
N12	H_a = D	4.0			
	H_a = D	**3.85±0.07**	**0.26±0.005**	**2.88±0.06**	**KIE = 0.99±0.06**
O12	H_b = D	5.2			
P12	H_b = D	4.2			
Q12	H_b = D	4.2			
R12	H_b = D	4.6			
	H_b = D	**4.6±0.3**	**0.30±0.02**	**3.4±0.2**	**KIE = 0.84±0.09**
S12	*N*-MeHEH$_2$ (2c), Col-buffer	0.93			
T12	*N*-MeHEH$_2$ (2c), Col-buffer	1.00			
	***N*-MeHEH$_2$ (2c), Col-buffer**	**0.97±0.03**		**0.007±0.00025**	
U12	*N*-MeHEH$_2$ (2c), No buffer	0.16			
V12	*N*-MeHEH$_2$ (2c), No buffer	0.29			
	***N*-MeHEH$_2$ (2c), No buffer**	**0.22±0.06**		**0.0016±0.0004**	

Table D.19. Yields for individual experiments for aldehyde reductions for quantum yield measurements.

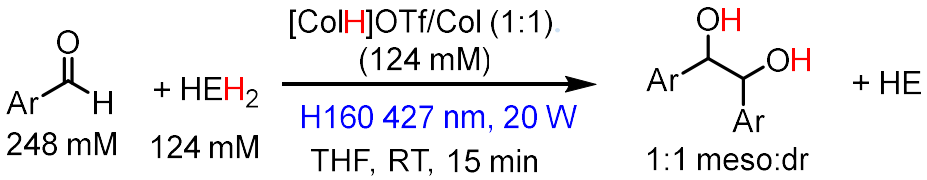

Entry	Variation from standard conditions	Yield tolNHOH (μmol)	Rate (μmol min^{-1})	Quantum yield (x100)
A13	R = NMe_2	11.8		
B13	R = NMe_2	13.7		
	R = NMe_2	**12.75±0.9**	**0.85±0.06**	**0.094±0.008**
C13	R = NMe_2, No buffer	<0.5		
D13	R = NMe_2, No buffer	<0.5		
	R = NMe_2, No buffer	**<0.5**	**<0.03**	**<0.003**
E13	R = OMe	13.2		
F13	R = OMe	13.4		
	R = OMe	**13.3±0.1**	**0.887±0.007**	**0.0986±0.0008**
G13	R = OMe, No buffer	2.8		
H13	R = OMe, No buffer	3.4		
	R = OMe, No buffer	**3.1±0.3**	**0.21±0.02**	**0.023±0.002**

D.4: UV-vis spectroscopy

D.4.1 General procedure

All solutions for UV-vis measurements were prepared inside a glovebox using dried solvent unless otherwise specified. For static spectra (Figures D.13, D.14, D.16 and D.17) an oven-dried cuvette was used and sealed with a Teflon valve.

For titration experiments (Figure D.15), an oven-dried cuvette was loaded in the glove box and sealed with a septum. The titrant was added via syringe against a counterflow of N_2 to maintain an O_2-free atmosphere throughout the experiment.

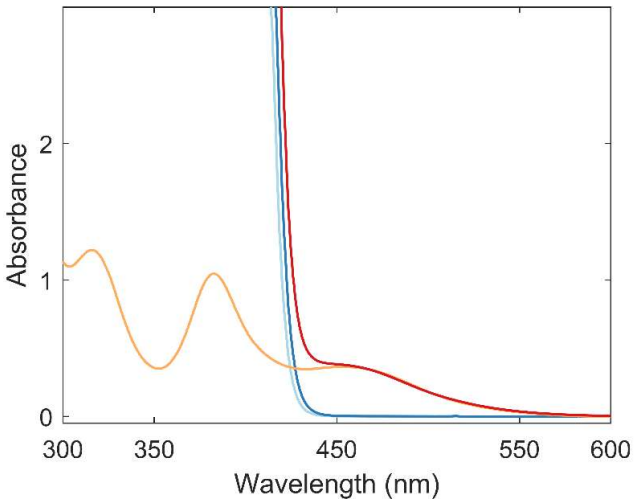

Figure D.13. UV-vis spectra of reaction components in 1 mm cuvette in THF at 25 °C. Traces are [$MoBr_3$], 2.3 mM (yellow); HEH_2 124 mM (light blue); HEH_2 + Col-buffer 124 mM (dark blue), and all reaction components (red trace).

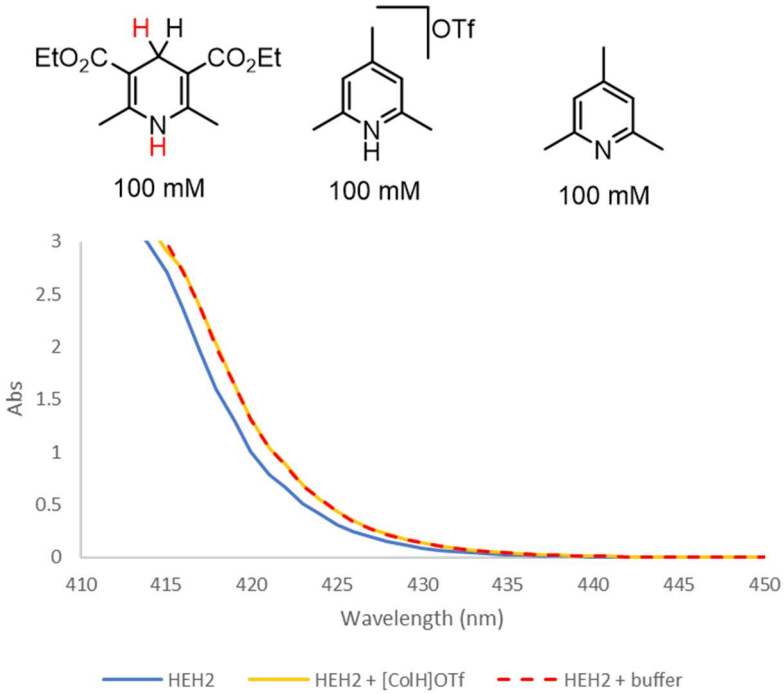

Figure D.14. UV-vis spectra of HEH_2 (100 mM; light blue); HEH_2 + [ColH]OTf (100 mM each; yellow), and HEH_2 + [ColH]OTf + Col (100 mM each; red dashed) collected in a 1 cm cuvette in THF at 25°C.

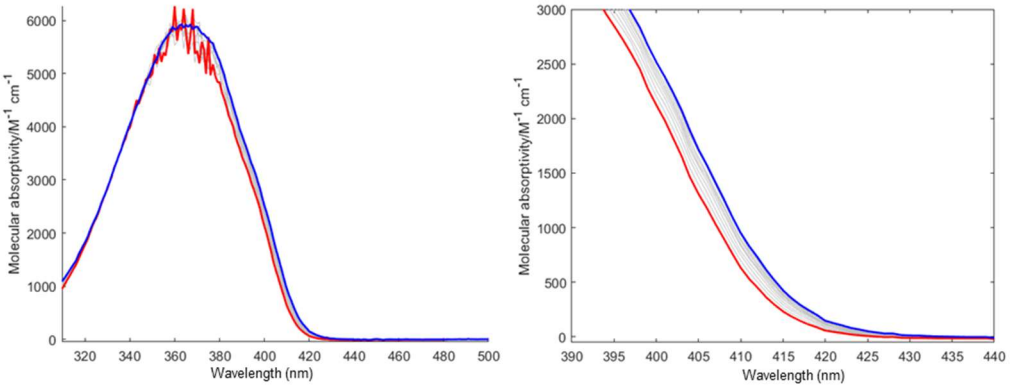

Figure D.15. UV-vis spectra of HEH_2 (0.1 mM) with [ColH]OTf titrated from 0 (red) to 160 mM (blue). Collected in a 1 cm cuvette in THF at 25°C.

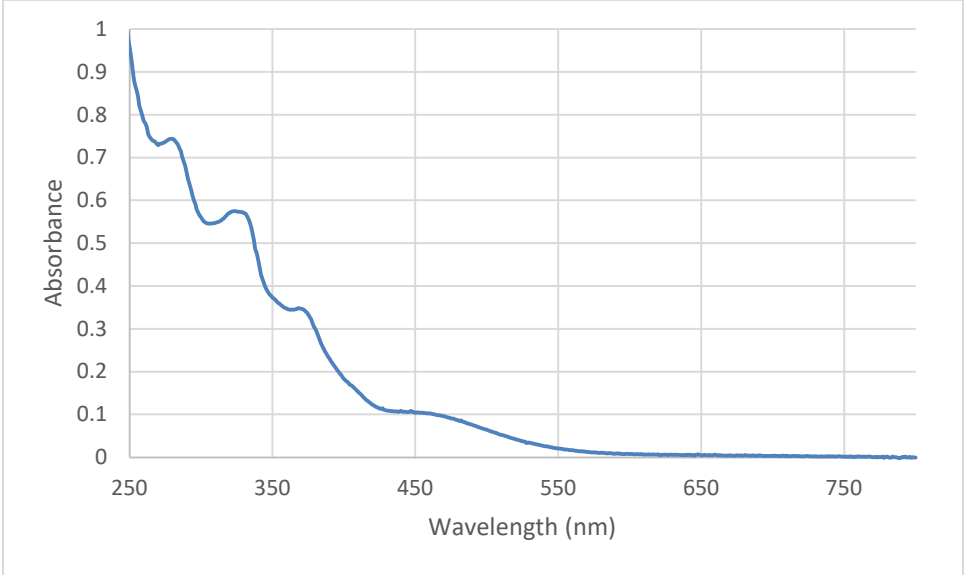

Figure D.16. UV-vis spectra of $PCPMoCl_3$ (0.1 mM) in a 1 cm cuvette in THF at 25°C.

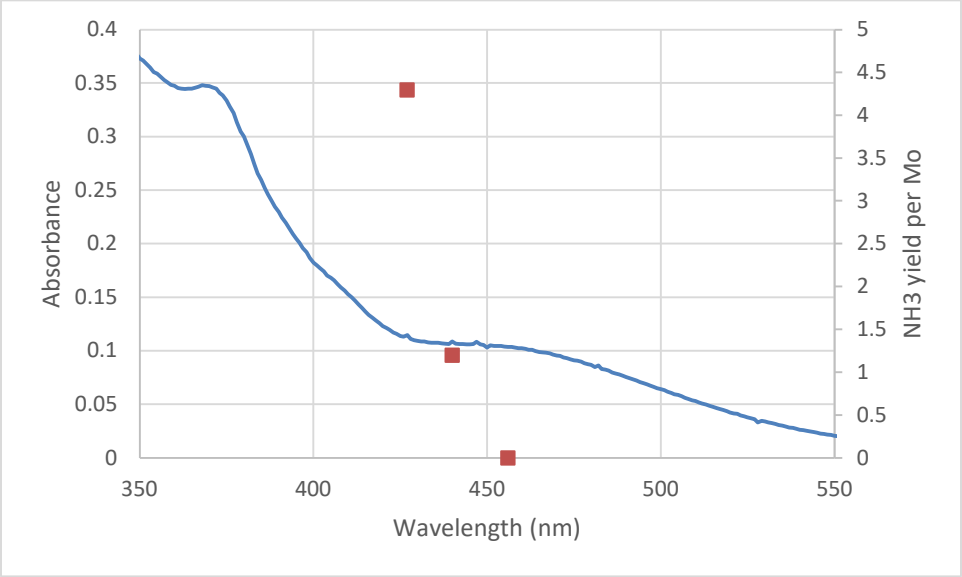

Figure D.17. UV-vis spectra of $PCPMoCl_3$ (0.1 mM) in a 1 cm cuvette in THF at 25°C with NH_3 yields from photodriven N_2R overlayed (from table D.3).

D.5 Fluorescence experiments

D.5.1General procedure

Steady-state fluorimetry was performed in the Beckman Institute Laser Resource Center (California Institute of Technology). Samples for luminescence measurements were prepared in dry THF and transferred to a 1-cm path length–fused quartz cuvette sealed with a high-vacuum Teflon valve (Kontes). Steady-state emission spectra were collected on the Jobin S4 Yvon Spec Fluorolog-3-11 with a Hamamatsu R928P photomultiplier tube detector with photon counting.

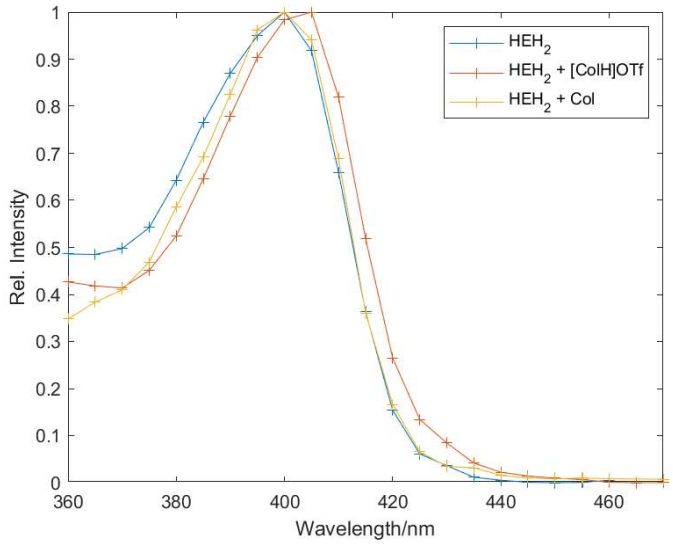

Figure D.18. Excitation spectra monitoring relative emission intensity (500 nm) of HEH_2 (0.5 mM) in the absence (blue trace) presence of [ColH]OTf (320 mM, orange trace) or Col (320 mM, yellow trace). A slight blue-shift is observed with HEH_2 and [ColH]OTf, as is also observed by UV-vis.

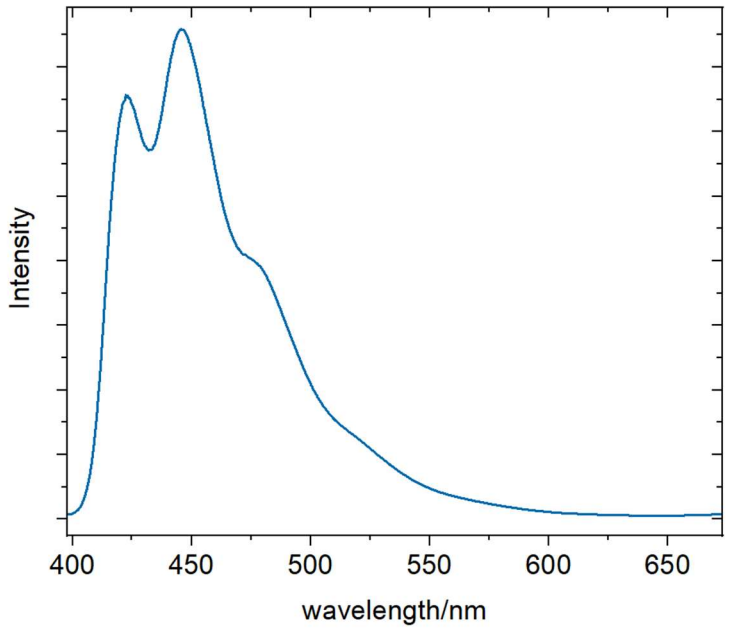

Figure D.19. Low temperature (77 K) emission spectrum of HEH_2 (1.2 mM) in THF. (Excitation wavelength: 355nm).

D.5.2 Fluorescence Quantum yield measurements

Fluorescence quantum yield of HEH_2 was measured against a 9,10-diphenyl anthracene standard (taken to be 1.0 in THF at 380 nm irradiation). Solution of both samples prepared such that the absorbance <0.1, and the integrated emission spectra upon exciting at 380±5 nm. Due to the low signal-to-noise ratio of 10x (100 ms vs 10 ms), integration time was required for HEH_2. The equation:

$$\frac{QY_{\mathrm{HEH2}}}{QY_{\mathrm{anth}}} = \frac{\int \mathrm{emission}_{\mathrm{HEH2}}}{\int \mathrm{emission}_{\mathrm{anth}}} \left(\frac{\mathrm{abs}_{\mathrm{anth,380}}}{\mathrm{abs}_{\mathrm{HEH2,380}}}\right) * \left(\frac{1}{10}\right) \quad \text{(eqn D. 2)}^{14}$$

gives $QY_{HEH2} = 0.018$. The factor of 1/10 is required due to the 10x longer integration time for the HEH_2 emission spectra. See **Figure D.20**.

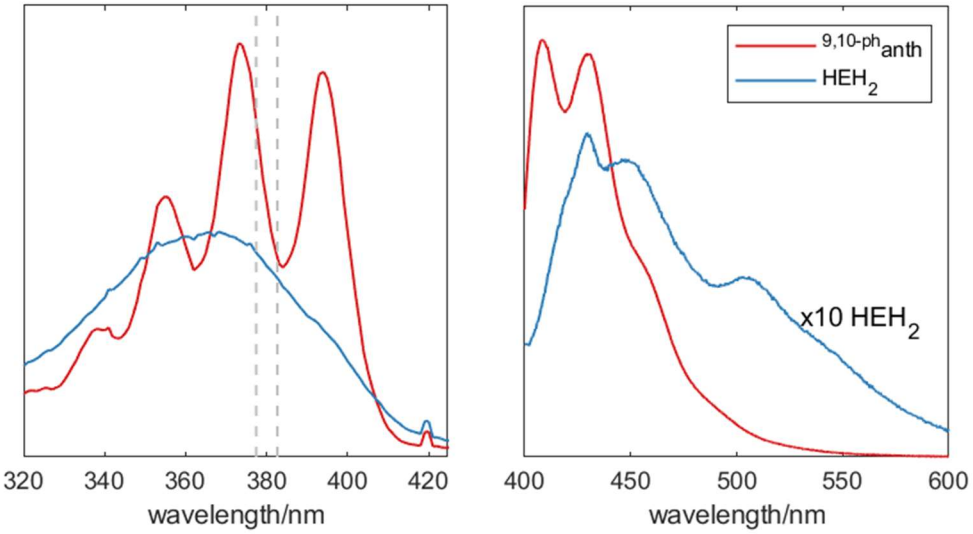

Figure D.20. Absorption spectra and emission spectra of HEH_2 and 9,10-diphenylanthracene. Note that HEH_2 is multiplied by 10x in the emission spectra, and generated using 10x integration time, resultingly the final integral is about 1/100 the intensity of 9,10-diphenylanthracene.

D.5.3 Quenching studies

D.5.3.1 Procedure for quenching studies

1 cm quartz glass cuvettes were loaded with 0.5 mM HEH_2 solutions in dry THF, with varying concentrations of quencher (either Col or [ColH]OTf) in a nitrogen glovebox. Stock solutions were used to assure consistency. Solutions were excited at 390 nm wavelength to avoid interference of the excitation wavelength and steady-state fluorescence spectra. Experiments were conducted at 23 °C.

D.5.3.2 Calculation of Stern-Volmer quenching constants

Using the previously measured excited state-lifetime measured (τ_0) for HEH_2 we can calculate the Stern-Vollmer quenching both via a diffusional constant (k_{diff}) and an equilibrium static quenching constant (K_{stat}) using the equation:

$$I_0/I_c = 1 + (k_{diff} \cdot \tau_0 + K_{stat})\,[Q] + (k_{diff} \cdot \tau_0 \cdot K_{stat})\,[Q]^2 \quad \text{(eqn D.3)}.^{14}$$

K_q and τ_0 are given by the lifetime quenching ($6.7\ 10^9\ M^{-1}\ s^{-1}$ and 200 ps, respectively; see figure D.23) to give $k_{diff} \cdot \tau_0 = 1.34\ M^{-1}$. Accordingly, an updated model (red line, figure D.21) uses $K_{stat} = 20\ M^{-1}$. This suggests slightly less static quenching compared to when solely static quenching is assumed ($22\ M^{-1}$, dashed, blue line).

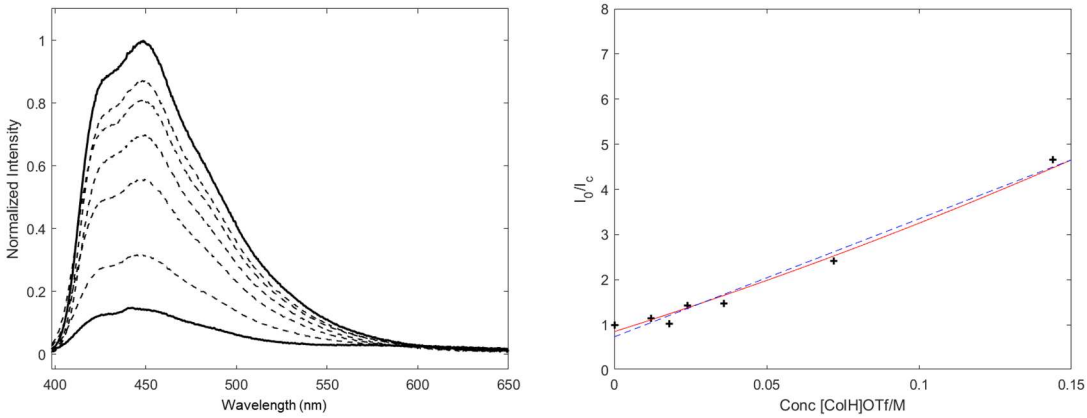

Figure D.21. Steady-state fluorescence of HEH_2 (0.5 mM) with varying amounts of [ColH]OTf (18 mM to 144 mM) (Left). Stern-Vollmer quenching plot of I_0/I_C against concentration of [ColH]OTf (right). Two models are presented, one assuming only static

quenching (blue dashed line) and one considering static and diffusional quenching as determined by luminescence lifetimes (red line).

Given the much lower value of the luminescence lifetime, adding this factor is not required based on this data, but as the luminescence spectroscopy suggests, it is present. The addition does improve the model slightly, as would be expected.

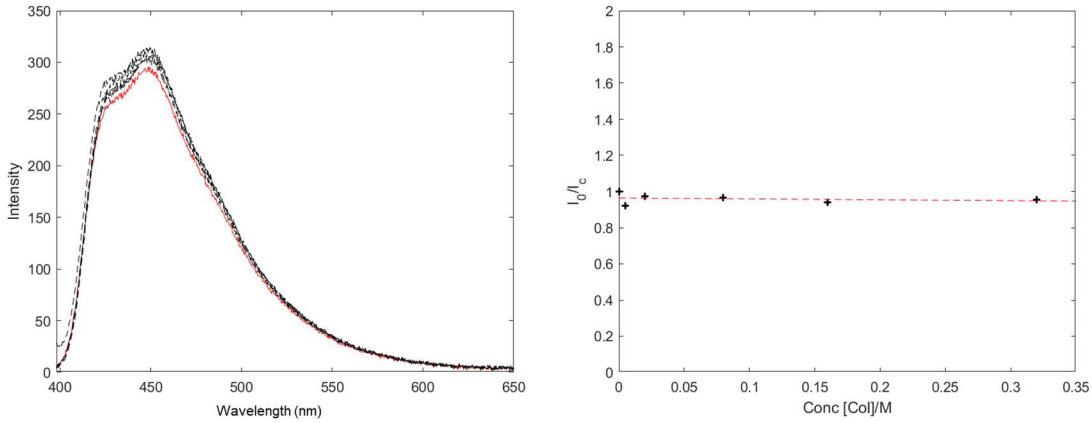

Figure D.22. Steady-state fluorescence of HEH_2 (0.5 mM) with varying amounts of Col (5 mM to 320 mM) (left). Stern-Vollmer quenching plot of I_0/I_C against concentration of Col (right). Slope is -0.05±0.1 M^{-1}, suggesting little to no quenching.

D.6 Time-resolved luminescence experiments

D.6.1 General procedure

Time-resolved luminescence measurements and transient absorption measurements were carried out in the Beckman Institute Laser Resource Center at Caltech. All measurements were performed with samples under an N_2 atmosphere at room temperature. Samples were prepared in air-tight 1 cm path-length quartz cuvettes in the dark, N_2-filled glovebox. Prior to measurement, all samples were protected from light by wrapping in aluminum foil.

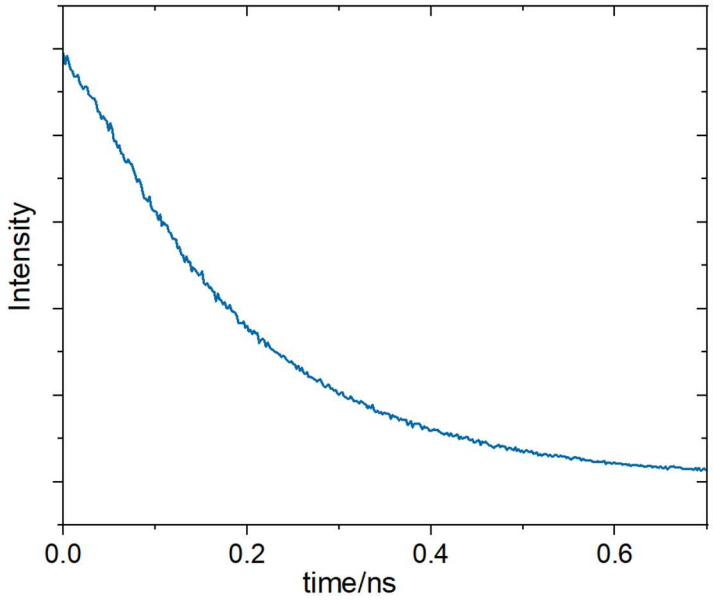

Figure D.23. Luminescence lifetime of HEH_2 (1.2mM) in THF. (Excitation wavelength: 355nm, detection wavelength: 450 nm).

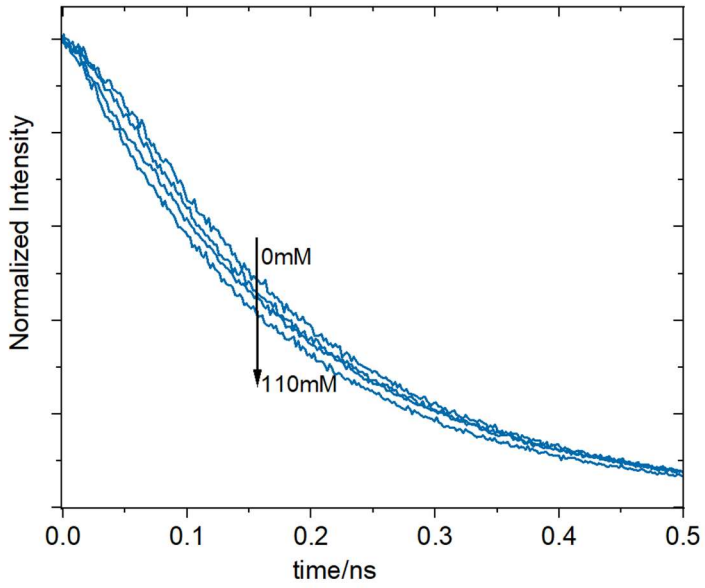

Figure D.24. Luminescence lifetime of HEH_2 (1.2mM) in THF after titration with [ColH]OTf (50mM-110mM). (Excitation wavelength: 355nm, detection wavelength: 450 nm).

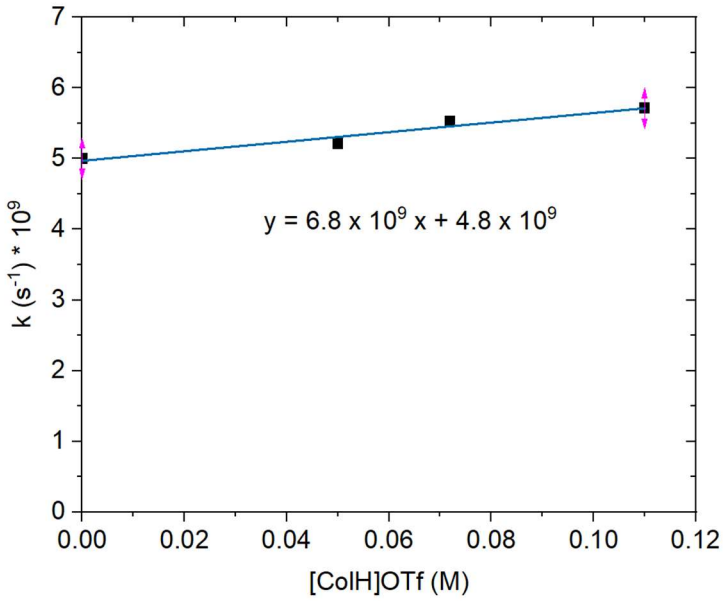

Figure D.25. Kinetic constants plot extrapolated from luminescence lifetime of HEH_2 (1.2mM) in THF after titration with [ColH]OTf (50mM-110mM).

Table D.20. Luminescence lifetime of HEH_2 (1.2mM) in THF after titration with [ColH]OTf (50mM-110mM).

	Lifetime
HEH_2	200 ps ± 10
HEH_2 + ColH (50mM)	192 ps ± 5
HEH_2 + ColH (72mM)	181 ps ± 4
HEH_2 + ColH (110 mM)	175 ps ± 9

D.6.2 Studies of [$MoBr_3$] luminescence

In addition to the study of HEH_2, we have also investigated the photophysical properties of [$MoBr_3$]. We find that excitation at 450 nm does result in the formation of a long-lived excited state. Importantly, this excited state is not quenched by HEH_2 both in the

presence and absence of buffer, supporting that HEH_2 is the photosensitizer during N_2R (Figures D.26-D.28).

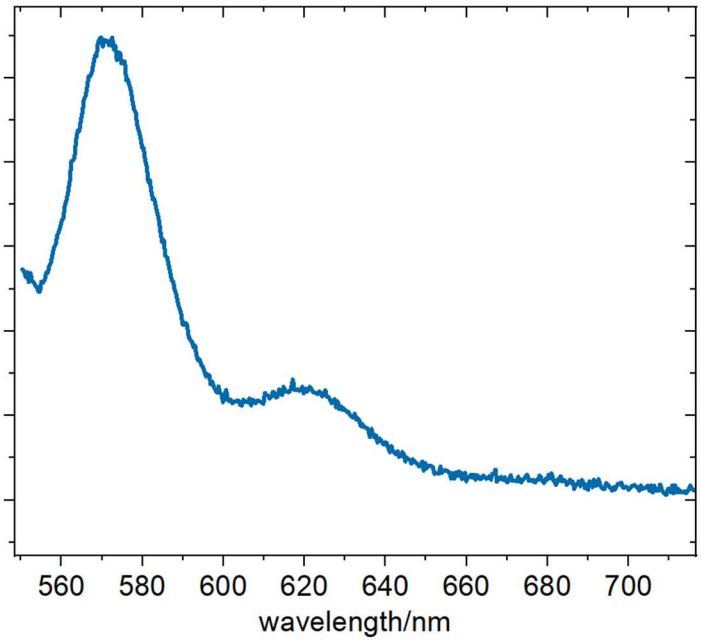

Figure D.26. Emission spectrum of [$MoBr_3$] in THF (0.1 mM; Excitation: 450nm).

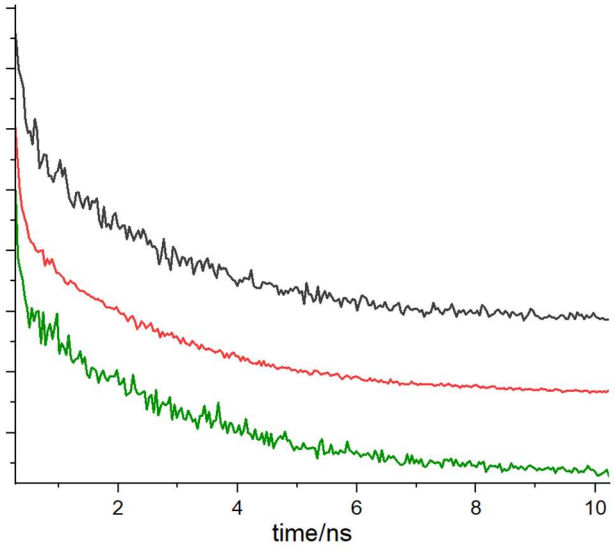

Figure D.27. Luminescence lifetime of [$MoBr_3$] (0.5 mM) in THF after titration with HEH_2 0 equiv (black), 25 equiv (red), 50 equiv (green) (Excitation: 450nm, Detection: 570 nm). Translated to more clearly show traces.

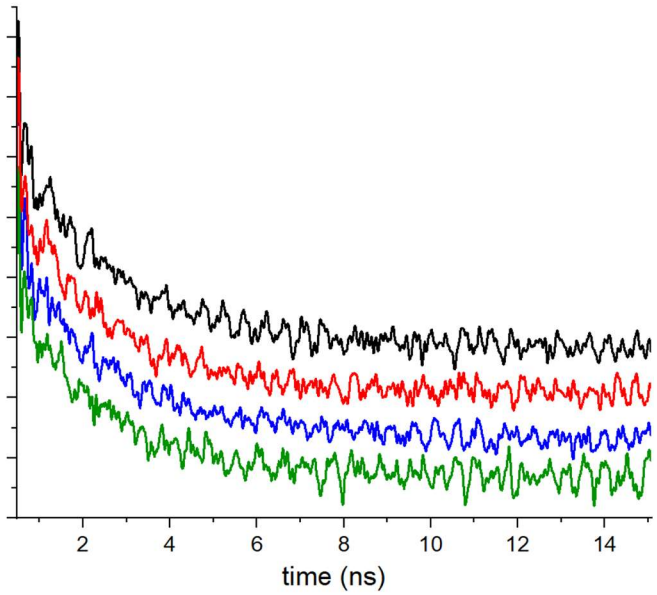

Figure D.28. Luminescence lifetime of [$MoBr_3$] (0.5 mM, black trace) in THF after addition of HEH_2 (50 equiv, red trace), HEH_2 (50 equiv), and 100 equiv of Buffer (blue trace) and HEH_2 (50 equiv) and 200 equiv of Buffer (green trace) (Excitation: 450nm, Detection: 570 nm). Translated to more clearly show traces.

D.7 Transient Absorption Studies

D.7.1 General procedure.

Transient absorption measurements were carried out in the Beckman Institute Laser Resource Center at Caltech. All measurements were performed with samples under an N_2 atmosphere at room temperature. Samples were prepared in air-tight 1 cm path-length quartz cuvettes in the dark, N_2-filled glovebox. Prior to measurement, all samples were protected from light by wrapping in aluminum foil.

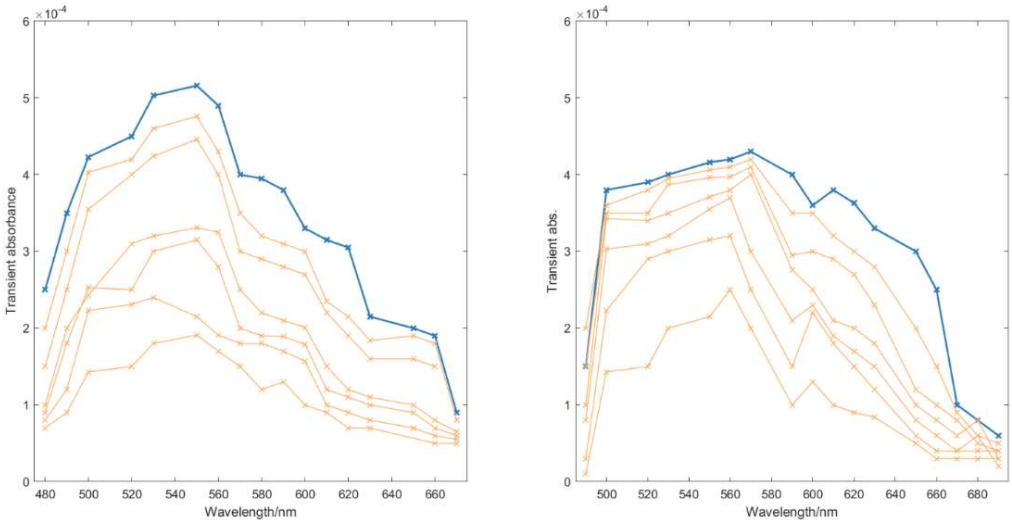

Figure D.29. TA spectrum of short-lived radical species generated from excitation (355 nm) of HEH_2 (1.2 mM) in the presence of [ColH]OTf (12 mM) and [ColH]OTf + Col (12 mM). Intensity decreases from 1.5 μs (blue trace) to 35 μs.

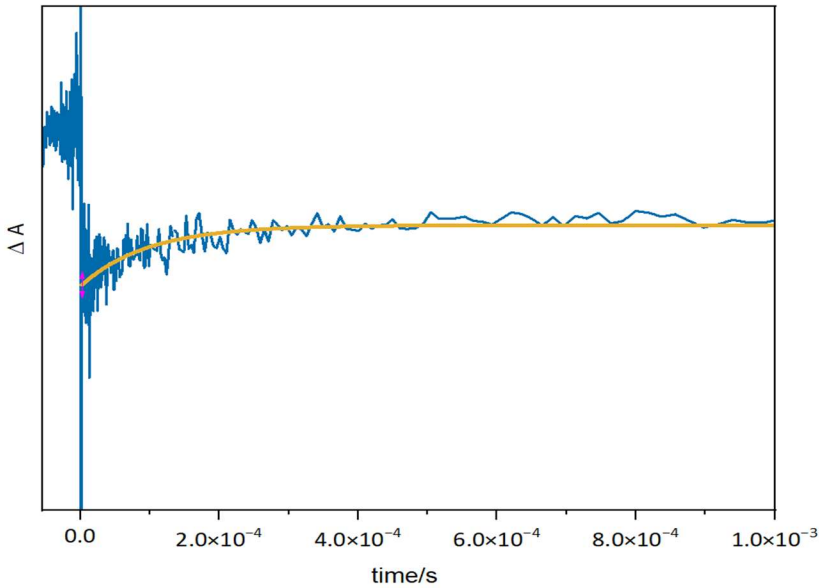

Figure D.30. Bleaching at 370 nm generated from HEH_2 (1.2 mM) in THF. (Excitation wavelength: 355nm, detection wavelength: 370 nm).

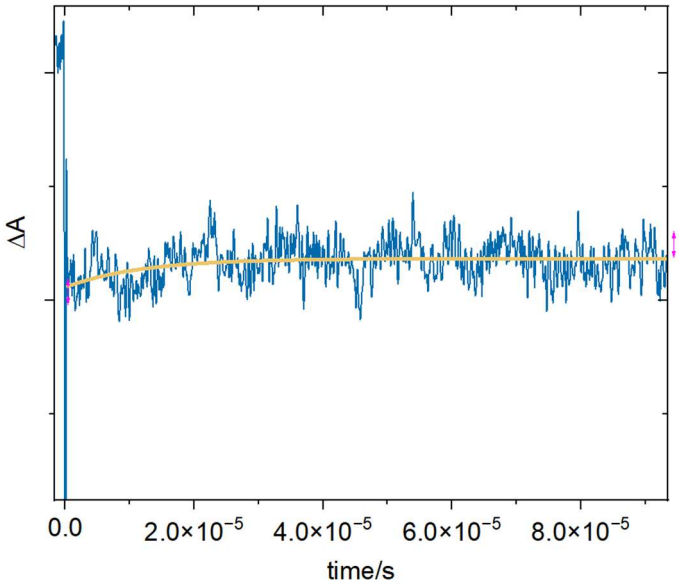

Figure D.31. Bleaching at 370 nm generated from HEH_2 (1.2 mM) in THF in the presence of [ColH]OTf (12 mM). (Excitation wavelength: 355nm, detection wavelength: 370 nm).

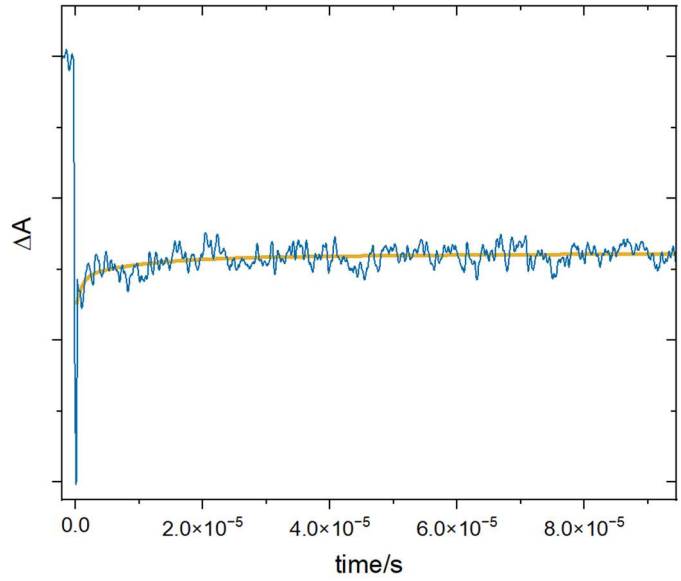

Figure D.32. Bleaching at 370 nm generated from HEH_2 (1.2 mM) in THF in the presence of [ColH]OTf (110 mM). (Excitation wavelength: 355nm, detection wavelength: 370 nm).

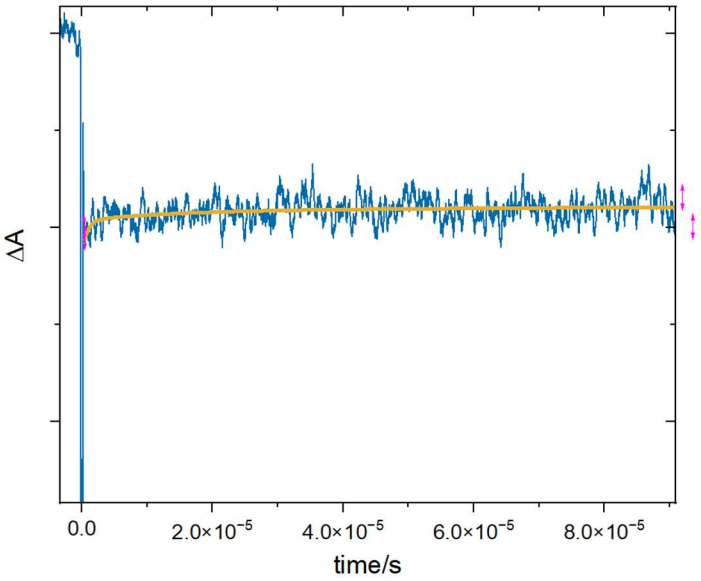

Figure D.33. Bleaching at 370 nm generated from HEH_2 (1.2 mM) in THF in the presence of [ColH]OTf (12 mM) and Col (50 mM). (Excitation wavelength: 355nm, detection wavelength: 370 nm).

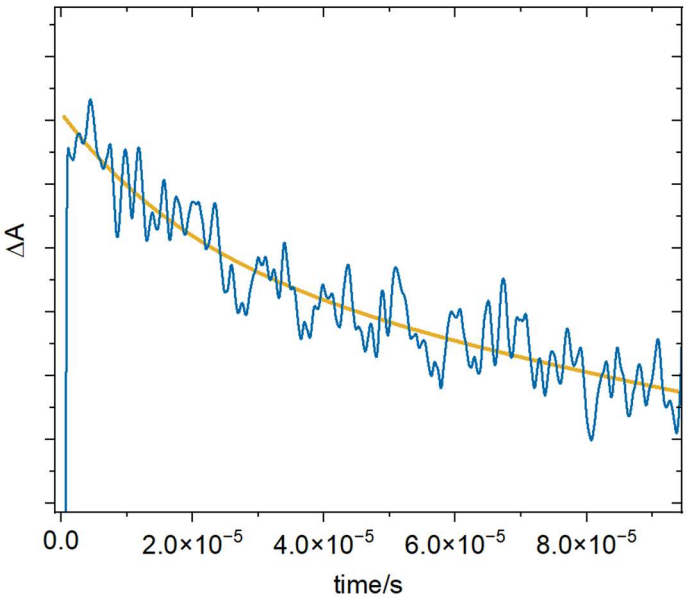

Figure D.34. Absorption at 500 nm generated from HEH_2 (1.2 mM) in THF in the presence of [ColH]OTf (12 mM). (Excitation wavelength: 355nm, detection wavelength: 500 nm).

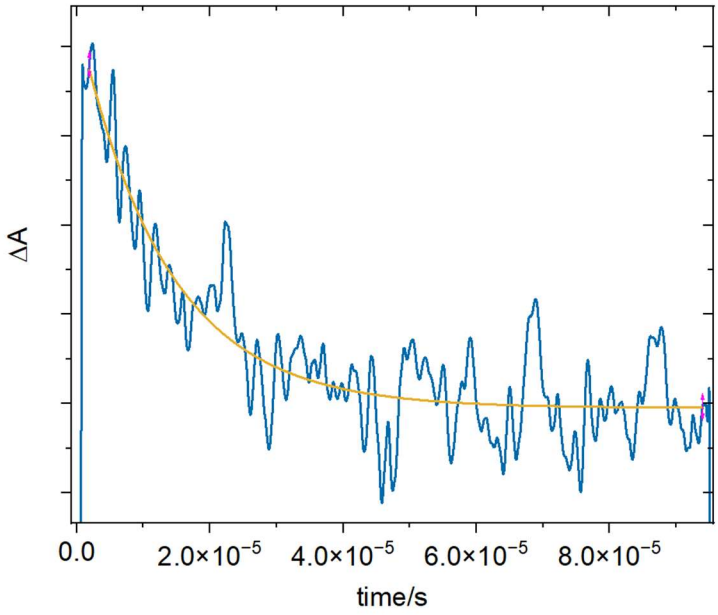

Figure D.35. Absorption at 500 nm generated from HEH_2 (1.2 mM) in THF in the presence of [ColH]OTf (12 mM) and Col (36 mM). (Excitation wavelength: 355nm, detection wavelength: 500 nm).

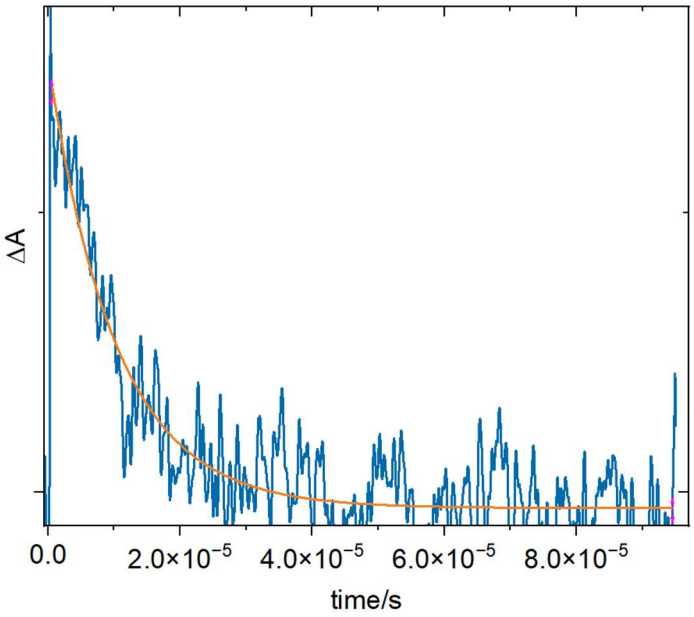

Figure D.36. Absorption at 500 nm generated from HEH_2 (1.2 mM) in THF in the presence of [ColH]OTf (12 mM) and Col (48 mM). (Excitation wavelength: 355nm, detection wavelength: 500 nm).

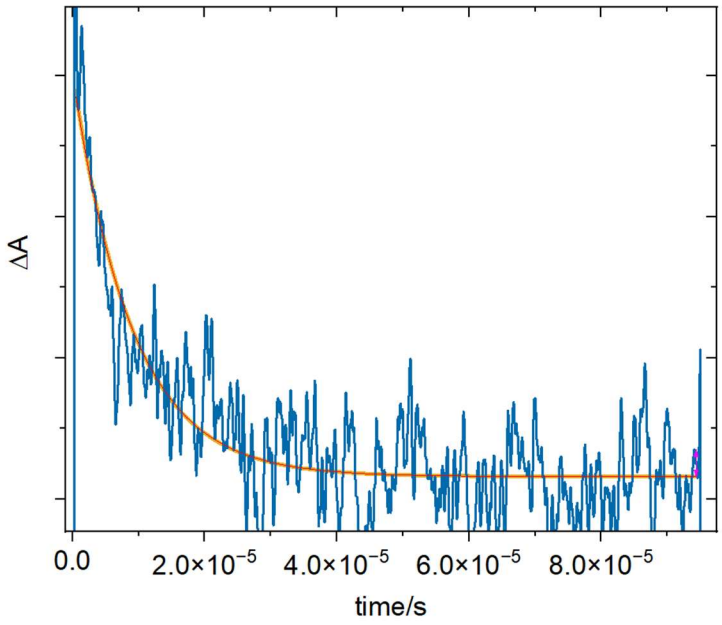

Figure D.37. Absorption at 500 nm generated from HEH_2 (1.2 mM) in THF in the presence of [ColH]OTf (12 mM) and Col (60 mM). (Excitation wavelength: 355nm, detection wavelength: 500 nm).

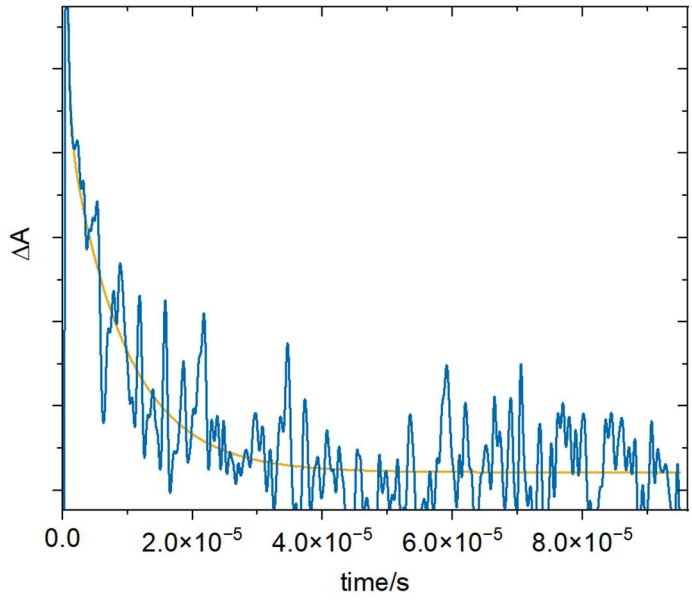

Figure D.38. Absorption at 500 nm generated from HEH_2 (1.2 mM) in THF in the presence of [ColH]OTf (12 mM) and Col (72 mM). (Excitation wavelength: 355nm, detection wavelength: 500 nm).

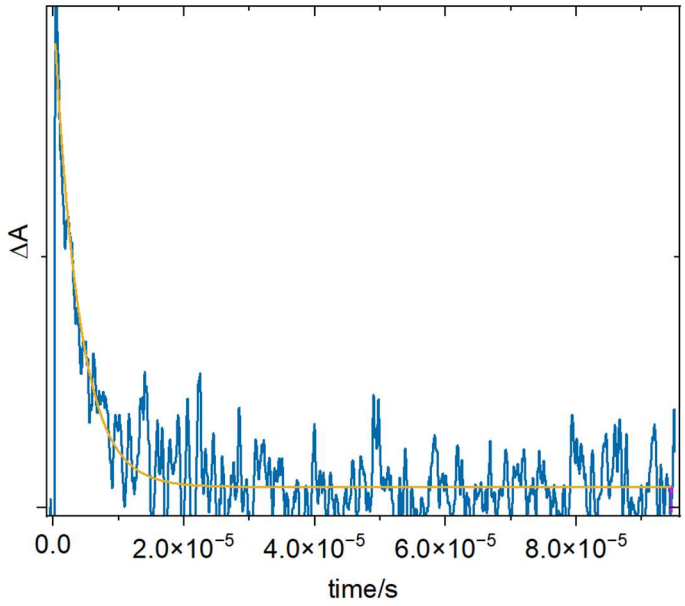

Figure D.39. Absorption at 500 nm generated from HEH_2 (1.2 mM) in THF in the presence of [ColH]OTf (12 mM) and Col (120 mM). (Excitation wavelength: 355nm, detection wavelength: 500 nm).

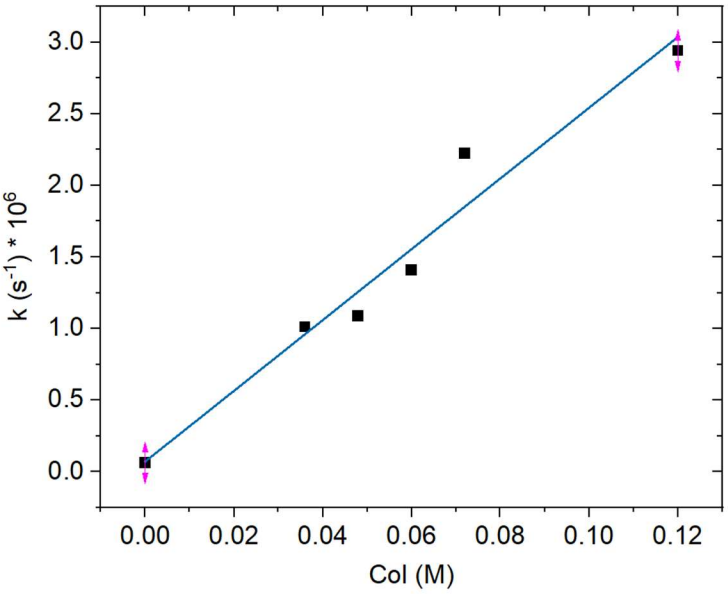

Figure D.40. Kinetic constants plot extrapolated from the lifetime of absorption signals generated after titrating HEH_2 (1.2mM) + [ColH]OTf (12 mM) with Col (36-120mM).

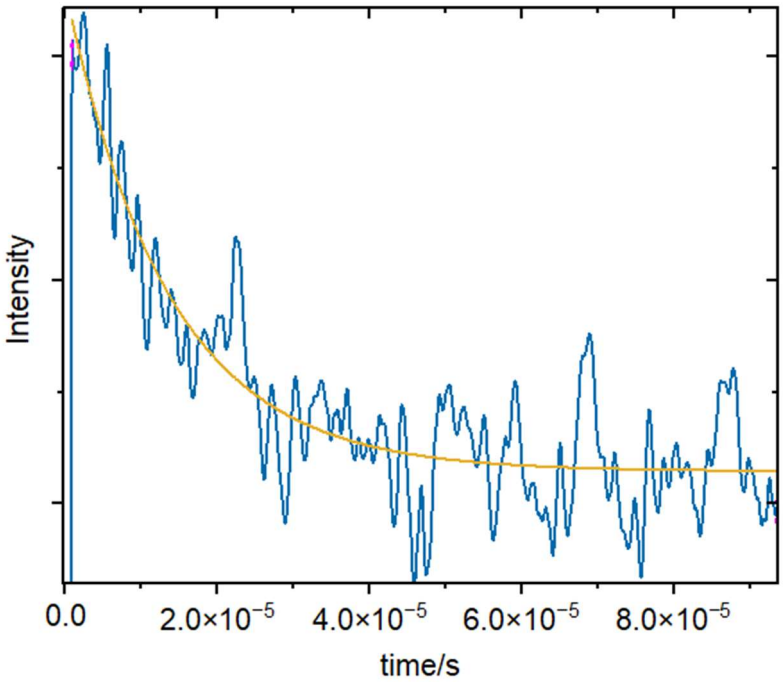

Figure D.41. Absorption at 500 nm generated from HEH_2 (1.2 mM) in THF in the presence of [ColH]OTf (60 mM). (Excitation wavelength: 355nm, detection wavelength: 500 nm).

Table D.21. Lifetime of absorption signals generated after titrating HEH_2 (1.2mM) + [ColH]OTf (12 mM) with Col (36-120mM).

	Lifetime (μs)
HEH_2 + [ColH]OTf	16 ± 5
HEH_2 + [ColH]OTf + Col (36 mM)	9 ± 2
HEH_2 + [ColH]OTf + Col (48 mM)	8 ± 1
HEH_2 + [ColH]OTf + Col (60 mM)	7.2 ± 0.5
HEH_2 + [ColH]OTf + Col (72 mM)	4.5 ± 0.5
HEH_2 + [ColH]OTf + Col (120 mM)	3.6 ± 0.5

Table D.22. Lifetime of absorption signals generated from HEH_2 (1.2mM) in the presence of [ColH]OTf (12-60 mM). The lifetime is not affected by the amount of [ColH]OTf added.

	Lifetime (μs)
HEH_2 + [ColH]OTf (12mM)	16 ± 5
HEH_2 + [ColH]OTf (36mM)	13 ± 3
HEH_2 + [ColH]OTf (48mM)	19 ± 5
HEH_2 + [ColH]OTf (60mM)	17 ± 3

D.8 EPR spectroscopy

D.8.1 General procedure for generation of freeze-quenched organic radicals

In a typical experiment, a J. Young-EPR tube was loaded with HEH_2 and Col-buffer (or other additives) in 100 mM concentration (unless otherwise noted) in THF. The tube was sealed and removed from the glovebox and irradiated in a highly reflective dewar. At the noted time (2 minutes, unless otherwise noted), the dewar was filled with liquid nitrogen to freeze the tube at 77 K. Irradiation was constant during the freezing of the tube. Subsequently, the EPR spectrum was measured in a 77 K immersion dewar using standard techniques.

For quantitative-EPR (Figure D.52), the spectra were collected at 0.002 mW power to avoid saturation of the signal. The double integral was compared to that of a 1 mM standard of TEMPO. The yield of the organic radical is in the presence of buffer ~ 10 μM. In the absence of buffer, the yield of the organic radical is lower (~5 μM).

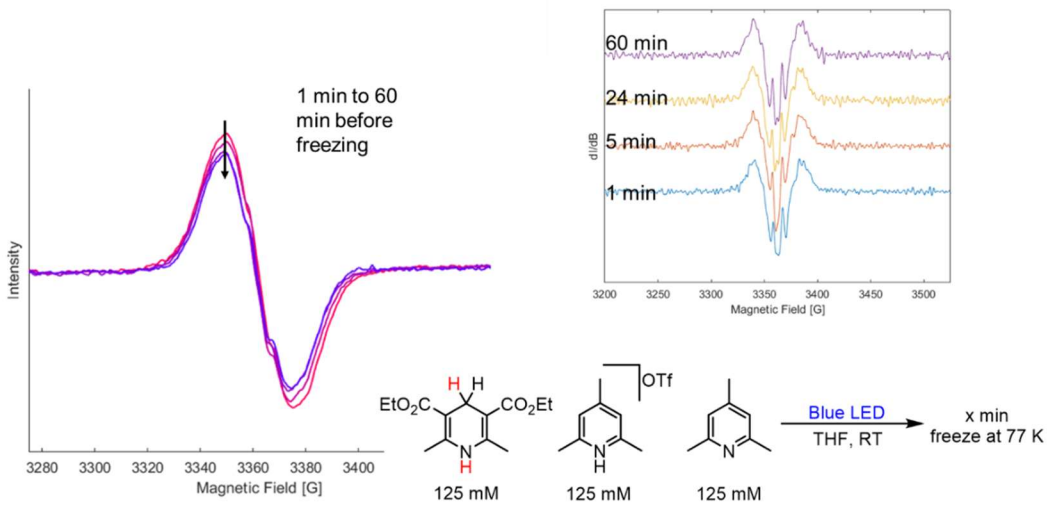

Figure D.42. CW-EPR data of HEH_2 with buffer varying reaction time before freeze-quenching. Acquisition parameters: temperature = 77 K; MW frequency = 9.38 GHz; MW power = 2 mW; modulation frequency = 100 kHz; modulation amplitude = 0.4 mT; conversion time = 20.5 ms.

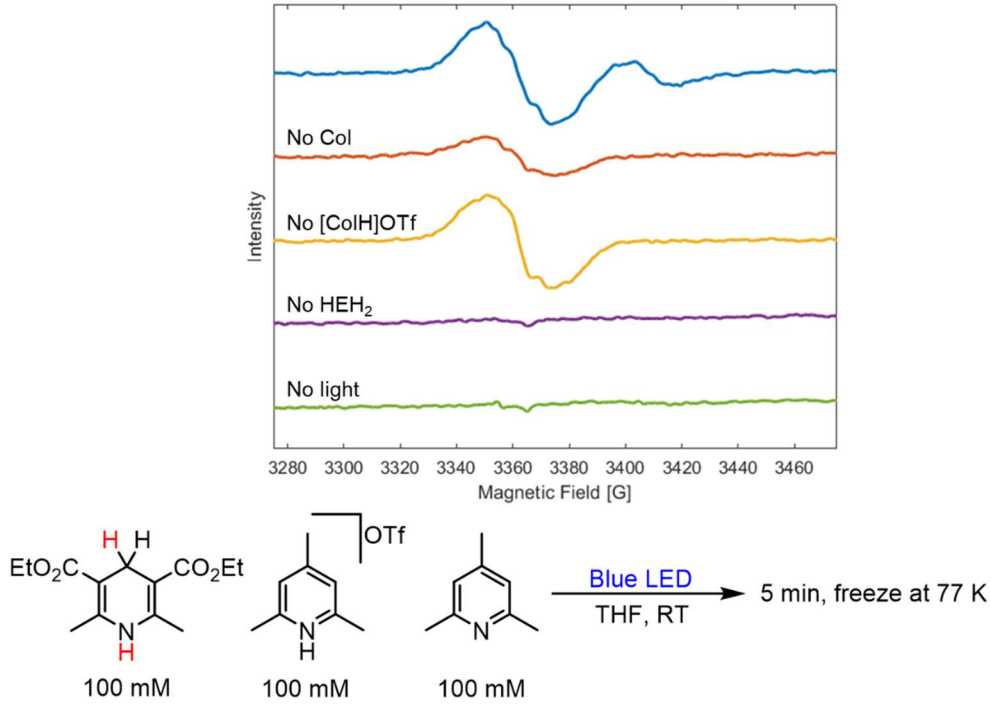

Figure D.43. CW-EPR data of HEH_2 with buffer and removing reaction components. Acquisition parameters: temperature = 77 K; MW frequency = 9.38 GHz; MW power = 2 mW; modulation frequency = 100 kHz; modulation amplitude = 0.4 mT; conversion time = 20.5 ms.

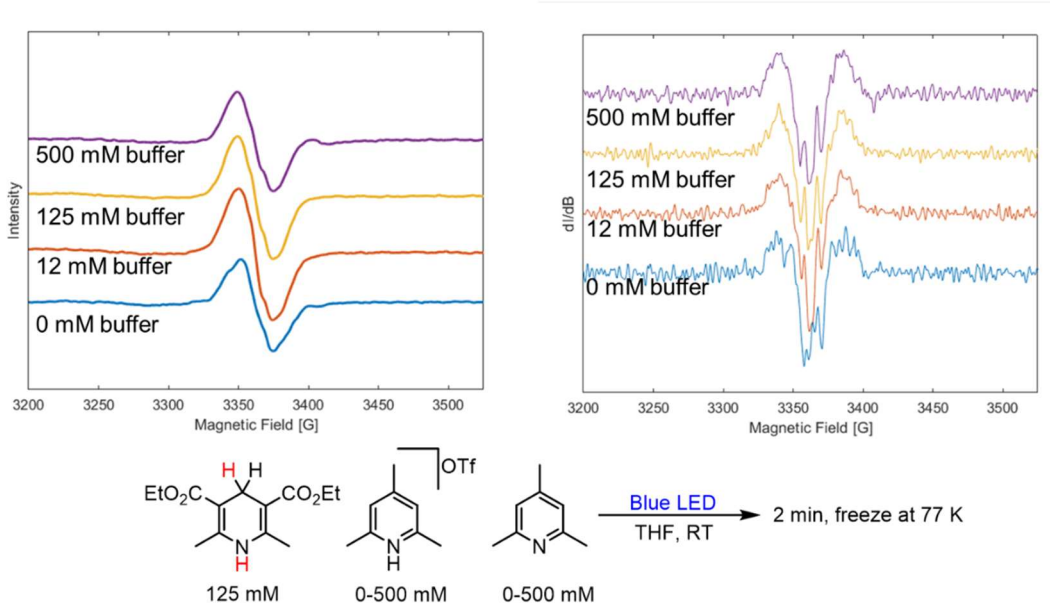

Figure D.44. CW-EPR data of HEH_2 with varying buffer loading. Acquisition parameters: temperature = 77 K; MW frequency = 9.38 GHz; MW power = 2 mW; modulation frequency = 100 kHz; modulation amplitude = 0.4 mT; conversion time = 20.5 ms.

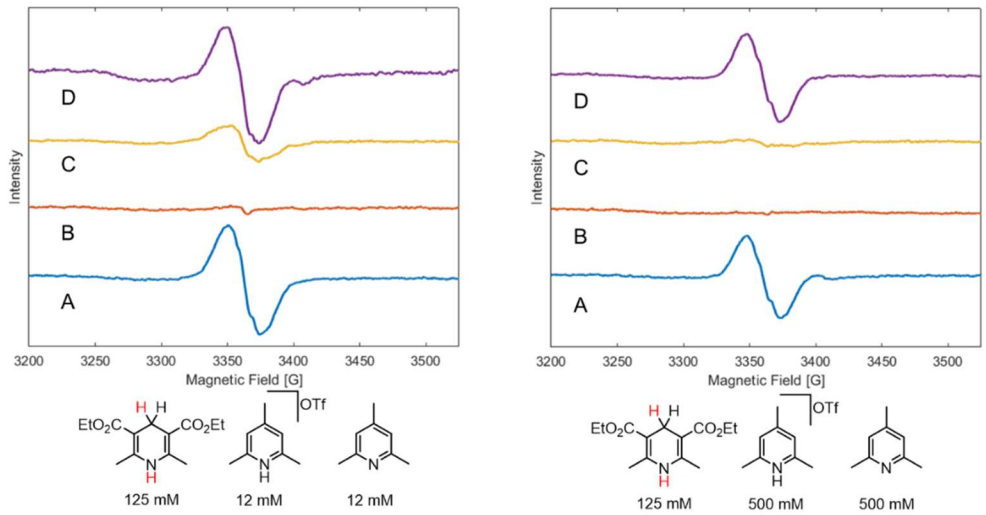

Figure D.45. CW-EPR data of HEH_2 with varying buffer loading. Spectra are labeled as follows: (A): Irradiate for 2 min, freeze at 77 K; (B): Thaw to RT, refreeze after 2 min without irradiation; (C): Irradiate while frozen; (D): Allow to thaw to RT, irradiate for 2 min, freeze at 77 K. Acquisition parameters: temperature = 77 K; MW frequency = 9.38 GHz; MW power = 2 mW; modulation frequency = 100 kHz; modulation amplitude = 0.4 mT; conversion time = 20.5 ms.

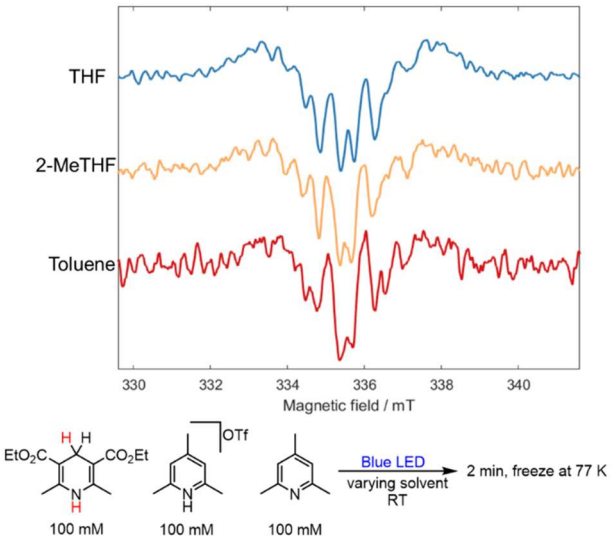

Figure D.46. CW-EPR spectra of freeze quenched reaction of HEH_2 with 100 mM Col-buffer irradiated for 2 minutes before freezing. The solvent is varied between experiments. Acquisition parameters: temperature = 77 K; MW frequency = 9.38 GHz; MW power = 2 mW; modulation frequency = 100 kHz; modulation amplitude = 0.1 mT; conversion time = 20.5 ms.

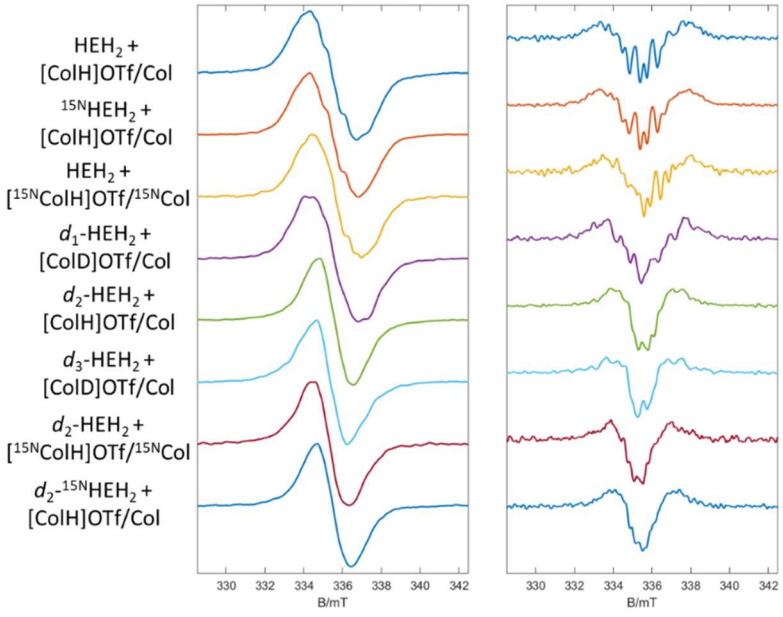

Figure D.47. CW-EPR spectra and 2nd derivative (hyperfine) spectra of reaction of HEH_2 and [ColH]OTf/Col with varying isotopologues. All reactions were conducted with 100 mM of reagents in THF, irradiating for 2 minutes before freeze-quenching. Assignment is

detailed in main text. Acquisition parameters: temperature = 77 K; MW frequency = 9.38 GHz; MW power = 2 mW; modulation frequency = 100 kHz; modulation amplitude = 0.1 mT; conversion time = 20.5 ms.

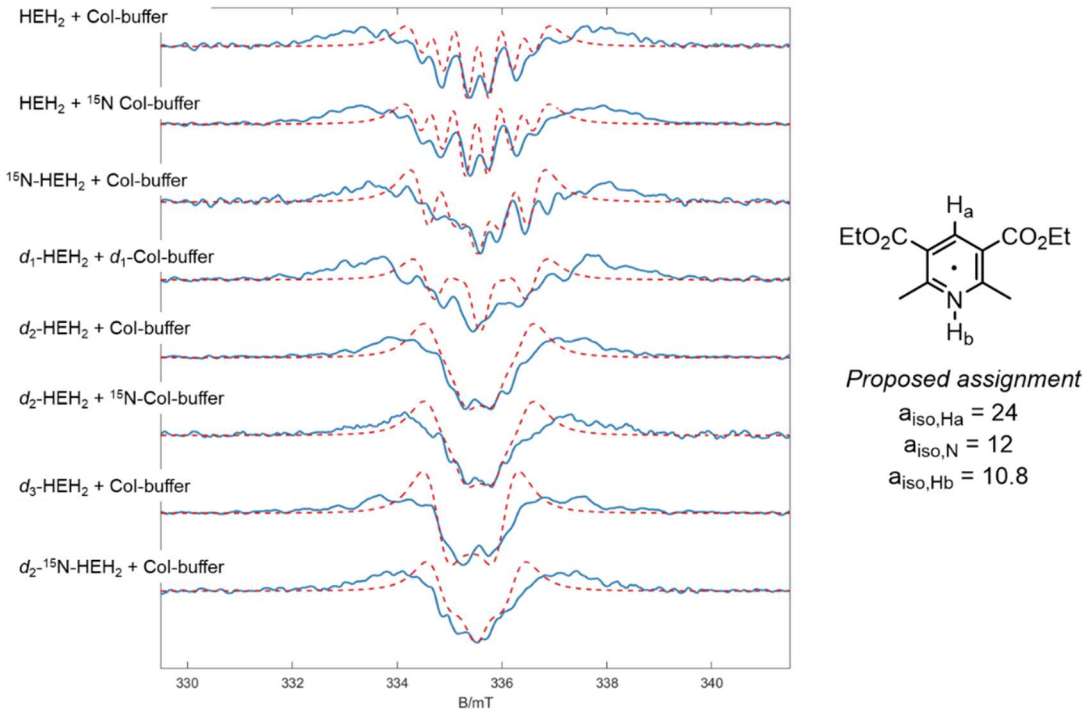

Figure D.48. 2nd derivative (hyperfine) spectra of HEH_2 with 100 mM Col-buffer, irradiated (Blue LED) and freeze-quenched after 2 minutes. Isotopologues of HEH_2 and Col-buffer are used. The lower quality fits for d_1-HEH_2/d_1-Col buffer, and d3-HEH2/d3-Col buffer is attributed to a lower degree of deuteration (compared to d_2-HEH_2) and partial exchange with trace water from HEH_2. Acquisition parameters: temperature = 77 K; MW frequency = 9.38 GHz; MW power = 2 mW; modulation frequency = 100 kHz; modulation amplitude = 0.1 mT; conversion time = 20.5 ms.

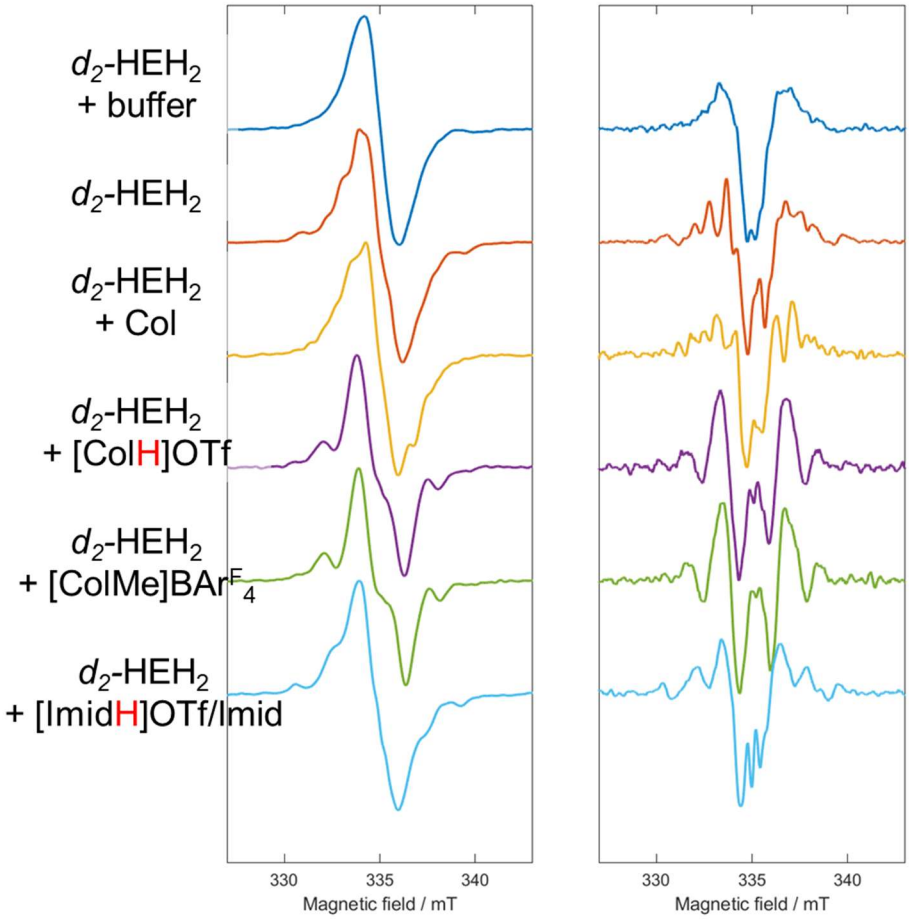

Figure D.49.. The differences between different reagent combinations are best visualized in the CW and 2nd derivate spectra of d_2-HEH$_2$ and various additives. CW-EPR spectra and 2nd derivative (hyperfine) spectra of d_2-HEH$_2$ with 100 mM buffers/additives are shown. No buffer, Col, and Imid-buffer all look similar. [ColH]OTf and [ColMe]BAr$^F_4$ also look different from HEH$_2$ and Col-buffer. We note that the difference between HEH$_2$ + Col-buffer and HEH$_2$ + [ColH]OTf is much clearer with d_2-HEH$_2$. Acquisition parameters: temperature = 77 K; MW frequency = 9.38 GHz; MW power = 2 mW; modulation frequency = 100 kHz; modulation amplitude = 0.1 mT; conversion time = 20.5 ms.

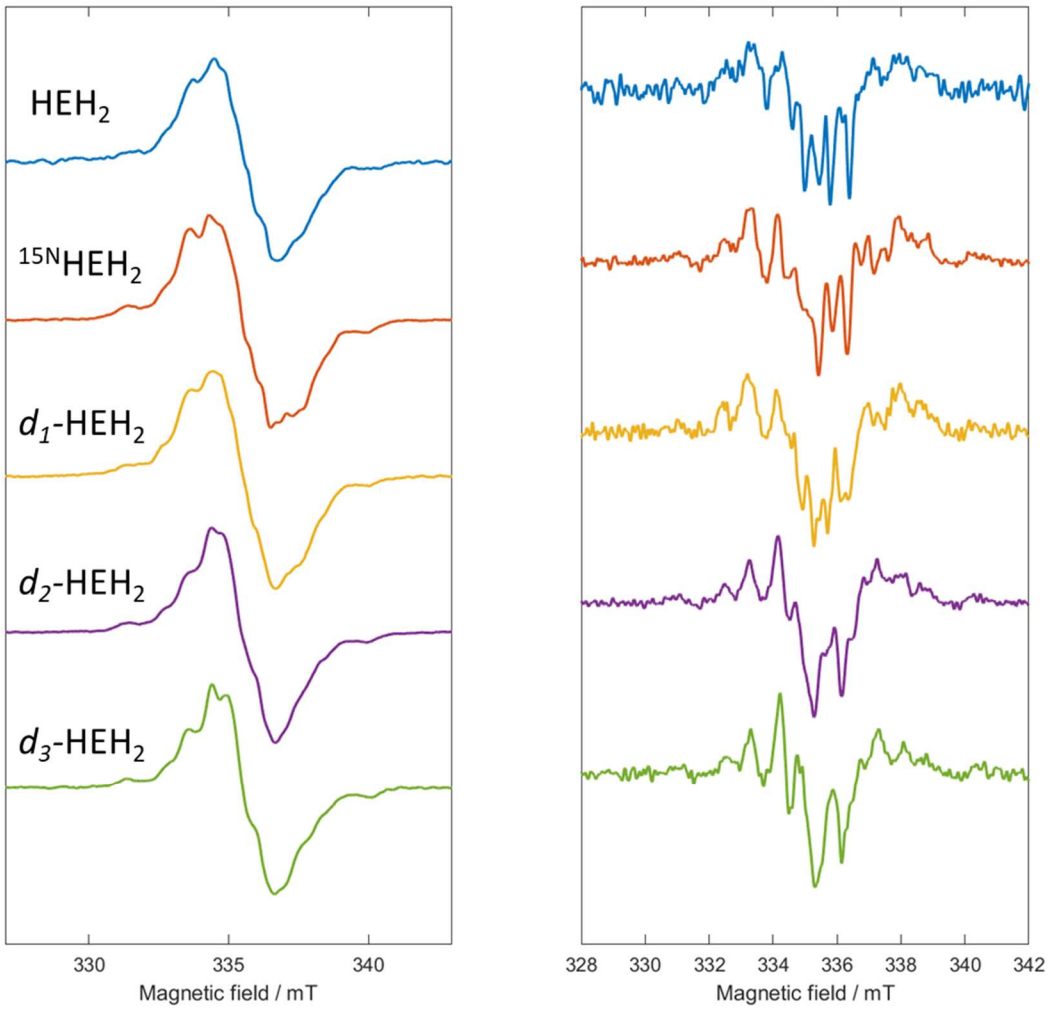

Figure D.50. CW-EPR spectra and 2nd derivative (hyperfine) spectra of HEH_2 isotopologues (100 mM) in THF, 2 minutes irradiation before freeze-quenching. Attempts to assign these spectra were challenged by the low intensity of the signal. Acquisition parameters: temperature = 77 K; MW frequency = 9.38 GHz; MW power = 2 mW; modulation frequency = 100 kHz; modulation amplitude = 0.1 mT; conversion time = 20.5 ms.

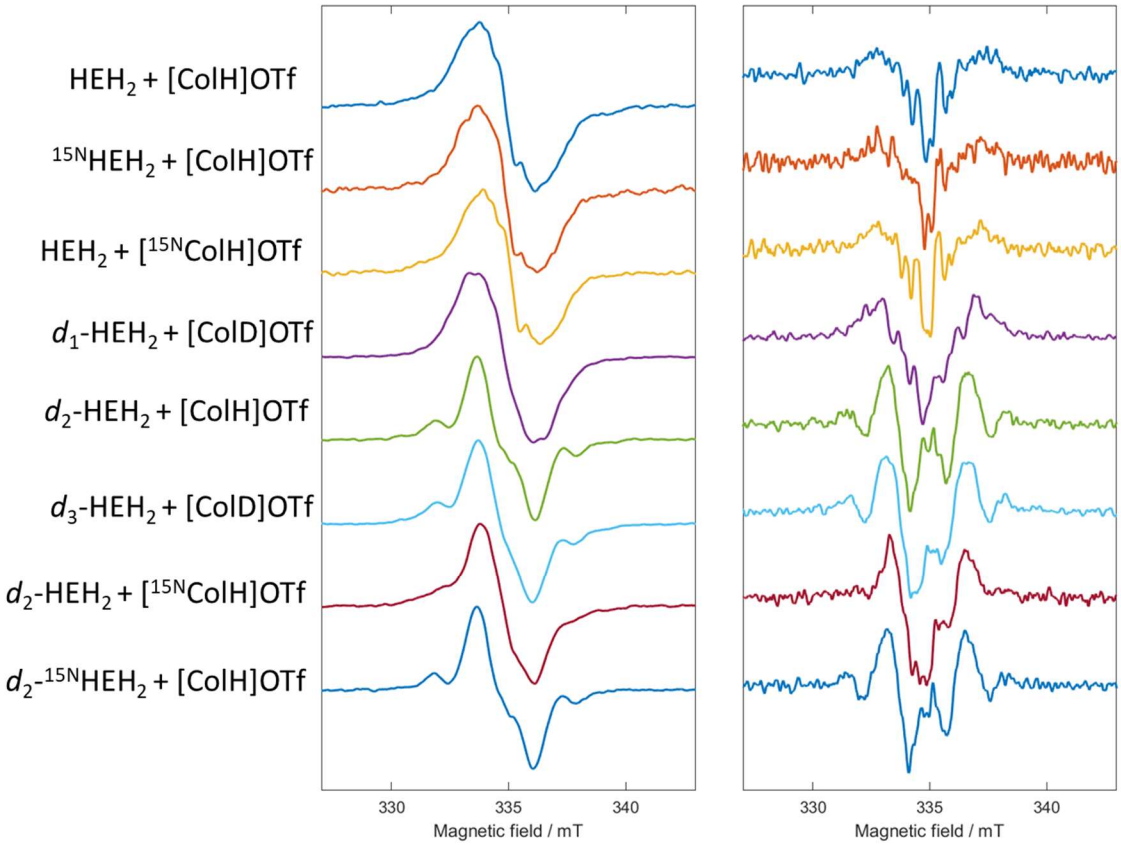

Figure D.51. CW-EPR spectra and 2nd derivative (hyperfine) spectra of reaction of HEH_2 and [ColH]OTf with varying isotopologues. All reactions were conducted with 100 mM of reagents in THF, irradiating for 2 minutes before freeze-quenching. Attempts to assign these spectra were challenged by the low intensity of the signal. Dependance on ^{15N}-Col and ^{15N}-HEH_2 labelling suggest that multiple species are associated with this signal. Acquisition parameters: temperature = 77 K; MW frequency = 9.38 GHz; MW power = 2 mW; modulation frequency = 100 kHz; modulation amplitude = 0.1 mT; conversion time = 20.5 ms.

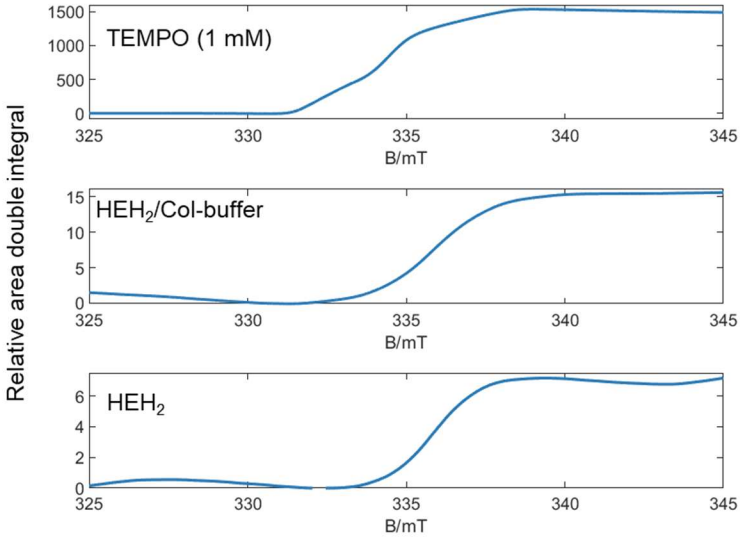

Figure D.52. Double integral of CW-EPR spectra of organic radical generated at low power (0.002 mW).

D.9 Electrochemical measurements

D.9.1 General procedure

Electrochemical measurements were conducted with a glassy carbon working electrode, a platinum wire counter electrode, and Ag/AgOTf (1mM AgOTf in 0.2 M [TBA][PF_6]) reference electrode isolated by a CoralPor™ frit (obtained from BASi) and referenced externally to $Fc^{+/0}$. Unless otherwise specified, NaK dried THF was used as solvent, with 0.2 M [TBA]PF_6 electrolyte. Measurements were conducted with a CH Instruments 600B electrochemical analyzer. For irreversible chemical events, oxidation of HEH_2 and reduction of [ColMe]$BAr^F{}_4$ were estimated using the inflection point potential to estimate $E_{1/2}$.[15]

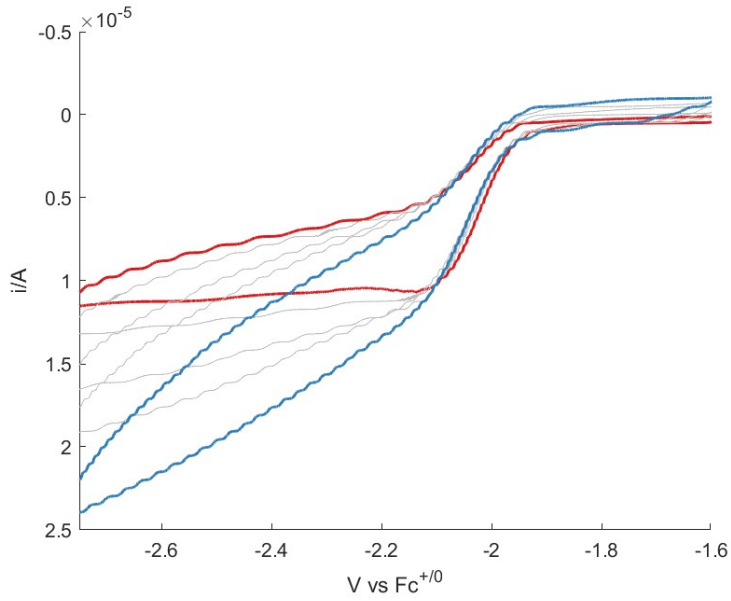

Figure D.53. Cyclic voltammograms of [ColMe]BAr^F_4 (2 mM, dashed lines) in 0.2 M [TBA]PF_6 in THF, with increasing scan rate from 25 mV s^{-1} (red trace) to 400 mV s^{-1} (blue trace).

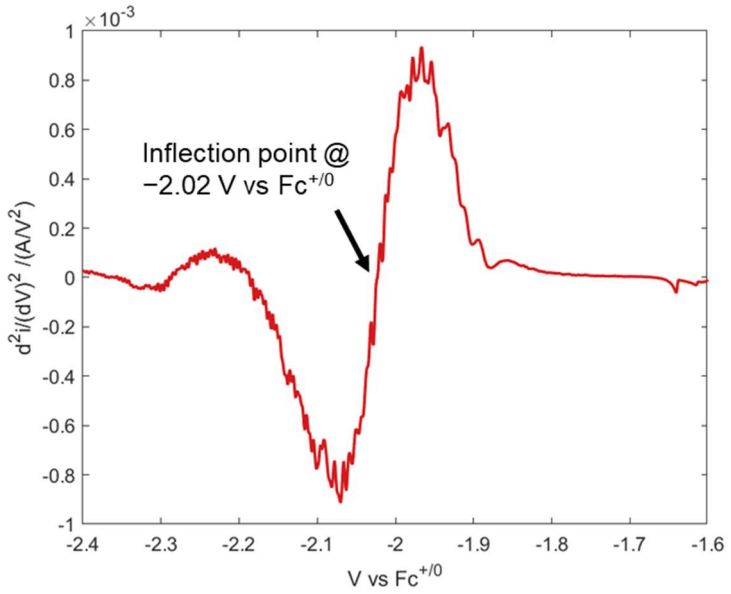

Figure D.54. 2nd derivative of linear sweep of [ColMe]BAr^F_4 (2 mM, dashed lines) in 0.2 M [TBA]PF_6 in THF, at 25 mV s^{-1} to determine inflection point (−2.02 V vs $Fc^{+/0}$).

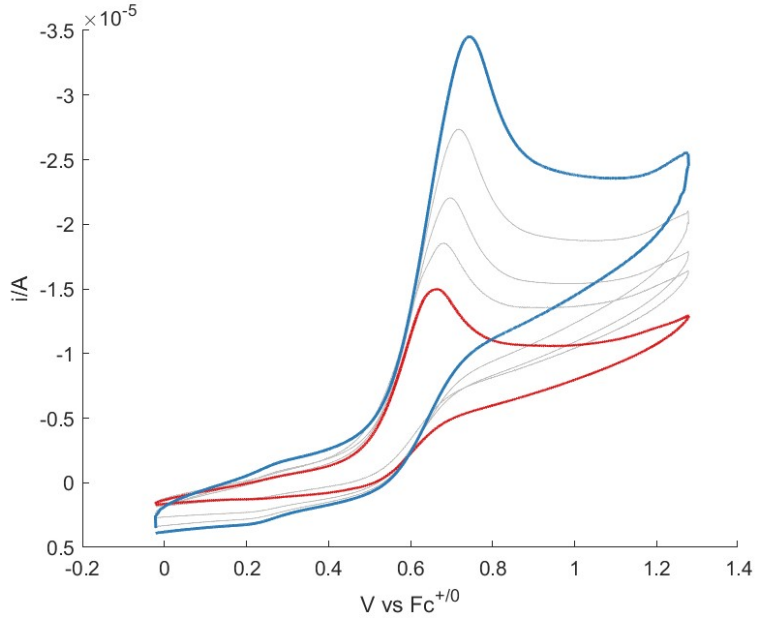

Figure D.55. Cyclic voltammograms of HEH_2 (2 mM, dashed lines) in 0.2 M $[TBA]PF_6$ in THF, with increasing scan rate from 25 mV s^{-1} (red trace) to 400 mV s^{-1} (blue trace).

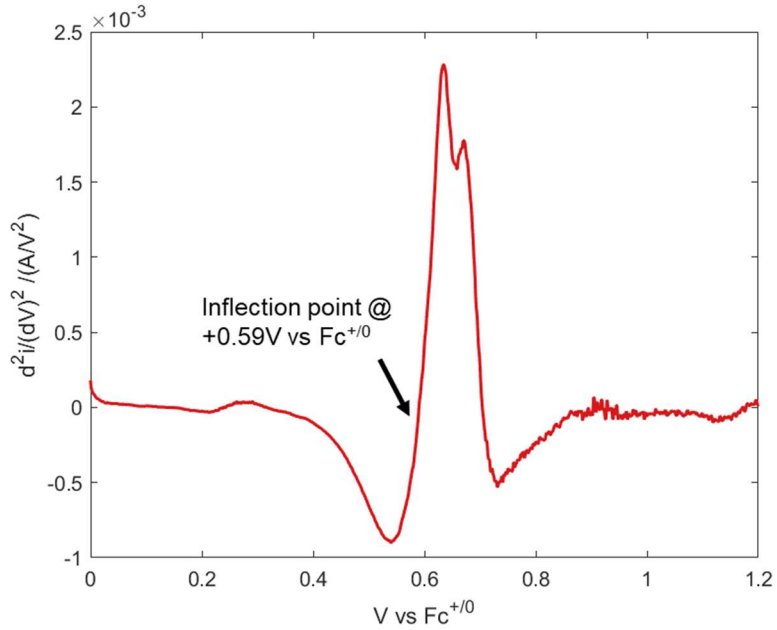

Figure D.56. 2nd derivative of linear sweep of HEH_2 (2 mM, dashed lines) in 0.2 M $[TBA]PF_6$ in THF, at 25 mV s^{-1} to determine inflection point (0.59 V vs $Fc^{+/0}$).

D.10 Infrared spectroscopy

D.10.1 General considerations

All IR data were collected as solution state spectra in a KBr-cell in THF. All data, unless stated, have had THF background spectra subtracted. This results in the regions 636-1500 and 2657-3050 cm^{-1} being completely blocked out due to the intensity of the much more intense THF peaks. Nonetheless, key IR transitions, specifically carbonyl and C=C double bonds, land largely outside this region, providing valuable probes for interactions between HEH_2 and [ColH]OTf.

In some cases, specifically, when acids are used, issues with subtractions result in artifacts in the region 2050-2550 cm-1 (Figures D.59, D.63, and D.64). These artifacts align exactly with THF overtones in the background spectra. We also note a much greater intensity of HEH_2 N−H over $ColH^+$ N−H (see Figures D.65-D.66). This limited the possibility of observing H-bonding between $[ColH]^+$ and HEH_2 as these signals are covered by the HEH_2 N−H stretch.

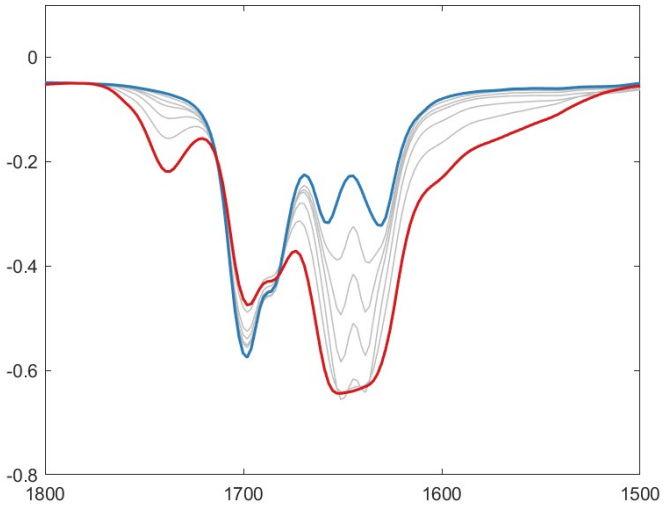

Figure D.57. Infrared spectra of 10 mM solution of HEH_2. [ColH]OTf was titrated in from 0 to 80 mM acid. Upon titration of acid the HEH_2 carbonyl stretch at 1695 cm^{-1} decreases, while a new peak at 1730 cm^{-1} grows in.

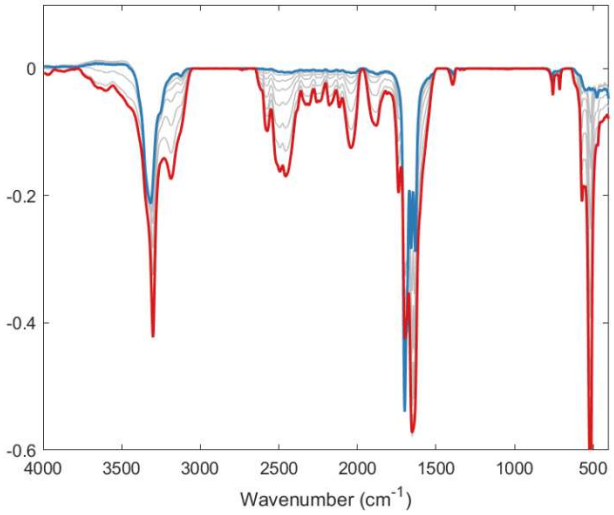

Figure D.58. Infrared spectra of 10 mM solution of HEH_2 (Blue). [ColH]OTf was titrated in from 0 to 80 mM acid (red trace 80 mM). Upon titration of acid the HEH_2 carbonyl stretch at 1695 cm^{-1} decreases, while a new peak at 1730 cm^{-1} grows in. In addition, peaks assignable to [ColH]+ grow in, including C-C π-stretches at 1650, 1638 cm-1, and N−H stretch at 3300 cm^{-1}.

Peaks from 1900-2650 align exactly with THF overtones that have their linewidths (but not peak position) affected by the titration of [ColH]OTf. This results in a poor THF subtraction in this region. See Figure D.63 for details).

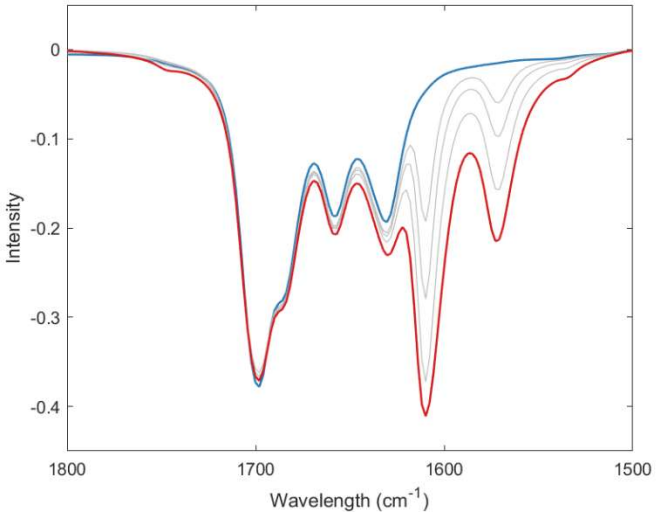

Figure D.59. Infrared spectra of 10 mM solution of HEH_2 (blue). Col was titrated in from 0 to 80 mM base (red trace 80 mM). The peak intensity of the HEH_2 carbonyl stretches at 1700, 1685 cm^{-1} remain unchanged.

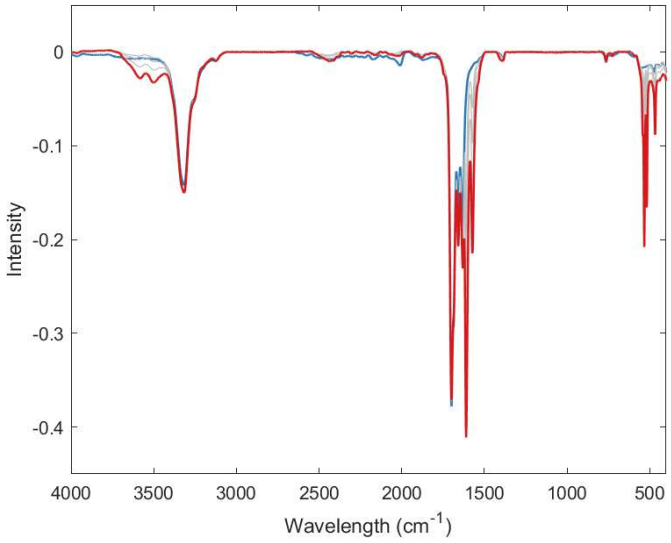

Figure D.60. Infrared spectra of 10 mM solution of HEH_2 (blue). Col was titrated in from 0 to 80 mM base (red trace 80 mM).

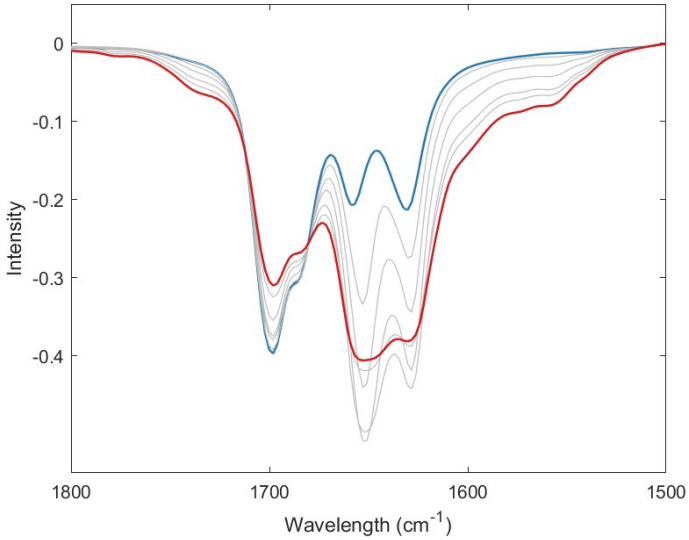

Figure D.61. Infrared spectra of 10 mM solution of HEH_2. [LutH]OTf was titrated. Upon titration of acid, the HEH2 carbonyl stretch at 1695 cm-1 decreases, while a new peak at 1730 cm-1 grows, similar to what is observed with [ColH]OTf. Despite being slightly more acidic than $[ColH]^+$, the magnitude of the decrease of the HEH_2 carbonyl stretches are similar between $[LutH]^+$ and $[ColH]^+$.

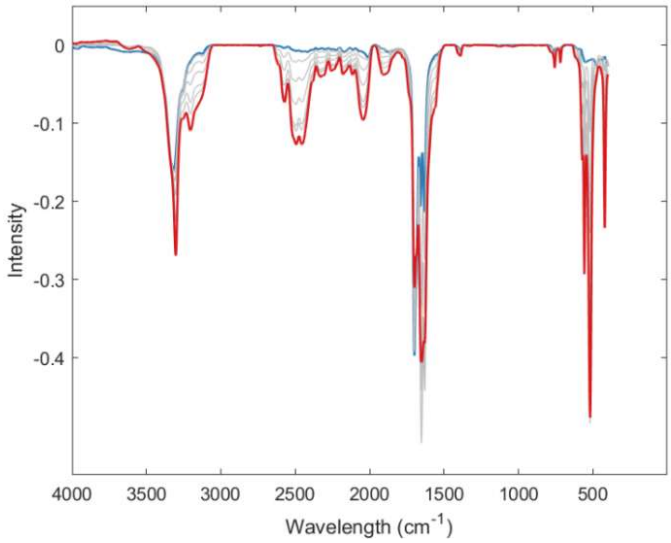

Figure D.62. Infrared spectra of 10 mM solution of HEH_2 (Blue). [LutH]OTf was titrated in from 0 to 80 mM acid (red trace 80 mM). Upon titration of acid the HEH_2 carbonyl stretch at 1695 cm^{-1} decreases, while a new peak at 1730 cm^{-1} grows in. In addition, peaks assignable to [LutH]+ grow in, including C-C π-stretches at 1650, 1638 cm-1, and N−H stretch at 3300 cm^{-1}.

Peaks from 1900-2650 align exactly with THF overtones that have their intensity and linewidths but not peak position affected. This results in a poor THF subtraction in this region. This effect appears to be the same as for $[ColH]^+$.

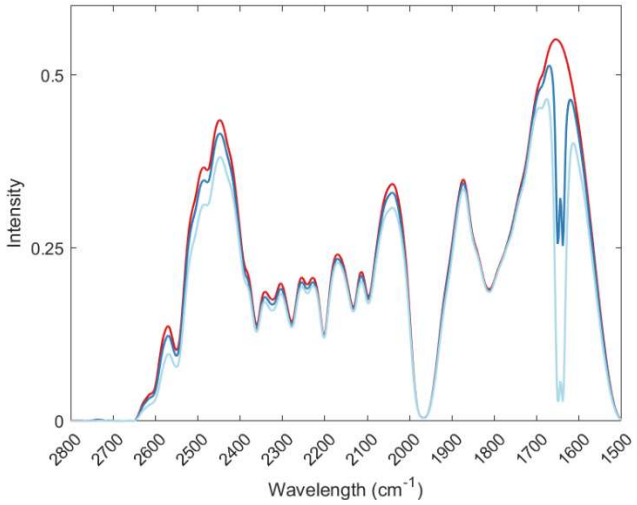

Figure D.63. Unsubtracted transmission infrared spectra of THF (red trace), 10 mM solution of [ColH]OTf in THF (Blue), and 40 mM [ColH]OTf (light blue). We wish to draw attention to the poor alignment between certain THF transmission overtones, specifically the peaks at 2550, 2480, 2330, and 2220 cm^{-1} and transmission minima at 2450, 2100, and 2050 cm^{-1}. While the origin of this poor alignment is unclear, we note that there

are not shifts in the position of these peaks, consistent with these new peaks not corresponding to [ColH]OTf vibrational modes.

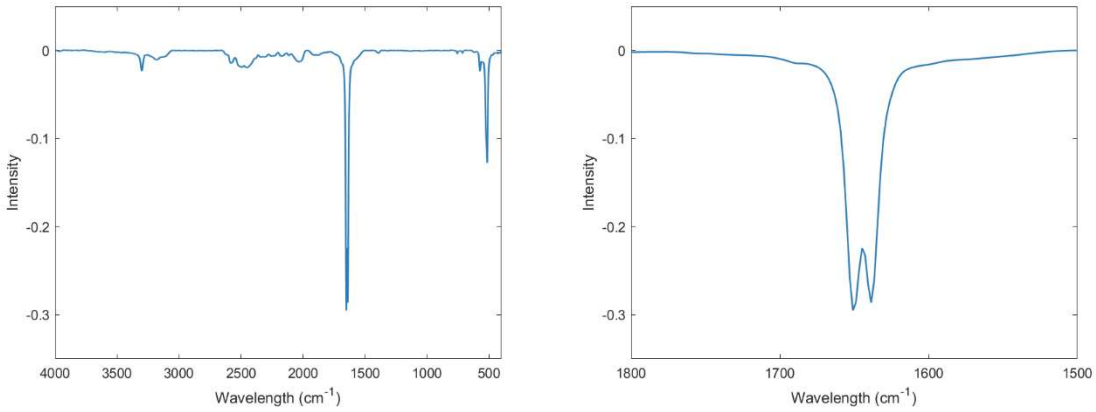

Figure D.64. [ColH]OTf (10 mM) in THF, both wide and zoomed in on the double bond region, with C-C π-stretches at 1650, 1638 cm-1, and N−H stretch at 3300 cm-1, and C−H stretches at 3180 and 3116 cm^{-1} observed.

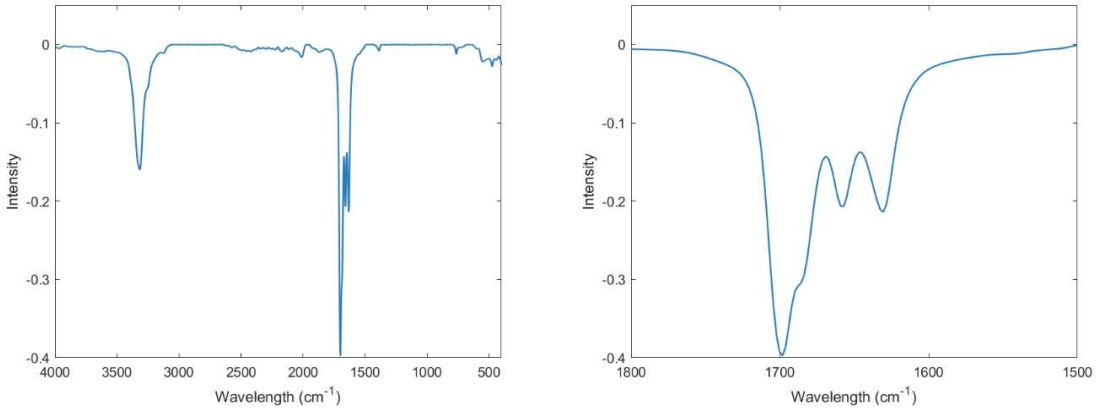

Figure D.65. HEH_2 (10 mM) in THF, both wide and zoomed in on double bond region, including C-C π-stretches at 1660, 1630 cm^{-1}, C=O bonds 1685, 1700 cm^{-1} and N−H stretch at 3310 cm^{-1} observed.

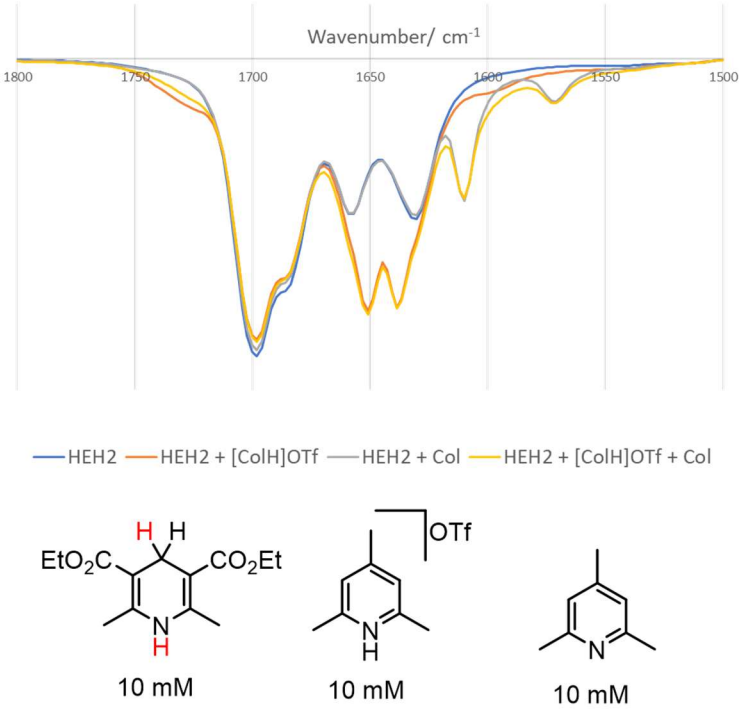

Figure D.66. Infrared spectra of 10 mM solution of HEH_2 (blue trace), 10 mM solution of HEH_2 + [ColH]OTf (10 mM each, orange trace), HEH_2 + Col (10 mM each, grey trace), and HEH_2 + [ColH]OTf/Col (10 mM each, yellow trace). Shoulder at 1730 cm^{-1} appears upon the addition of acid or in the buffer mixture.

D.11 Measurement of HEH_2 excited state pK_a

D.11.1 General considerations

The excited state pK_a of HEH_2 was calculated in MeCN to allow a good comparison with the existing pK_a of $[ColH]^+$ in organic solvent.[12] The resulting values were confirmed to hold in THF by steady-state fluorimetry (Figure D.70).

The excited state pK_a in MeCN was measured using the Förster equation:

$$pK_a^* = pK_a + E_{00,EH2-} - E_{00,HEH2} \quad \text{(eqn D.4)}[14]$$

using these values as derived from Figures D.71-D.72. We calculate pK_a* (HEH_2) 23.8±0.6. This is notable ΔpK_a 8 from that of Col, the buffer during N_2R. Accordingly, the excited state deprotonation of HEH_2 should not play a role during catalysis.

UV-vis and fluorescence experiments were conducted as previously detailed.

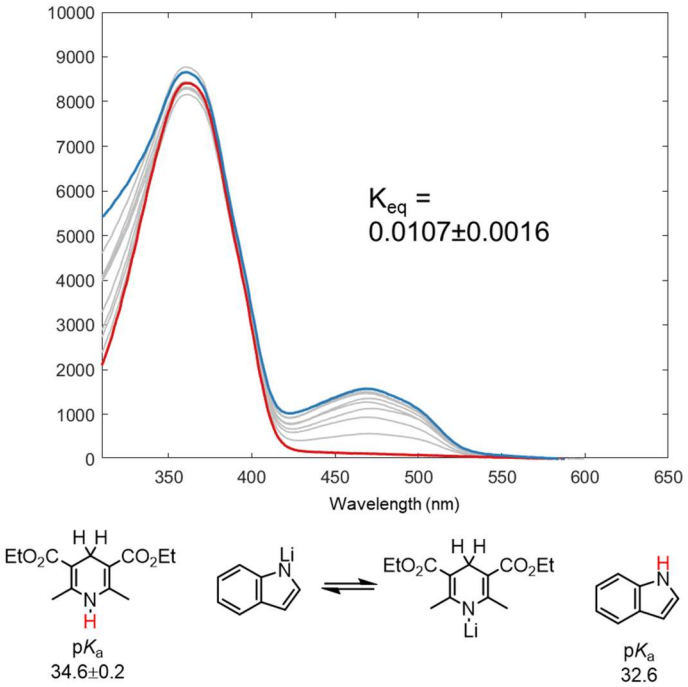

Figure D.67. Measure of pK_a of HEH_2 in MeCN via titration of sodium indolate (pK_a 32.6 in MeCN)[12], used to derive pK_a of HEH_2 at 34.6.

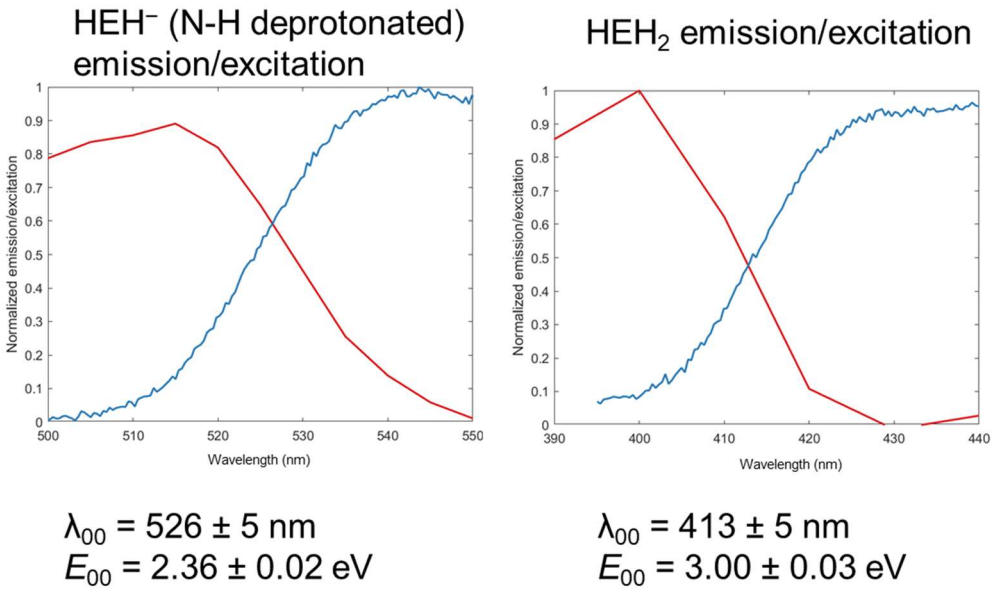

Figure D.68. Measure of E_{00} of Na[HEH_C] (0.5 mM) and HEH_2 (0.5 mM) in MeCN.

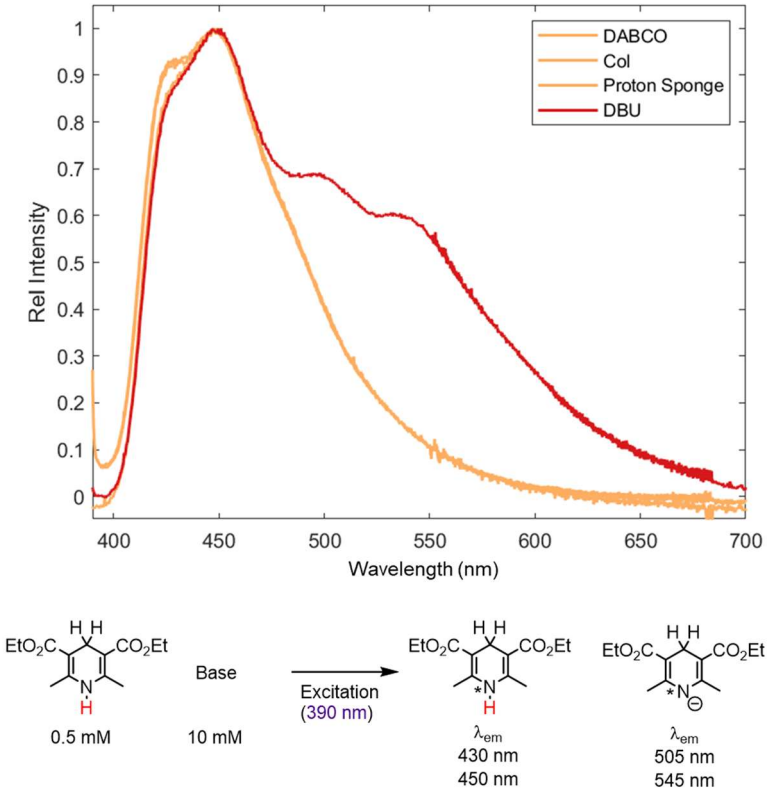

Figure D.69. Measure of pK_a of HEH_2 in THF via the addition of increasingly strong bases. Only when DBU is added is excited state deprotonation of HEH_2 observed. Weaker bases (Col, DABCO, proton sponge) do not deprotonate $^*HEH_2$.

D.12 Summary of thermochemistry of Hantzsch ester (HEH_2) and derivatives and [ColH]$^\bullet$

D.12.1 General considerations

Table D.22 lists $BDFE_{X–H}$, pK_a, and E_{ox} values for various protonation and oxidation states of HEH_2. As has been established by Mayer and coworkers,[16] bond dissociation enthalpies (BDEs) can be converted to BDFEs based on the assumption that the entropies of R–H and R$^\bullet$ are similar. Subtraction of $TS°(H^\bullet)_{solv}$ (6.37 kcal mol^{-1} in MeCN) from the BDE values reported in ref. 17 yields the estimated BDFE values in Table D.22.

$$\mathrm{BDFE}_{\mathrm{estimated}} = 23.06\,E + 1.37\,\mathrm{p}K_a + C_{\mathrm{G}} \quad (\text{eqn } A5.5)$$

Given the proposed role of ColH$^{\bullet}$ radicals, it is useful to experimentally estimate the $BDFE_{N-H}$ using the Bordwell equation.[18] This can be compared to relevant BDFEs of HEH_2 and its semi-oxidized intermediates for which bond strengths have previously been thermochemically derived.[17] The pK_a of $[ColH]^+$ has been measured in MeCN and THF as 15.0 and 10.4, respectively.[12,19] As it is difficult to accurately measure $E(ColH^{+/0})$[20] due to the earlier onset of proton reduction, we rely on $E(ColMe^{+/0})$ as a substitute, measuring $E(ColMe^{+/0})$ as −1.90 V and −2.02 V vs $Fc^{+/0}$ in MeCN[21] and THF. Using eqn D.5 and C_G of 52.6 and 59.9 kcal mol^{-1} in MeCN and THF, we calculate $BDFE_{estimated}$ as 29 kcal mol^{-1} (MeCN) and 28 kcal mol^{-1} (THF), respectively.

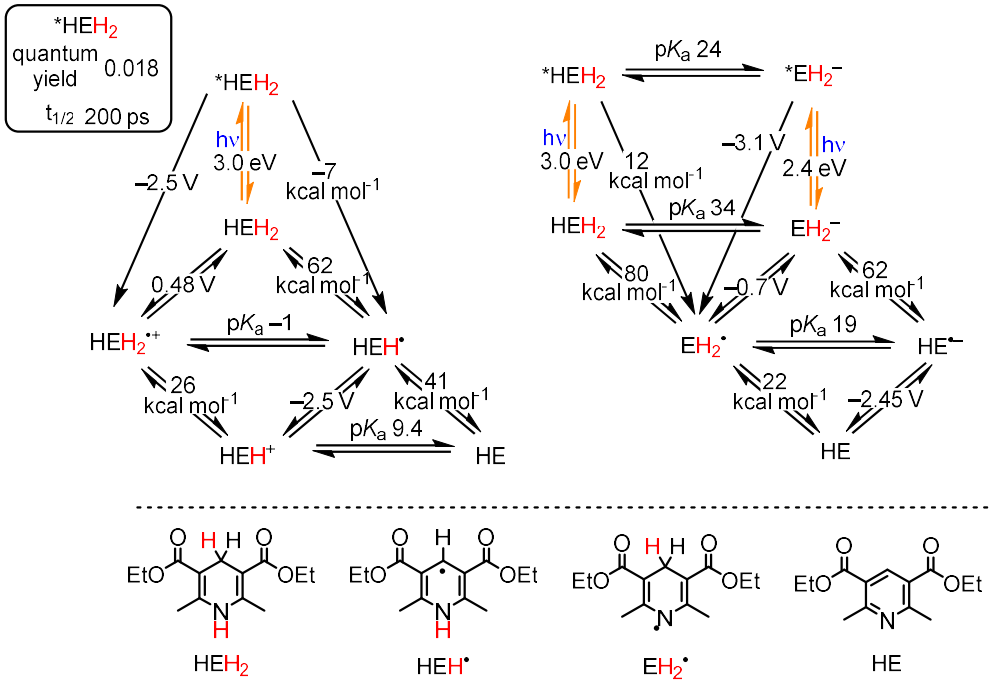

Figure D.70. Overview of measured thermochemistry (in MeCN) of HEH_2 based on either initial C−H or N−H bond oxidation, with excitation (3.0 eV) added to show changes in driving force from excited state.

Table D.22. Reported and estimated thermochemical values for various protonation and oxidation states of HEH_2 relevant to this study. [a] kcal mol^{-1} in MeCN at 298 K. [b] V vs. $Fc^{+/0}$ in MeCN at 298 K. [c] Ref. 18.
[d] Measured in this report, in THF vs $Fc^{+/0}$, see Figures D.54-D.55. [e]Measured in this (in MeCN) report see Section S10. [f]E_{00} measured in this report see Figure D.69, using Rehm-Weller approximation.[22] [g] Ref. 12 [h] Ref. 19 [i]Estimated from $[ColMe]^{+/0}$, measured previously by Pragst and coworkers, Ref 21. [j]Estimated from $[ColMe]^{+/0}$, measured in this report see Figures D.52-D.53.

	BDE[a]	BDFE[a]	E_{ox}[b]	pK_a
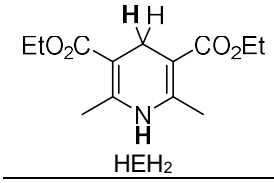 HEH_2	68.7 (C–H), 86.6 (N–H)[c]	62.3 (C–H), 80.2 (N–H)	0.48[c] 0.59[d]	31.8 (N–H) 34.6 (N–H)[e]
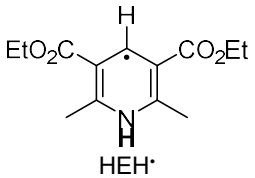 $HEH^{\bullet}$	46.9 (N–H)[c]	40.5 (N–H)		
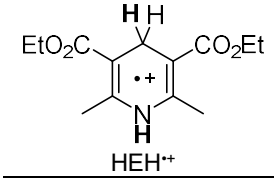 $HEH^{\bullet+}$				–1.0 (C–H)
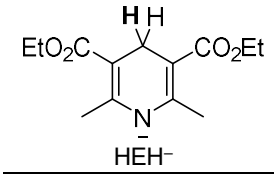 HEH^{-}			–0.695[c]	
$[HEH_2]^*$		–8.5 (C–H)	–2.5[f] –2.4[f]	23.8 (N–H)
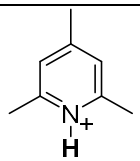				15.0 (N–H)[g] 10.4 (N–H)[h]
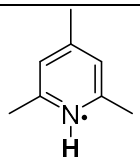		29.4 (N–H) 27.6 (N–H)	−1.90[i] −2.02[j]	

D.13 Additional mechanistic schemes

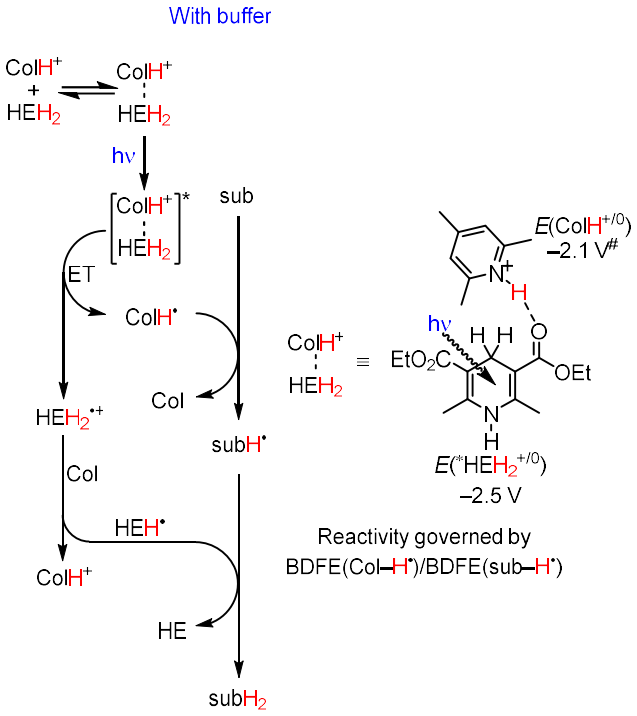

Figure D.71. Proposed mechanism for 2 H^+/2 e^- reduction of sub to $subH_2$ by HEH_2 mediated by Col-buffer.

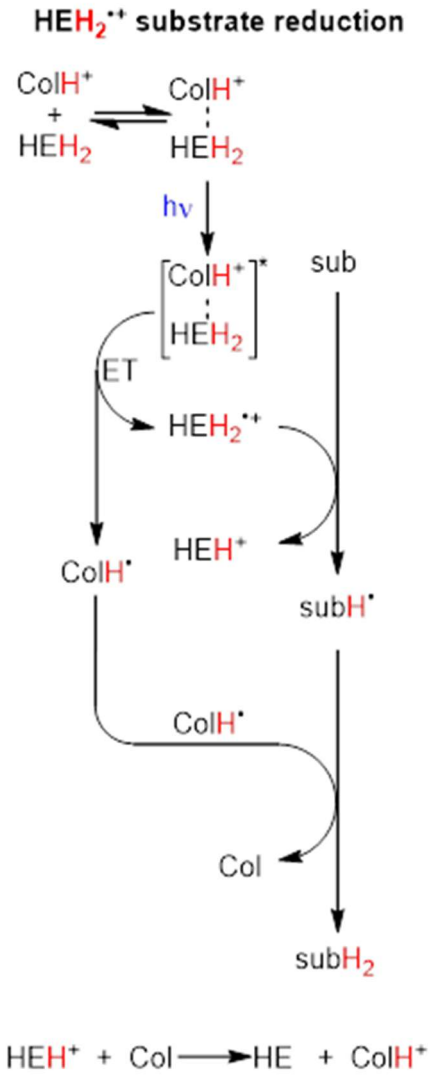

Figure D.72. Schemes depicting mechanism for 2 H^+/2 e^- reduction of sub to $subH_2$ by HEH_2 mediated by Col-buffer if direct reduction of substrate by $HEH_2^{\bullet+}$ occurs (right).

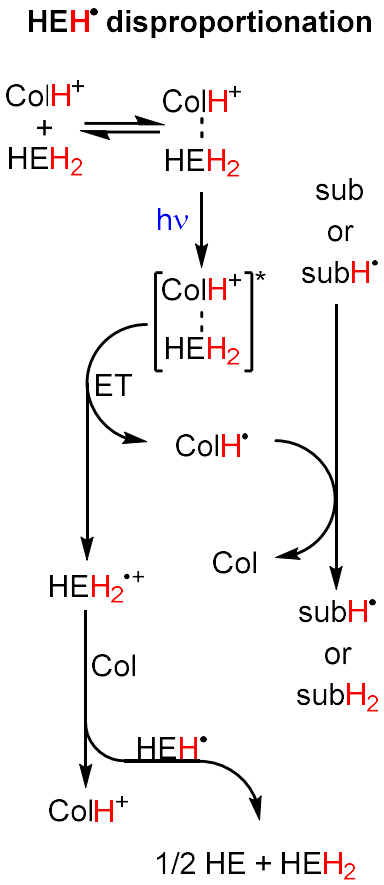

Figure D.73. Schemes depicting mechanism for 2 H^+/2 e^- reduction of sub to $subH_2$ by HEH_2 mediated by Col-buffer, if $HEH^•$ disproportionated to form 0.5 equiv HE and 0.5 equiv.

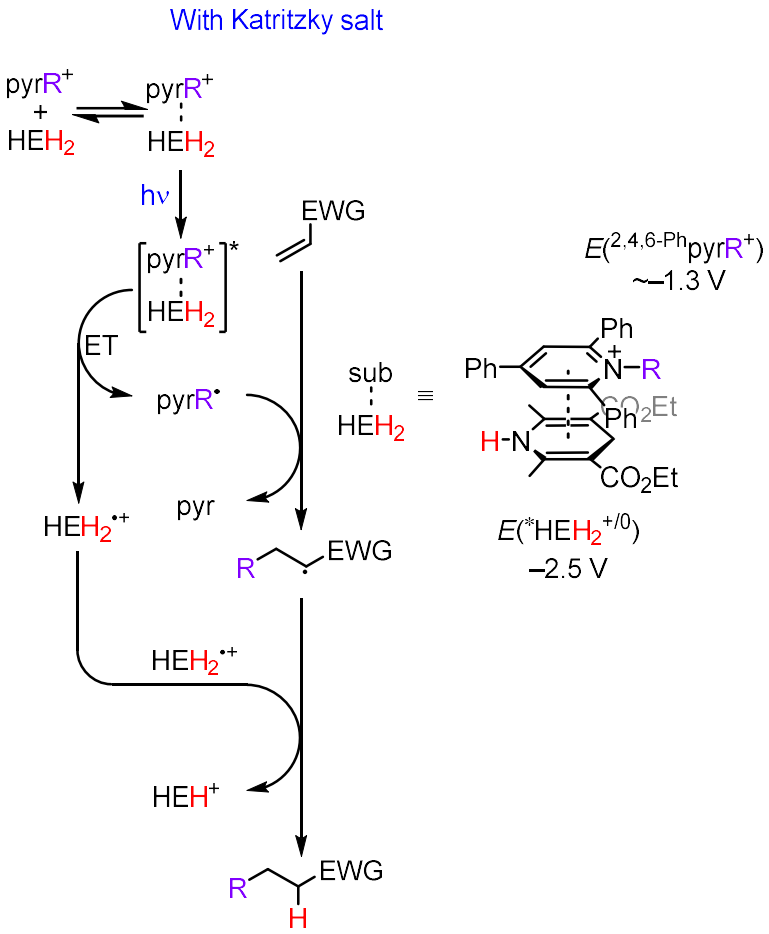

Figure D.74. Typically invoked mechanism for R• addition to sub (e.g., alkene as depicted here) by HEH_2 and Katritizky salt ($[^{2,4,6\text{-Ph}}pyrR]^+$).

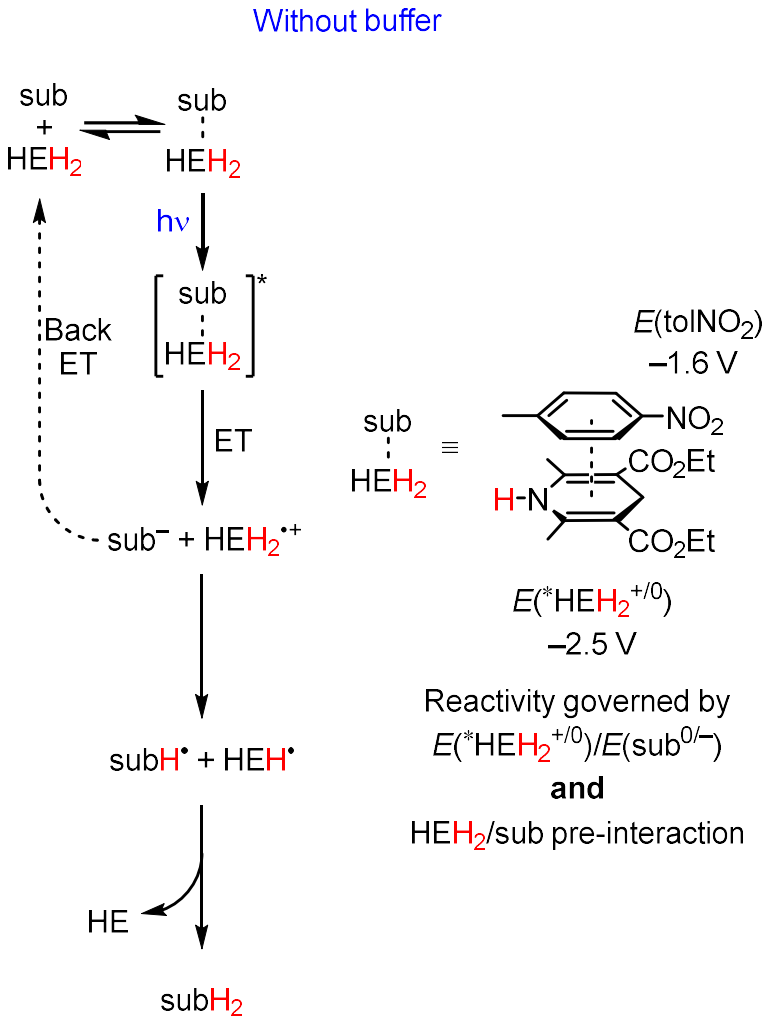

Figure D.75. Proposed mechanism for 2 H^+/2 e^- reduction of sub to $subH_2$ by HEH_2 in the absence of Col-buffer.

D.14 Computational methods

D.14.1 General overview of computational methods

As stated in the main text for our computational studies, we employed the TPSS functional[23] and a def2-TZVP basis set on transition metals and a def2-SVP basis set on all other atoms.[24] This set of functionals was chosen upon a small screen of relevant measured BDFEs. A CPCM solvent model (either MeCN or THF) was used. The ORCA 5 open-source software package was used.[25,26]

The numerical frequencies of the minimized structures were calculated to ensure that these structures represented local minima and not saddle points.

TD-DFT analysis was conducted on optimized structures using TPSSh[23,27] and a def2-TZVP basis set. This updated methodology was found to predict the $^1HEH_2$ π-π* transition more accurately and was used for all other TD-DFT calculations.

D.14.2 Treatment of H•

The treatment of $S(H^\bullet)$ and $\Delta G(H^\bullet)_{solvation}$ can be a source of systematic error in DFT calculations, therefore it is useful to detail how this value has been derived. By calculating a set of known C−H and N−H BDFEs and comparing the computed BDFE ($BDFE_{calc}$) to the measured (Table D.22), we found that the experimental values were most closely reproduced using the following formula:

$$\mathrm{BDFE}_{corrected} = \mathrm{BDFE}_{calculated} + 2.6 \ \ (\mathrm{eqn}\ D.6).$$

All calculated BDFE values cited in the main text are $BDFE_{corrected}$.

It is also worth noting that as this procedure is done on every calculated BDFE, errors in the treatment of $S(H^\bullet)$ and $\Delta G(H^\bullet)_{solvation}$ will be canceled when comparing two different BDFEs.

D.14.3 Computational evaluation of weak interactions between HEH_2 and $[ColH]^+$

When considering the relative energy of interactions between HEH_2 and [ColH]OTf the possibility for multiple conformers of HEH_2 must be accounted for. We find three major conformers can be formed, defined by the rotation of the ester bond. We define them as HEH_2 (A), the lowest energy conformer with the ester carbonyl bonds both pointing towards the 2,6-methyl groups, HEH_2 (B), intermediate energy, with one ester carbonyl group pointing towards the 2-methyl group and one carbonyl parallel with the C_4−H bonds, and HEH_2 (C) with both carbonyls parallel with the C_4−H bond (Figure D.67).

Crucially, we find that the H-bonding is only slightly disfavored to the HEH_2 (B) form, specifically with the $[ColH]^+$ coordinating to the carbonyl parallel with the C_4−H bonds. The relative energy of all three isomers and H-bonding or π-stacking interactions are summarized in Figure D.79.

D.14.4 Calculation of equilibrium isotope effects

Equilibrium isotope effects were calculated using the !PRINTTHERMOCHEM function in ORCA 5, recalculating the entropic and internal energy contributions from an optimized structure but swapping the relevant H-atoms for D-atoms.

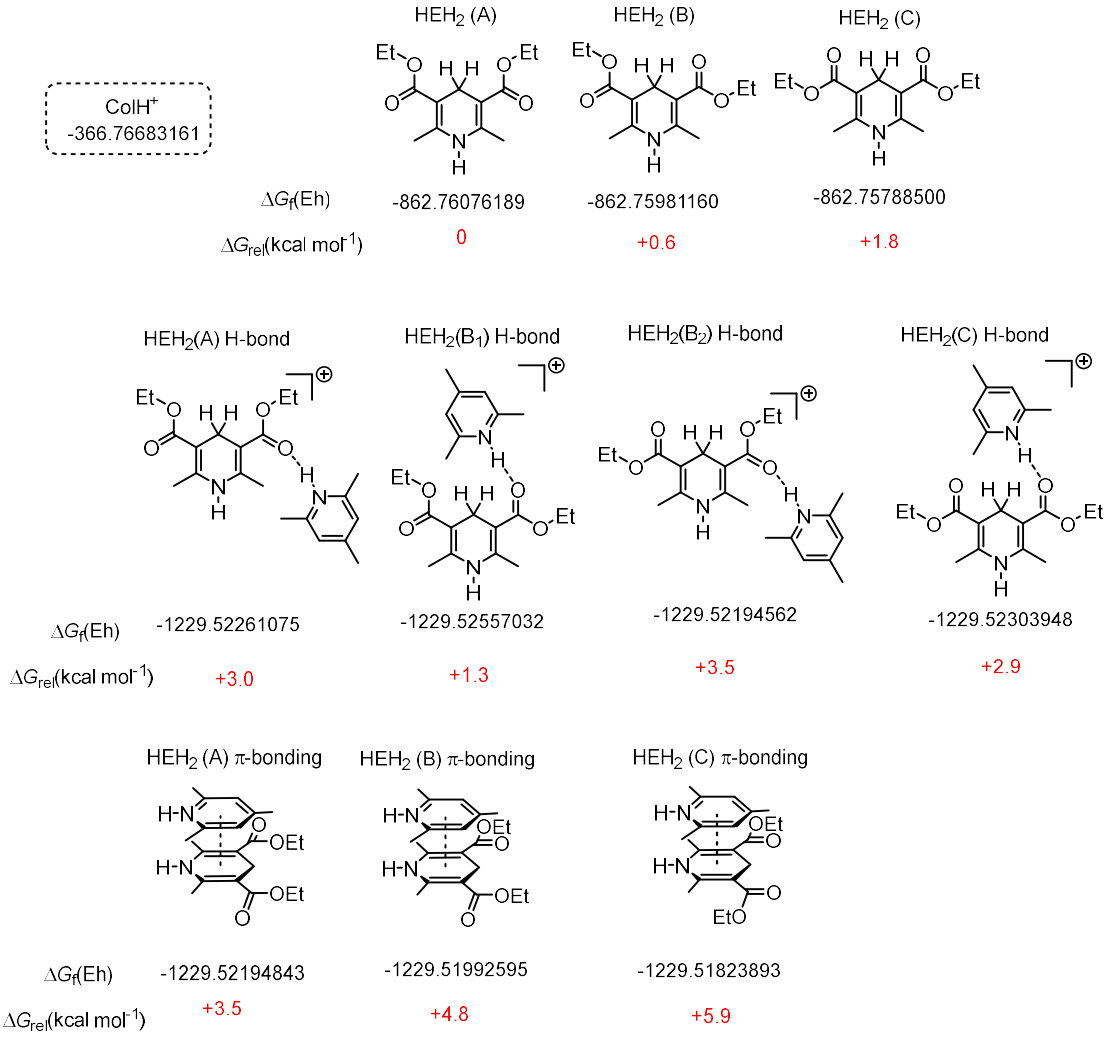

Figure D.76. Evaluation of conformers of HEH_2/$[ColH]^+$ coordination.

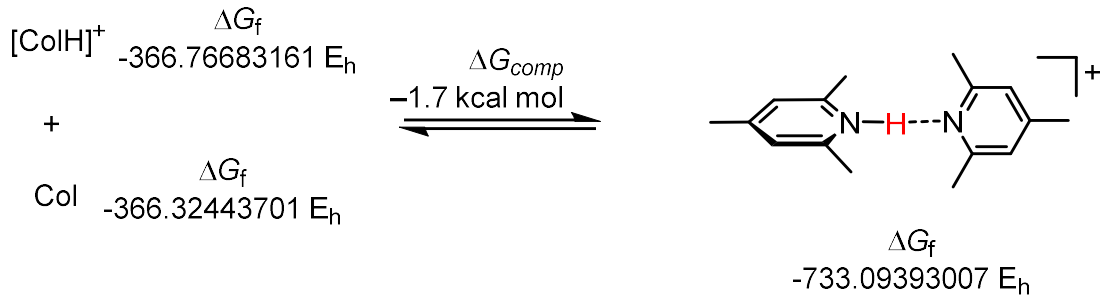

Figure D.77. Evaluation of Col-buffer homodimer, predicted to be favored in solution.

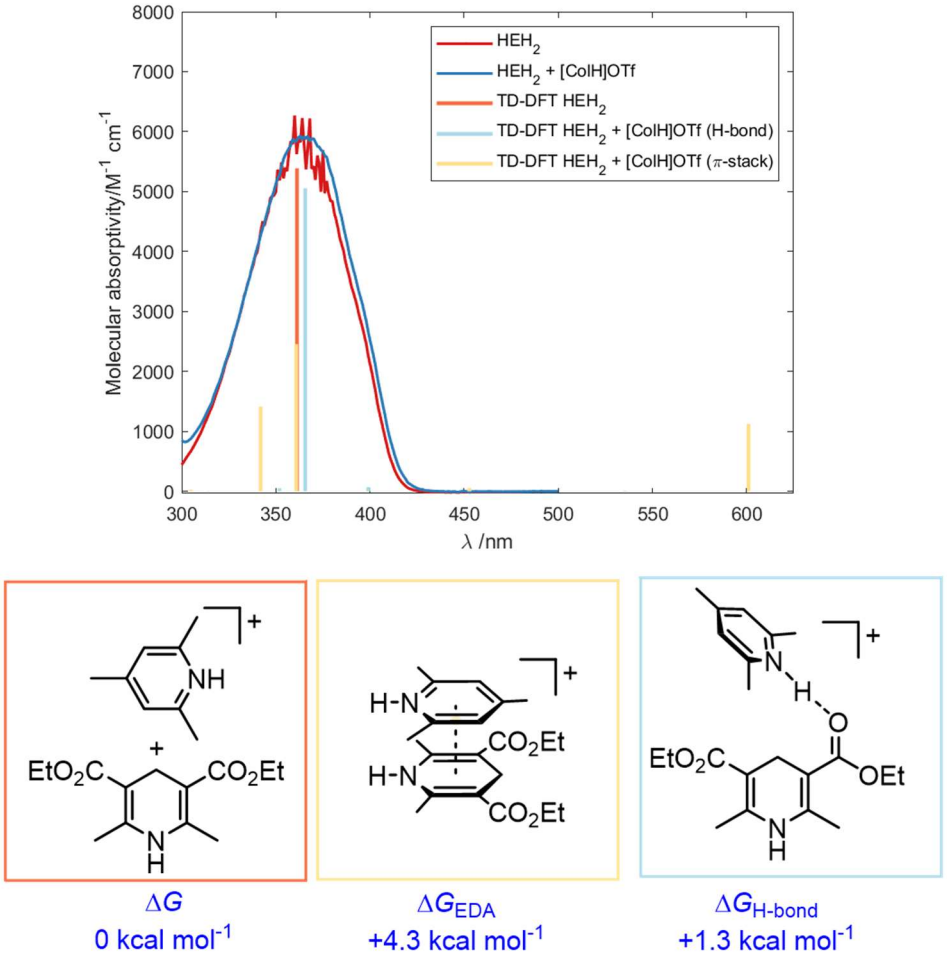

Figure D.78. Comparison of predicted absorption spectroscopy transitions of HEH_2 depending on interaction with $[ColH]^+$ (H-bond or EDA complex).

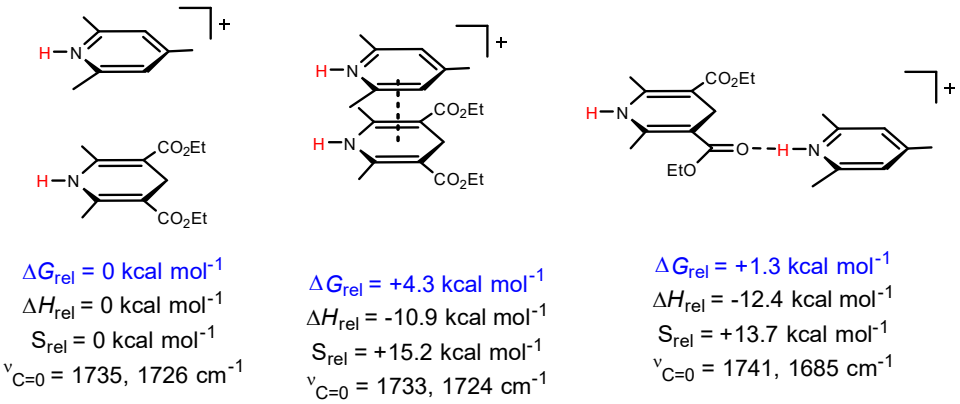

Figure D.79. Predicted vibrational modes for interactions between HEH_2 and Col-buffer.

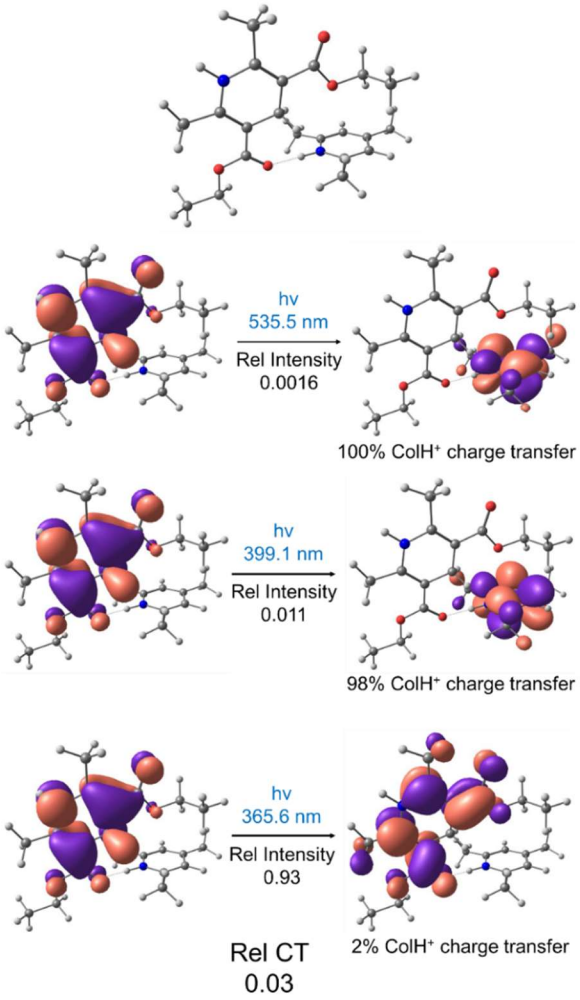

Figure D.80. Optical transitions within relevant to $[ColH]^+$ reduction with wavelength and charge transfer associated with transition to give Rel. Charge Transfer, for HEH_2, $[ColH]^+$ H-bonding interaction.

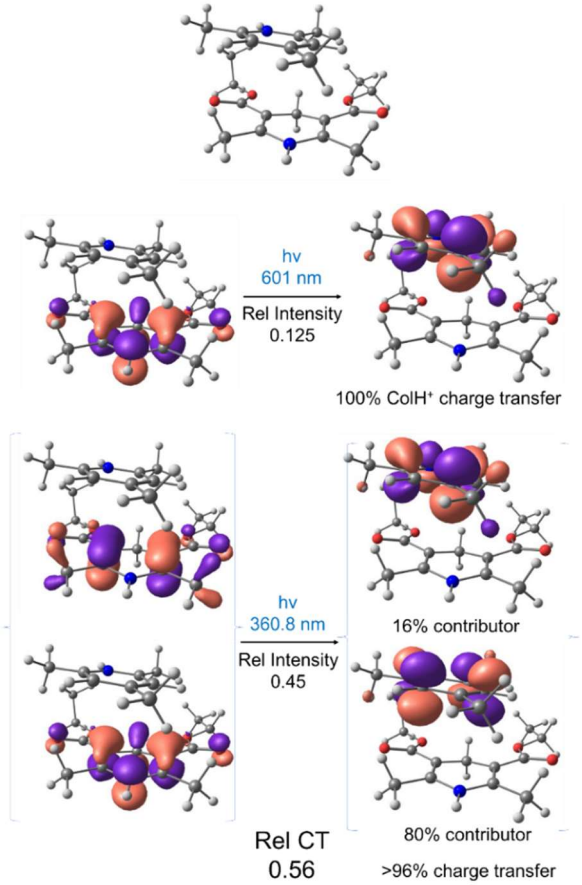

Figure D.81. Optical transitions within relevant to $[ColH]^+$ reduction with wavelength and charge transfer associated with transition to give Rel. Charge Transfer, for HEH_2, $[ColH]^+$ EDA-interaction.

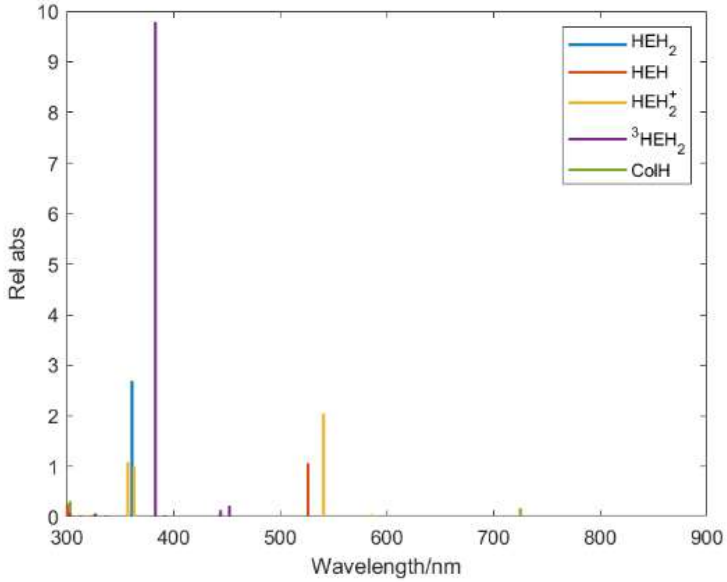

Figure D.82. Predicted TD-DFT transitions for possible species detected by Transient Absorbance spectroscopy.

We note that [ColH]$^{\bullet}$ is predicted to be far less absorbing than $[HEH_2]^{\bullet+}$. [HEH]$^{\bullet}$ is less absorbing than $[HEH_2]^{\bullet+}$, and partially overlaps with this more intense signal. Radical cations being more intense and slightly red-shifted of the corresponding, deprotonated radicals have been observed previously.[28,29,30] These predicted absorbances rationalize why these radicals cannot be picked out in the TA data.

Table D.23. ΔG_f of species relevant to H$^{\bullet}$ calibration. All species were calculated with a CPCM solvent model in MeCN.

Compound	Spin state	ΔG_f (E_h)
HEH_2	0	-861.814
EH_2	1/2	-861.185
HEH	1/2	-861.199
HE	0	-860.64
HEH^+	0	-861.08
HEH_2^+	1/2	-861.627
ColH	1/2	-366.874
Col	0	-366.325
H	1/2	-0.5102

Table D.24. Calculated BDFE for C−H and N−H bond strengths used for calibration. The error is minimized upon adding a factor of +2.6 kcal mol^{-1}; this factor is introduced to all subsequent BDFE calculations. All values measured in MeCN and a CPCM solvent model was likewise used in the calculations.

There is a large discrepancy between the DFT-calculated versus the estimated (from measured data and the Bordwell equation) $BDFE_{N–H}$ of HEH$^{\bullet}$. A contributing factor to this discrepancy might be the reversible formation of an HEH$^{\bullet}$ dimer, leading to a higher measured apparent $BDFE_{N–H}$ than expected for the idealized reaction HEH$^{\bullet}$ → HE + H$^{\bullet}$.

	ΔG_{comp} (E_h)	ΔG_{comp} (kcal mol^{-1})	ΔG_{corr} (kcal mol^{-1})	ΔG_{exp} (kcal mol^{-1})	Error, computed (kcal mol^{-1})	Error, calculated (kcal mol^{-1})
HEH_2 → HEH + H	0.104	65.3	67.9	62.3	3.0	5.6
HEH_2 → EH_2 + H	0.119	74.4	77.0	80.2	-5.8	-3.2
1/2HEH_2 → 1/2HE + H	0.077	48.2	50.8	51.4	-3.2	-0.6
HEH_2^+ → HEH^+ + H	0.037	23.2	25.8	25.63	-2.4	0.2
ColH → Col + H	0.039	24.3	26.9	29	-4.7	-2.1
					Error calc. (kcal mol^{-1}), ±4.0	Error corr. (kcal mol^{-1}), ±3.1

Table D.25. Thermochemistry of substrate semihydrogenation. (top) ΔG_f of species relevant to calculated substrate BDFEs (main text Figure 5.9). All species were calculated with a CPCM solvent model in THF. (bottom) Calculated BDFE for O−H bonds in substrates used in main text Figure 5.9.

Substrate	Spin state	ΔG_f (E_h)
H	1/2	-0.510
Me_3NO	0	-249.694
Me_3NOH	1/2	-250.289
$PhNO_2$	0	-436.950
$PhNO_2H$	1/2	-437.523
$nPrNO_2$	0	-323.774
$nPrNO_2H$	1/2	-324.340
$nPrN(H)O_2$	1/2	-324.281
NO_3^-	0	-280.626
HNO_3^-	1/2	-281.186
HNO_3	0	-281.071
$NO(OH)_2$	1/2	-281.629
$^{4\text{-Me2N}}PhCHO$	0	-479.691
$^{4\text{-Me2N}}PhCH(OH)$	1/2	-480.241
$^{4\text{-MeO}}PhCHO$	0	-460.268
$^{4\text{-MeO}}PhCH(OH)$	1/2	-460.822
$^{4\text{-MeO2C}}PhCOOMe$	0	-688.270
$^{4\text{-MeO2C}}PhC(OH)Ome$	1/2	-688.812
Benzylacetone	0	-463.639
benzylacetoneH	1/2	-464.180

	ΔG (E_h), calc.	ΔG (kcal mol^{-1}), calc.	ΔG (*k*cal mol^{-1}), corr.
$Me_3NOH \rightarrow Me_3NO + H$	0.085	53.4	56.0
$PhNO_2H \rightarrow PhNO_2 + H$	0.062	39.2	41.8
$nPrNO_2H \rightarrow nPrNO_2 + H$	0.056	35.2	37.8
$HNO_3^- \rightarrow NO_3^- + H$	0.050	31.2	33.8
$NO(OH)_2 \rightarrow HNO_3 + H$	0.048	29.9	32.5
$^{4\text{-MeO}}PhCH(OH) \rightarrow {}^{4\text{-MeO}}PhCHO + H$	0.044	27.6	30.2
$^{4\text{-Me2N}}PhCH(OH) \rightarrow {}^{4\text{-Me2N}}PhCHO + H$	0.040	24.9	27.5
$^{4\text{-MeO2C}}PhC(OH)OMe \rightarrow {}^{4\text{-MeO2C}}PhCOOMe + H$	0.031	19.7	22.3
benzylacetoneH → benzylacetone + H	0.031	19.6	22.2

Table D.26. Thermochemistry ofpossible HAT donors formed. (top) ΔG_f of species relevant to calculated ColH/HEH_2 based BDFEs. All species were calculated with a CPCM solvent model in THF. (bottom) calculated ColH/HEH_2 based BDFE for N/C−H bonds.

Substrate	Spin state	ΔG_f (E_h)
H	1/2	-0.5102
HEH_2	0	-862.761
EH_2	1/2	-862.132
HEH	1/2	-862.145
HE	0	-861.587
HEH^+	0	-862.017
HEH_2^+	1/2	-862.565
ColH	1/2	-366.873
Col	0	-366.324
$ColH^+$	0	-366.767
$^3HEH_2$	1	-862.69

	ΔG (E_h), calc.	ΔG (kcal mol^{-1}), calc.	ΔG (*k*cal mol^{-1}), corr.
$HEH_2 \rightarrow HEH + H$	0.106	66.5	69.1
$HEH_2 \rightarrow EH_2 + H$	0.119	74.7	77.3
$HEH \rightarrow HE + H$	0.047	29.4	32.0
$EH_2 \rightarrow HE + H$	0.034	21.3	23.9
$HEH_2^+ \rightarrow HEH^+ + H$	0.038	23.6	26.2
$^3HEH_2 \rightarrow HEH + H$	0.035	22.2	24.8
$ColH \rightarrow Col + H$	0.038	24.1	26.7

Table D.27. Calculated entropy and internal energy for minimized structures of HEH_2, $ColH^+$ and Col with varying isotopologues.

	Entropy and internal energy (298 K), E_h	$\Delta\Delta G_{H\text{-}D}$ (kcal mol^{-1})
$ColH^+$	0.1473	-
$ColD^+$	0.1437	-
$\Delta G(ColH^+) - \Delta G(ColD^+)$	-	2.3
HEH_2	0.2566	
d_1-HEH_2	0.2531	
d_2-HEH_2	0.2499	
$\Delta G(HEH_2) - \Delta G(d_1\text{-}HEH_2)$	-	2.2
$\Delta G(HEH_2) - \Delta G(d2\text{-}HEH_2)$	-	4.2
$HEH_2\cdots HCol^+$ (H-bond)	0.4278	-
d_1-$HEH_2\cdots DCol^+$ (H-bond)	0.4208	-
d_2-$HEH_2\cdots HCol^+$ (H-bond)	0.4211	-
$\Delta G(HEH_2\cdots HCol^+$ (H-bond)) − $\Delta G(d_1\text{-}HEH_2\cdots DCol^+$ (H-bond))	-	4.4
$\Delta G(HEH_2\cdots HCol^+$ (H-bond)) − $\Delta G(d_2\text{-}HEH_2\cdots HCol^+$ (H-bond))	-	4.2
$HEH_2\cdots HCol^+$ (π-stack)	0.4290	-
d_1-$HEH_2\cdots DCol^+$ (π-stack)	0.4219	-
d_2-$HEH_2\cdots HCol^+$ (π-stack)	0.4223	-
$\Delta G(HEH_2\cdots HCol^+$ (π-stack)) − $\Delta G(d_1\text{-}HEH_2\cdots DCol^+$ (π-stack))	-	4.5
$\Delta G(HEH_2\cdots HCol^+$ (π-stack)) − $\Delta G(d_2\text{-}HEH_2\cdots HCol^+$ (π-stack))	-	4.2
$ColH\cdots Col^+$	0.3011	-
$ColD\cdots Col^+$	0.2979	-
$\Delta G(ColH^+\cdots Col)$ − ΔG(ColD+…Col)	-	2.0

Table D.28. Calculated equilibrium isotope effects (based on table D.27) for pre-complexation.

Reaction	Difference in entropy and internal energy (298 K), E_h	$\Delta\Delta G_{H\text{-}D}$ (kcal mol^{-1})	KIE
ColH$^+$ + HEH_2 -> HEH_2···HCol$^+$ (H-bond)	0.0239	15.0	-
ColD$^+$ + d_1-HEH_2 -> d_1-HEH_2···DCol$^+$ (H-bond)	0.0240	15.1	-
ColH$^+$ + $d2$-HEH_2 -> d_2-HEH_2···HCol$^+$ (H-bond)	0.0238	15.0	-
$\Delta\Delta G$(H-D for N-D)	-0.0001	-0.1	1.16
$\Delta\Delta G$(H-D for C-D)	0	0	0.96
ColH$^+$ + HEH_2 -> HEH_2···HCol$^+$ (π-stack)	0.0251	15.8	
ColD$^+$ + d_1-HEH_2 -> d_1-HEH_2···DCol$^+$ (π-stack)	0.0251	15.8	
ColH$^+$ + $d2$-HEH_2 -> d_2-HEH_2···HCol$^+$ (π-stack)	0.0251	15.7	
$\Delta G(HEH_2) - \Delta G(d_1\text{-}HEH_2)$	0	0	1.00
$\Delta G(HEH_2) - \Delta G(d2\text{-}HEH_2)$	0	0	0.96
ColH$^+$···Col + HEH_2 -> HEH_2···HCol$^+$ + Col (H-bond)	-0.1299	-81.5	
ColD$^+$···Col + d_1-HEH_2 -> d_1-HEH_2···DCol$^+$ + Col (H-bond)	-0.1302	-81.7	
ColH$^+$···Col + $d2$-HEH_2 -> d_2-HEH_2···HCol$^+$ + Col (H-bond)	-0.1300	-81.6	
ΔG(HEH_2···HCol$^+$ (H-bond)) − ΔG(d_1-HEH_2···DCol$^+$ (H-bond))	0.0003	0.1	0.80
ΔG(HEH_2···HCol$^+$ (H-bond)) − ΔG(d_2-HEH_2···HCol$^+$ (H-bond))	0.0001	0.0	0.96
ColH$^+$···Col + HEH_2 -> HEH_2···HCol$^+$ + Col (π-stack)	-0.0846	-53.1	
ColD$^+$···Col + d_1-HEH_2 -> d_1-HEH_2···DCol$^+$ + Col (π-stack)	-0.0846	-53.1	
ColH$^+$···Col + $d2$-HEH_2 -> d_2-HEH_2···HCol$^+$ + Col (π-stack)	-0.0846	-53.1	
ΔG(HEH_2···HCol$^+$ (H-bond)) − ΔG(d_1-HEH_2···DCol$^+$ (π-stack))	-	0.0	0.97
ΔG(HEH_2···HCol$^+$ (H-bond)) − ΔG(d_2-HEH_2···HCol$^+$ (π-stack))	-	0.0	0.96

D.15 References for Appendix D

1. Norcross, B. E.; Clement, G.; Weinstein, M. *J. Chem. Educ.* **1969**. 46, 694.
2. Arashiba, K.; Eizawa, A.; Tanaka, H.; Nakajima, K.; Yoshizawa, K.; Nishibayashi, Y. *Bull. Chem. Soc. Jpn.* **2017**. 90, 1111-1118.
3. Ashida, Y.; Arashiba, K.; Nakajima, K.; Nishibayashi, Y. *Nature* **2019**. 568, 536–540.
4. Johansen, C. M.; Boyd, E. A.; Peters, J. C. *Sci. Adv.* **2022**. 8, eade3510.
5. Golubev, N. S.; Smirnov, S. N.; Schah-Mohammedi, P.; Shenderovich, I. G.; Denisov, G. S.; Gindin, V. A.; Limbach, H. H. *Russ. J. Gen. Chem.* **1997**. 67, 1082–1087.
6. Ren, C.; Ji, G.; Li, X.; Zhang, J. *Chem. – Eur. J.* **2022**. 28, e202201442.
7. Zhang, D.; Wu, L.-Z.; Zhou, L.; Han, X.; Yang, Q.-Z.; Zhang, L.-P.; Tung, C.-H. *J. Am. Chem. Soc.* **2004**. 126, 3440–3441.
8. Li, H.; Liu, Y.; Chiba, S. *Chem. Commun.* **2021**. 57, 6264–6267.
9. Tricoli, V.; Orsini, G.; Anselmi, M. *Phys. Chem. Chem. Phys.* **2012**. 14, 10979–10986.
10. Fulmer, G. R.; Miller A. J. M.;, Sherden, N. H.; Gottlieb, H. E.; Nudelman, A.; Stoltz, B. M.; Bercaw, J. E.; Goldberg, K. I. *Organometallics* **2010**. 29, 2176–2179.
11. Weatherburn, M. W. *Anal. Chem.* **1967**. 39, 971–974.
12. Tshepelevitsh, S.; A. Kütt, M. Lõkov, I. Kaljurand, J. Saame, A. Heering, P. G. Plieger, R. Vianello, I. Leito, *Eur. J. Org. Chem.* **2019**. 2019, 6735–6748.
13. Hatchard, C. G.; Parker, C. A.; Bowen, E. J. *Proc. R. Soc. Lond. Ser. Math. Phys. Sci.* **1997**. 235, 518–536.
14. Lakowicz, J. R., *Principles of Fluorescence Spectroscopy*. **2006** Springer.
15. Espinoza, E. M.; Clark, J. A.; Soliman, J.; Derr, J. B.; Morales, M.; Vullev, V. I. *J. Electrochem. Soc.* **2019**. 166, H3175.

16. Agarwal, R. G.; Coste, S. C.; Groff, B. D.; Heuer, A. M.; Noh, H.; Parada, G. A.; Wise, C. F.; Nichols, E. M.; Warren, J. J.; Mayer, J. M. *Chem. Rev.* **2022**. 122, 1–49.
17. Shen, G.-B.; Fu, Y.-H.; Zhu, X.-Q. *J. Org. Chem.* **2020**. 85, 12535–12543.
18. Bordwell, F. G.; Cheng, J. P.; Harrelson, J. A. *J. Am. Chem. Soc.* **1988**. 110, 1229–1231.
19. Garrido, G.; Rosés, M.; Ràfols, C.; Bosch, E. *J. Solut. Chem.* **2008**. 37, 689–700.
20. Munisamy, T.; Schrock, R. R. *Dalton Trans.* **2011**. 41, 130–137.
21. Pragst, F.; Šantrůček, M. *J. Für Prakt. Chem.* **1987**. 329, 67–80.
22. Rehm, D.; Weller, A. *Isr. J. Chem.* **1970**. 8, 259–271.
23. Tao, J.; Perdew, J. P.; Staroverov, V. N.; Scuseria, G. E. *Phys. Rev. Lett.* **2003**. 91, 146401–146404.
24. Weigend, F. *Phys. Chem. Chem. Phys.* **2006**. 8, 1057–1065.
25. Neese, F.; Wennmohs, F.; Becker, U.; Riplinger, C. *J. Chem. Phys.* **2020**. 152, 224108.
26. Neese, F. *WIREs Comput. Mol. Sci.* **2022**. 12, e1606.
27. Staroverov, V. N.; Scuseria, G. E.; Tao, J.; Perdew, J. P. *J. Chem. Phys.* **2003**. 119, 12129–12137.
28. Czochralska, B.; Lindqvist, L. *Chem. Phys. Lett.* **1983**. 101, 297–299.
29. Anne, A.; Hapiot, P.; Moiroux, J.; Neta, P.; Saveant, J. M. *J. Am. Chem. Soc.* **1992**. 114, 4694–4701.
30. Zielonka, J.; Marcinek, A.; Adamus, J.; Gębicki, J *J. Phys. Chem. A* **2003**. 107, 9860–9864.